Two-Dimensional Quench Propagation Model for a Three-Dimensional "High -Temperature" Superconducting Coil

by

Benjamin J. Haid

S.B. Mechanical Engineering
Massachusetts Institute of Technology, 1996

Submitted to the Department of Mechanical Engineering
in partial fulfillment of the requirements for the degree of

Master of Science in Mechanical Engineering

at the

MASSACHUSETTS INSTITUTE OF TECHNOLOGY

June 1998

Author ....
Department of Mechanical Engineering
May 8, 1998

Certified by ....
Yukikazu Iwasa
Thesis Supervisor

Accepted by ....
Ain A. Sonin
Chairman, Departmental Graduate Committee

Two-Dimensional Quench Propagation Model for a Three-Dimensional "High -Temperature" Superconducting Coil

by

Benjamin J. Haid

Submitted to the Department of Mechanical Engineering
on May 8, 1998, in partial fulfillment of the
requirements for the degree of
Master of Science in Mechanical Engineering

Abstract

Quenching is a thermal failure mechanism encountered with superconducting magnets. When a section of conductor is driven normal by an external heat input, the magnet transport current flows through a resistance, causing joule dissipation. If heat is not conducted away from the normal region faster than it is dissipated, the normal region will grow and the temperature will increase indefinitely. Growth of the normal region is commonly refered to as normal zone propagation(NZP). A reliable NZP model is necessarry for designing protection systems because a quench may cause irreparable damage if a section of the winding is over-heated.

This thesis develops a numerical NZP model for a three dimensional, dry-wound, BSSCO-2223 superconducting magnet. The test magnet operates under quasi-adiabatic conditions at 20 K and above, in zero background field. It is contained in a stainless steel cryostat and cooled by a Daikin cryocooler. The NZP model is based on the two-dimensional transient heat diffusion equation. Quenches are simulated by a numerical code using the finite-difference method. Agreement between voltage traces obtained in the test magnet during heater-induced quenching events and those computed by the numerical NZP model is reasonable. The model indicates that thermal contact resistance has a dominant effect on propagation in the azimuthal direction(across layers).

The model is also used to simulate quenching in persistent-mode magnets similar in construction with the test magnet. Specifically studied were effects of magnet inductance, for a given set of operating current and temperature, on the maximum temperature reached in one full turn of the conductor located at the magnet outermost layer driven normal with a heater. The simulation demonstrates that there is an operating current limit for a given magnet inductance and operating temperature below which the magnet can be considered self-protecting. The simulation also demonstrates that shunted subdivision lowers the maximum temperature.

Thesis Supervisor: Dr. Yukikazu Iwasa
Title: Research Professor, Francis Bitter Magnet Laboratory, and Senior Lecturer, Department of Mechanical Engineering, MIT

Acknowledgments

I owe many thanks to my thesis advisor, Dr. Yukikazu Iwasa, for the many ideas he has contributed to this and other work, the time spent explaining concepts and reviewing this thesis, and the financial support appointed to me that has permitted me to live comfortably during the last couple of years. I am also indebted to the lab technicians Melvin Vestal, David Johnson, and Ron LeRoche for their help in locating materials and assistance in assembling apparatus and other needed parts. I thank my fellow members of our research group, past and present, for their flexibility and generous help. In particular, I give special thanks to Dr. Hai Gun Lee, Kevin McFall, and Dr. Makoto Tsuda. I thank Julian Orbanes for his extensive advice on the simulation code.

Several individuals have provided me with moral support over the years. I thank Dan Shnidman for the many retreats and reality checks. And of course, I thank my parents for their nurturing and guidance. Had they not been there, I would definitely not have had the ambition to complete this or any other comparable work.

Contents

List of Figures

List of Tables

Chapter 1

Introduction

1.1 Superconductivity

1.1.1 Discovery of Superconductivity

The electrical resistivity of some materials becomes zero at low temperatures, defining a state known as superconductivity. In 1911, a Dutch physicist, Kamerlingh Onnes, discovered this condition when he cooled mercury to 4.2 K (the boiling point of liquid helium at atmospheric pressure) and detected no measurable resistance. He later discovered that several other metals, such as lead and tin, also exhibited the same change of state. However, these early superconductors did not promise any practical advantage because they could not carry significant current densities while maintaining their superconducting state. Superconducting materials with maximum current densities(or critical current densities) high enough to permit design improvements over the use of normal conductive metals, such as copper, were not discovered for several decades.

1.1.2 Type II Superconductors

In the early 1950s, Nb_3Sn and NbTi were found to exhibit superior current-carrying performance even at high magnetic-fields. Their critical current densities are greater than those of copper conductors in well-designed water-cooled copper magnets. These superconductors

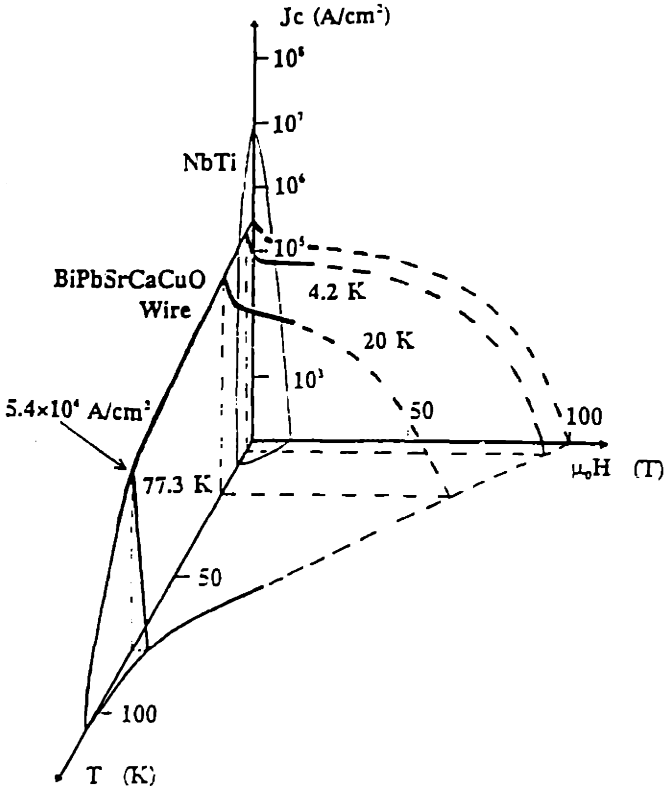

Figure 1-1: Critical surfaces for NbTi and BSCCO-2223 [1]

are classified as Type II. The Type I classification applies to the monatomic metals with relatively low critical currents that Onnes discovered. Type I and Type II superconductors also differ in their response to external magnetic field. Below a critical field, H_{c1}, a body of either type will completely exclude the field from its interior while it is superconducting, a behavior known as the Meissner effect. The magnitude of H_{c1} varies with material and temperature. Above H_{c1}, Type I superconductors become nonsuperconducting; Type II materials allow field penetration throughout the body while remaining superconducting until the field reaches H_{c2}, which is several orders of magnitude greater than H_{c1}.

The critical current density of Type II superconductors varies with temperature and magnetic field. There is a maximum temperature, T_c, as there is a maximum field strength, H_{c2}, and within these limits the materials are in the superconducting state. Figure 1-1 shows three-dimensional plots defining the critical surfaces for NbTi and a high-temperature superconductor(HTS) compound of bismuth(Bi), lead(Pb), strontium(Sr), calcium(Ca), copper(Cu), and oxygen(O) – BiPbSrCaCuO – often known by BSCCO-2223[1].

1.2 High Field Superconducting Magnets

High field magnets wound with Type II superconductor pose several advantages over copper magnets. To begin with, they require less power to operate. Most of the required power is used for refrigeration to maintain the magnet at its operating temperature. There is little heat dissipation as a result of the operating current because the conductor has negligible resistance. On the other hand, the electrical resistance of copper magnets requires higher power for driving current through them. For example, a 15-T, 5-cm bore DC superconducting magnet system requires a few hundred watts, while an equivalent copper magnet requires several megawatts[2]. The second advantage of high-field superconducting magnets is they can produce the same field as copper magnets while using a smaller volume of conductor.

1.3 High-Temperature Superconductors

In 1986, Karl Alex Muller and Johann Georg Bendnorz of the Zurich IBM Research Laboratory reported an alloy of Ba-La-Cu-O as having a critical temperature of 35 K, over 10 K above the highest critical temperature known at that time. The discovery started a worldwide effort pursuing superconductors with even higher critical temperatures. Within a few years, materials with critical temperatures in excess of 100 K were produced. Many of these "high-Tc" materials have critical current densities at liquid nitrogen temperatures that compare to the current densities of copper conductors in water-cooled magnets. The ability to produce high fields at liquid nitrogen temperatures is a key advantage over materials which must be cooled by liquid helium(low-temperature superconductors or LTS), as cryogenics is more efficient at higher operating temperatures. Therefore, HTS magnets offer better cryogenic efficiencies over LTS magnets.

The disadvantages to high-temperature superconductors lies in their manufacturing complexity and mechanical properties. Most are ceramic and very brittle. Their maximum strain is smaller and more care must be taken in designing high field magnets, where the conductor is inevitably stressed under high Lorentz forces. Strain cycling will also cause the critical current to suffer. In terms of manufacturing, many high-Tc materials contain more than four constituents, making it difficult to reduce defects and maintain a consistent quality. The critical current often varies along the conductor. Finally, manufacturing difficulties makes them far more expensive than low-Tc materials.

1.4 Thermal Stability of Superconductors

A superconducting magnet must operate at a low enough temperature so that the critical current(which is also determined by the operating field) is larger than the operating current. Operating below the critical current does not guarantee stable operation in the superconducting state. There is inevitably random points of localized heat dissipation throughout a superconductor when it is carrying current. These may heat small regions into the normal state. Heat dissipated by the normal region will spread and drive adjacent conductor normal. In essence, the normal region grows. We call this event normal zone propagation(NZP), or quench propagation. It is the main thermal behavior of a superconducting magnet driven normal. We can protect against random disturbances by embedding the superconductor in a conductive metallic matrix, referred to as sheathing. This allows current to flow around a small normal region with only a small increase in voltage. Also, the high thermal conductivity of the metal will conduct heat away from a normal region and bring it back into the superconducting state. However, sheathing the superconductor cannot prevent magnets from quenching for all sources of heat dissipation. For example, mechanical disturbances, such as epoxy cracking under changing stress, can cause a large enough thermal power input to propagate a quench in a sheathed conductor. We require a theoretical basis for designing superconducting magnets that will ensure stable operation. Stekly first proposed a concept in the mid-1960s, known as cryostability, where normal-state(all current flows through the matrix) Joule heating is balanced with convective cooling by a liquid cryogen, making NZP impossible. However, the cryostability criterion is the extreme of conservative design. All superconducting magnets may be operated stably with higher current densities.

In this thesis we study the stability of an HTS magnet operated dry, meaning there is no cryogen in contact with the conductor and the magnet operation is essentially adiabatic. If we were to use cryostability as the basis for design, the magnet would carry no current because the cooling term is zero. In practice, adiabatic magnets operate at higher overall current densities than cryostable magnets due to the absence of cooling channels within the wind. The trade-off to improved current density is susceptibility to damage during a quench event. Therefore, we require an NZP model which will allow us to predict the transient thermal response to particular heat inputs. Specifically, an NZP model should help answer the following questions:

1. Will the magnet quench by a specific heat dissipation, considering its magnitude and location(s)?
2. What type of protection system is required to ensure that the magnet will never be damaged?
3. What voltage magnitude across a specific length of conductor indicates a nonrecovering quench that will propagate and potentially damage the magnet?

Reliable NZP models have been developed for low-temperature superconducting magnets using analytical methods. Numerical methods have also been developed, showing some improvement in accuracy over the analytical methods. However, as is described in Chapter 2, the accuracy of analytical models suffers substantially when applied to high-temperature superconducting magnets. For coils wound with BSCCO-2223, the most common high-Tc superconductor currently wound into coils, the modeling of NZP is not yet complete. Almost all past work has been limited to one-dimensional propagation, along the length of the conductor. Lim[3] has modeled NZP in a single pancake two-dimensionally by using a numerical technique. But many, if not most magnets consist of multiple turns per layer. It is the intent of this project to model NZP in a three-dimensional coil using numerical techniques.

1.5 Overview

The purpose of this thesis is to develop a quench propagation model that may be used for designing the protection of a dry HTS magnet operating above 20 K. The model is based upon the two-dimensional form of the heat equation and is implemented by a numerical code using the finite difference method. The code predicts voltage rise and temperature profiles in the outer layers over time. The results of the model are compared with voltage traces recorded during quench events in a 360-turn BSCCO-2223 test magnet. Much work remains before high-temperature superconducting magnets will become practical components of larger systems. It is hoped that the model demonstrated in this work will contribute to the effort by providing insight into the means of protecting these magnets against damaging quenches.

Chapter 2

Experimental Techniques–Apparatus and Procedure

Results of a normal zone propagation code developed in this thesis for a layer-wound BSCCO-2223 test coil were compared with experimental results obtained with a 360-turn BSCCO-2223 coil constructed by Sumitomo Electric. The voltages across individual turns were recorded during quench events, each event induced with a heat pulse applied to a section of the winding.

2.1 Overall Operation

The experimental apparatus used to quench the test magnet is shown in Figure 2-1. The test magnet is maintained at 20 K or above with a Daikin cryocooler. The test magnet is contained within a stainless steel cryostat that is linked to the cryocooler with a stainless steel flange. Both cryostat vacuum chambers, the sample space and the vacuum space, are evacuated with a diffusion pump to less than 10^{-5} torr, minimizing convective heat transfer. Thirty layers of superinsulation are wrapped around the system to reduce radiation heat transfer. Liquid nitrogen is used to cool the nitrogen space wall thereby reducing radiation into the sample space wall and the test magnet. A copper extension rod couples the second stage of the cryocooler to the coil form, maintaining their temperature within a

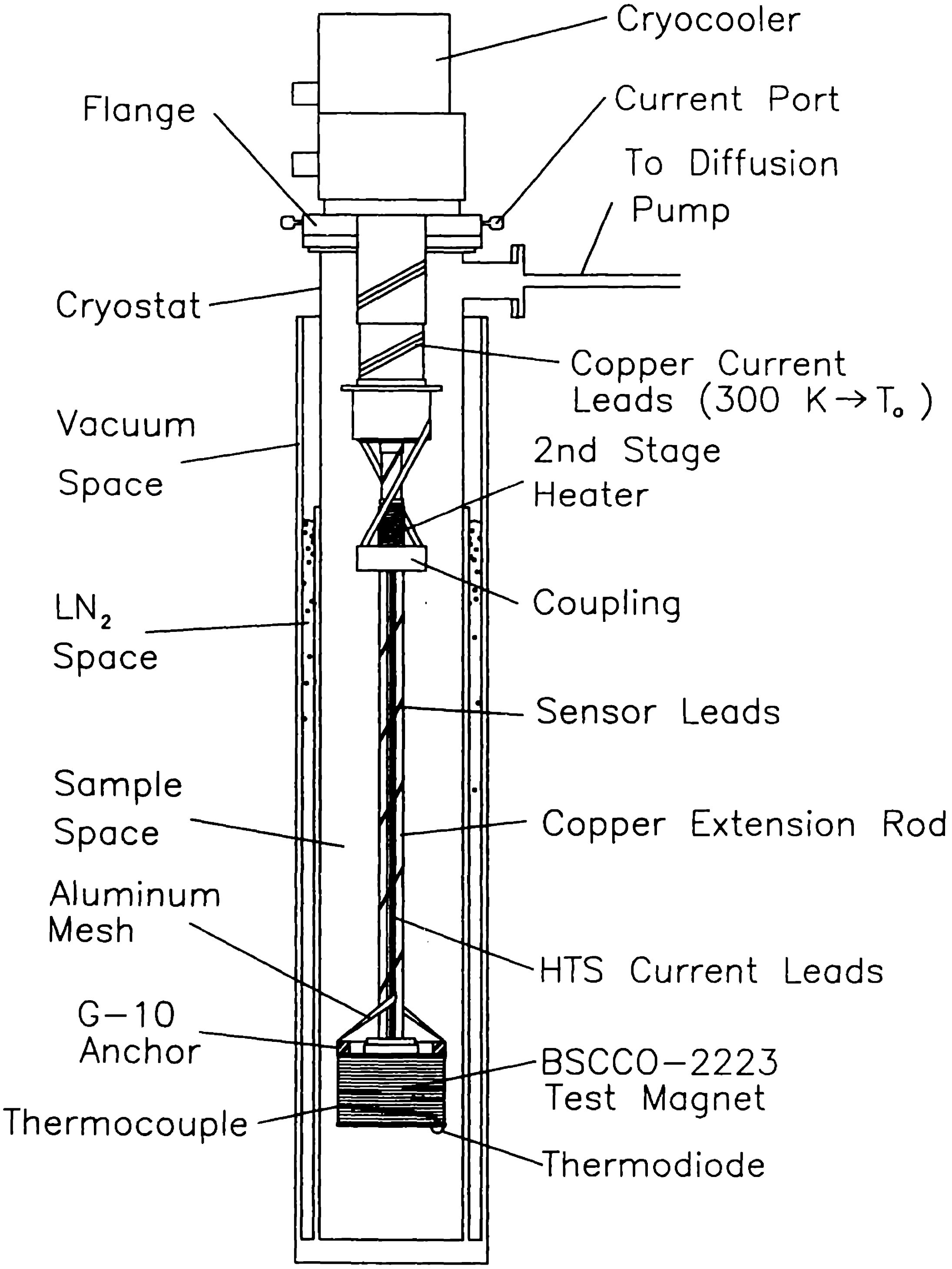

Figure 2-1: Experimental Apparatus

1 K difference. Temperature of the sample is adjusted with a heater enfolding the second stage of the cryocooler. The temperature is measured with a calibrated GaAlAs thermodiode that is located at the bottom of the copper coil form. Difference in temperature between the conductor and the coil form is measured with a type E thermocouple.

Current is supplied to the test magnet by two Hewlett Packard power supplies operating in parallel. The supply leads are clamped to the current lead outlets, which extend from the flange that joins the cryocooler with the cryostat. Copper cable connects the current lead outlets to HTS leads at the top of the copper extension rod. The HTS leads, consisting of BSCCO-2223 tape, travel the length of the copper extension rod to join the aluminum mesh leads of the sample magnet.

Each quench is initiated with a stainless steel heater that is in contact over approximately one full turn of the outermost layer. The propagation is revealed through voltage measurements across taps placed around regions of the coil expected to show significant voltage rise. Leads from the taps travel to a 32-pin connector extending from the top flange. A digital computer with Labview software samples the tap voltages, transport current, and the thermodiode voltage. Keithley voltmeters are used to monitor the voltages in real time.

2.2 Thermal Systems

2.2.1 Cryostat/Cryocooler Assembly

The cryostat consists of two sealed spaces, the vacuum space and the sample space. The vacuum space encompasses a nitrogen space as shown in Figure 2-1. When the vacuum space is evacuated, convective heat transfer into the nitrogen space and the sample space is minimized. A vacuum valve allows the diffusion pump to be disconnected from the vacuum space while a vacuum is still maintained. A vacuum flange at the top of the sample space permits continuous pumping. Pressure is measured with a discharge gauge located just upstream of the diffusion pump.

The vacuum space walls are constructed with stainless steel sheets. The nitrogen space is open to the atmosphere. Its stainless steel inner wall faces the aluminized copper wall of the sample space. When the nitrogen space is filled with liquid nitrogen, radiation to the sample space wall is reduced. In turn, the wall of the sample space cools and radiation heat transfer into the system decreases. We observed that if nitrogen is not used to cool the wall, the temperature difference between the thermodiode and the bottom outside turns of the test magnet may be greater than 30 K. The temperature gradient is caused by radiation transfer and separation from a good thermal sink by approximately 500 cm of conductor.

A flange at the top of the sample space is constructed from 3/16 inch stainless steel. The cryocooler and the cryostat flange are joined by bolts to an intermediate 1/2 inch thick stainless steel flange. Silicon greased Parker O-rings sit in canals on top of each flange for a vacuum tight seal. The cryocooler is a Daikin model U104CWZ.

2.2.2 Copper Extension Rod

The copper extension rod serves to thermally connect the test magnet to the cryocooler second stage while keeping the cryocooler away from the magnetic fields produced by the test magnet. The cryocooler contains a permanent magnet stepper motor that drives a piston for conducting the helium flow. Too high a magnetic field will cause the motor to saturate.

The rod is 50-cm long, and has a square cross-section with 28-mm sides. Apiezon-N grease is applied at both end surfaces to improve the thermal connection. Two pairs of BSCCO-2223 tape strips are adhered to opposite sides of the rod to act as current leads. Sensor leads are wrapped multiple times around it to reduce conductive heat input into the sample and prevent significant temperature variation at tap connections.

2.3 Electrical Systems

Figure 2-2 is a schematic of the electrical systems.

2.3.1 Current Source and Copper Leads

Current is supplied by two Hewlett Packard 6260B 100 A, 10 V power supplies operating in parallel. A 200 $\mu\Omega$ shunt placed in series with the output allows the current to be measured

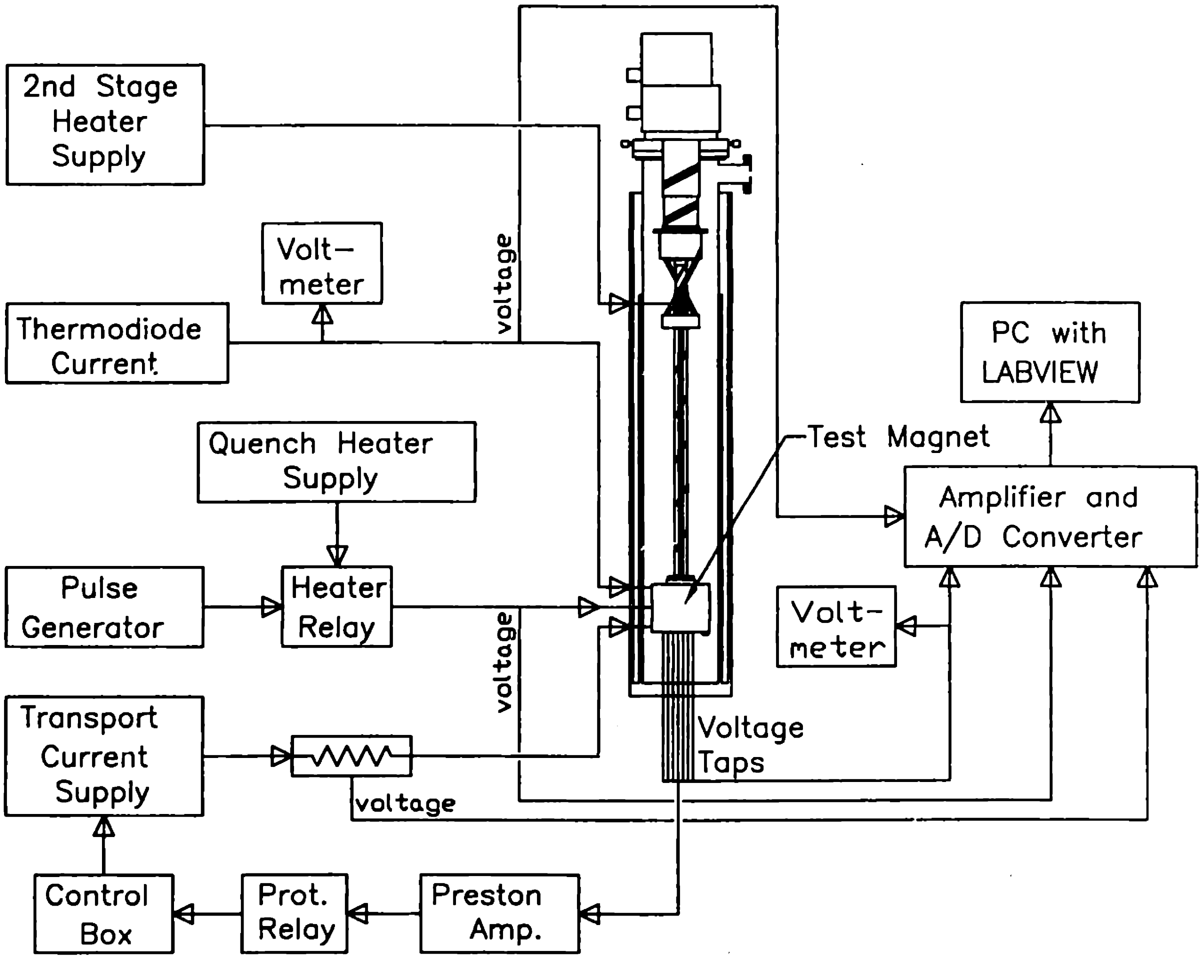

Figure 2-2: Schematic of the electrical systems.

from the voltage across the shunt. Current is controlled by a resistance across a pair of supply inputs. Shorting the inputs forces the current to zero. To protect the test magnet from thermal damage, a latching relay shorts the supply inputs when the voltage across the heated turn reaches a preset value. The relay is controlled by a variable amplifier. Prior to each trial a shut-off voltage value, V_{off}, corresponding to one turn at room temperature is calculated. The variable amplifier is adjusted to trip the protection relay when the heated turn reaches V_{off}, calculated with the following equation:

$$V_{off} = \frac{\rho_{Ag,300} l}{x_{Ag} A} I_t \qquad (2.1)$$

where l is the length of the heater. A is the area of the conductor, x_{Ag} is the fraction of silver in the conductor, I_t is the transport current, and $\rho_{Ag,300}$ is the resistivity of silver at 300 K.

The supply leads are clamped to the current lead outlets extending from the flange that joins the cryocooler with the cryostat. The outlets are 1/4 inch diameter copper pins. They are electrically isolated from the stainless steel flange and sealed with epoxy. Inside the cryostat, copper cable connects the current lead outlets with the HTS leads. The cable is wrapped several times around the cryocooler to reduce heat conduction into the HTS leads.

2.3.2 HTS Current Leads

Two pairs of silver-sheathed BSCCO-2223 tape strips carry the current from the copper cable to the test magnet's aluminum mesh leads. The use of HTS tapes, as opposed to copper cables, reduces heat dissipation. The HTS tape strips are adhered flush against opposite sides of the copper extension rod. The conductor is manufactured by Sumitomo Electric and rated 42 A at 77 K.

Before attaching the leads, 20 μm thick Kapton tape is placed over the copper extension rod to electrically insulate the HTS leads. The HTS tape is adhered to the Kapton with Stycast epoxy, providing a good thermal contact. A second layer of Kapton covers the HTS leads to prevent shorts.

Table 2.1: Test magnet dimensions.

	Inner Coil	Outer Coil
Inside Diameter [mm]	100.0	105.8
Outside Diameter [mm]	104.6	111.6
Wind Height [mm]	76.0	76.0
Total Turns	160	200
Layers	8	10
Turns/Layer	20	20
Conductor Length [m]	52	69
Self Inductance [mH]	2.14	3.55
Mutual Inductance [mH]	2.57	2.57
Center Field @100A [T]	0.16	0.19
Peak Field @100A [T]	0.20	0.25
λJ @100A [A/m^2]	9.21×10^7	8.98×10^7

Table 2.2: Conductor specifications.

	Inner Coil	Outer Coil
Conductor Width [mm]	3.5	3.5
Conductor Thickness [mm]	0.23	0.23
I_c(77 K, 0 T) [A]*	23.5	19.9
Silver Fraction	0.70	0.70

*criterion of $E_c = 0.1\mu V/cm$.

2.3.3 Construction Details of the Test Magnet

A detailed drawing of the test magnet, manufactured by Sumitomo Electric, and its heat lead connection is shown in Figure 2-3. The magnet consists of two concentric coils of equal height and the same wind direction. The outer and inner coil conductors have different critical currents(different quality), but the same cross-section. The coils were wound dry(without epoxy) on a copper coil form. Tension in the conductor is maintained by double stick pads applied to the conductor at the end of each layer. The conductor is wrapped once in 25 μm thick Kapton insulation, as depicted in Figure 2-4. There effectively are three layers of Kapton between each layer of conductor. Dimensions of the test magnet are listed in Table 2.1. Conductor specifications are given in Table 2.2.

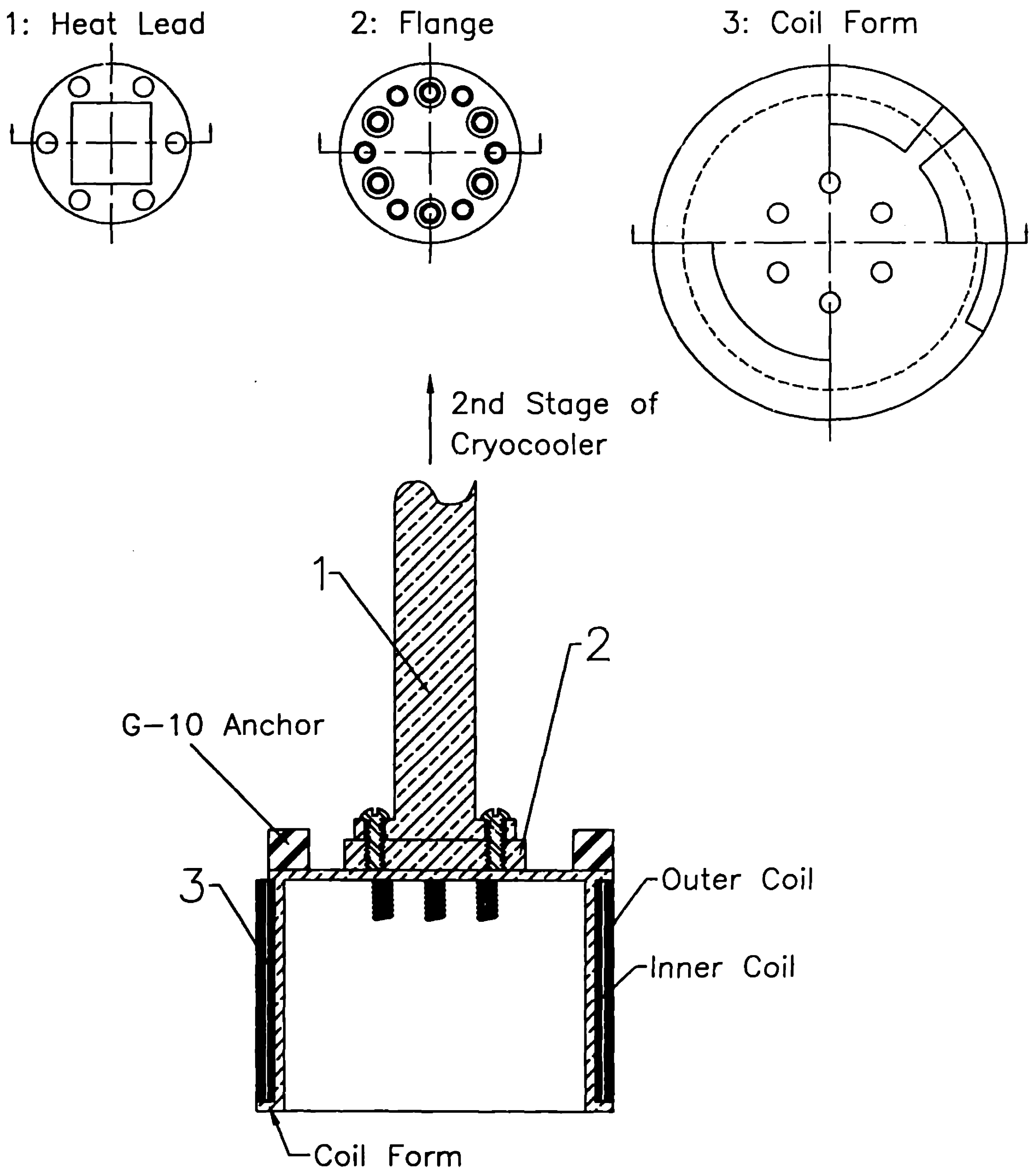

Figure 2-3: Detailed drawing of the test magnet coupled to the heat lead. Parts 1, 2, and 3 are all made of copper, facilitating thermal coupling between the 2nd stage of the cryocooler and the test magnet coil form.

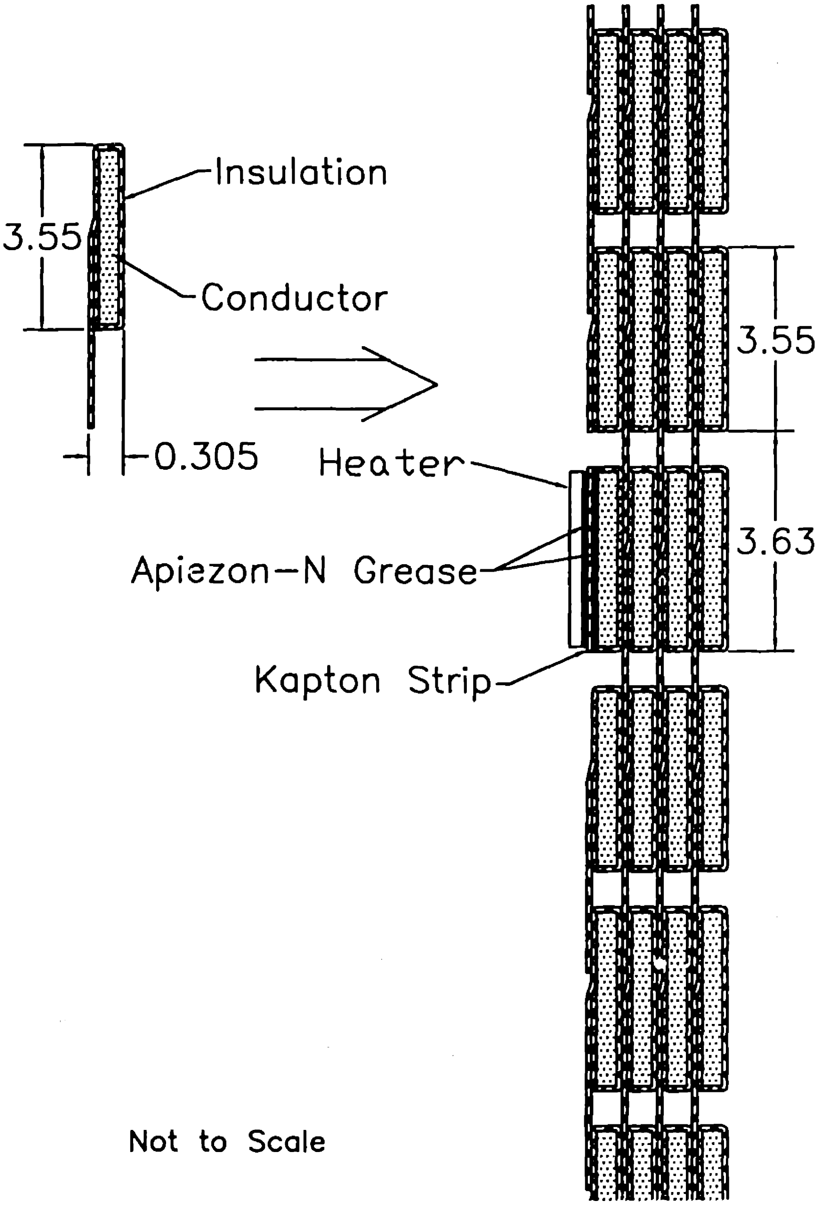

Figure 2-4: Detail of insulation. Dimensions in mm.

Soldesign, a solenoid design computer program, is used to calculate the field profile and inductances. For a transport current of 100 A, the test magnet generates a centerline field of 0.35 T, and a peak field of 0.45 T.

As may be inferred from Figure 2-3, the test magnet coil form material and parts that connect the coil form and the second stage of the cryocooler are all made of copper, facilitating thermal coupling of the test magnet to the cooling source. Additionally, the copper's high thermal conductivity helps maintain a constant temperature throughout the winding.

The ends of the conductor extend through the top of the coil to G-10 anchors, where they are soldered to aluminum mesh that is connected to the HTS leads, as shown in Figure 2-1. The quench heater is attached over a single turn of the outer coil's outermost layer, extending about 6.0 cm less than a full turn. Figure 2-5 is a schematic drawing of the outermost layer, indicating the locations of the heater and voltage taps attached. Taps are placed to measure voltages across the following regions, as shown in Figure 2-5: 1. the heated turn; 2. one turn above the heated turn; 3. one turn below the heated turn; 4. the entire second layer (20 turns); 5. the entire outermost layer (20 turns) including those 3 individually monitored turns; 6. between lower end of heater and lower heated turn tap; 7. between upper end of heater and upper heated turn tap; 8. outer coil (160 turns); 9. inner coil(200 turns).

2.3.4 Voltage Taps

Each voltage tap is a 3-mm wide strip of copper shim, slipped beneath the Kapton insulation. The contact is secured using BIPAX silver epoxy; an epoxy, instead of solder, is used to avoid excessive heating that may damage the conductor. Copper leads from the 32-pin connector are soldered to the free end of the copper shim strip. The leads are wrapped around the cryocooler and the copper extension rod to reduce conductive heat transfer.

2.3.5 Quench Heater

The quench heater is a 3.4 mm wide(same as the conductor) by 33 cm long strip of 13μm thick stainless steel shim. The Kapton insulation is removed from the heated turn and replaced by a single strip of 3.5 mm wide Kapton. Care is taken not to allow contact with

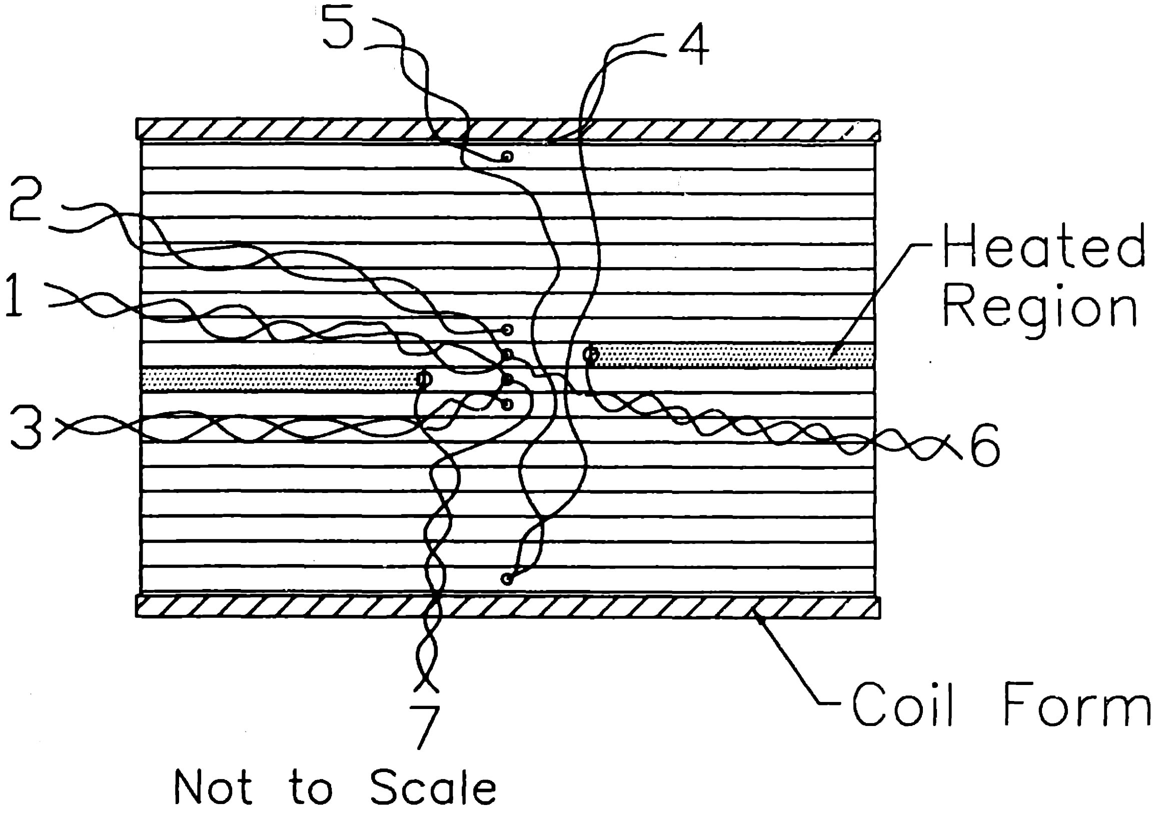

Figure 2-5: Heater and tap positions. 1) heated turn; 2) one turn above the heated turn; 3) one turn below the heated turn; 4) the entire second layer; 5) the entire outermost layer; 6) between lower end of heater and lower heated turn tap; 7) between upper end of heater and upper heated turn tap.

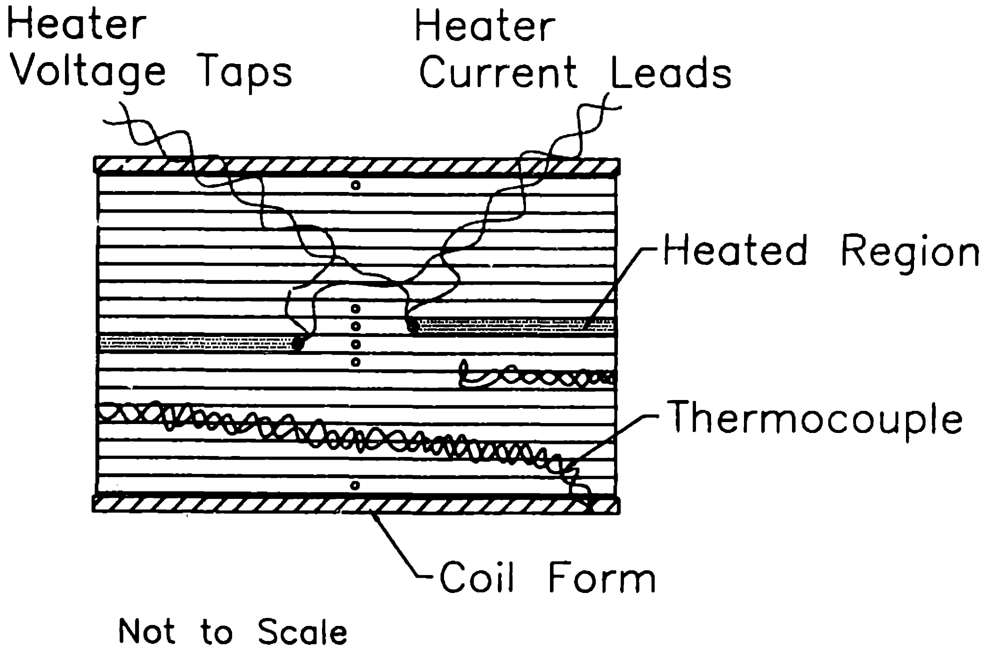

Figure 2-6: Location of the heater and the thermocouple.

adjacent turns in order to isolate the heating to one turn. Apiezon-N grease is applied to the conductor to provide a good thermal contact and hold the Kapton strip in place. The quench heater is fixed in place with a layer of Apiezon-N grease that is applied to the outer surface of the Kapton strip, as shown in Figure 2-4. A thin layer of solder is applied over 2 cm of each end, isolating the heating within 3.0 cm of each end of the heated turn, as shown in Figure 2-5. The thermal grease beneath the nonresistive regions of the heater ends is removed. A tiny amount of Stycast epoxy is applied at the heater ends to hold them flat and maintain slight tension in the heater.

Two lead pairs are attached to each end of the heater, one of each pair carries current, the other is used to measure the voltage. The current leads consist of a twisted pair of 22-gauge wire extending to the heater supply via the 32-pin connector. The heater power supply is rated 3A at 15 V. A pulse is produced using a relay placed in series with the quench heater. The relay is controlled by a pulse generator as depicted in Figure 2-2.

2.3.6 Temperature Control Heater

A heater for controlling the temperature of the test magnet enfolds the second stage of the cryocooler. It consists of 20 turns of manganin wire, wrapped into a layer of Apiezon-N thermal grease. At 20 K, the heater has a resistance of 19.9 Ω. A power supply outputs 3.1 W to the heater to achieve a coil form temperature of 20 K, 6.1 W for 30 K, and 7.7 W for 40 K.

2.3.7 Temperature Measurement

Temperature of the coil form is measured with a calibrated Lakeshore Cryogenics GaAlAs thermodiode. The diode sits in a 2.0 mm diameter by 1.5 mm deep recess, at the bottom of the copper coil form. The recess is filled with Apiezon-N thermal grease. A pair of leads are connected to each diode contact, one to carry current, the other to measure voltage. Control current is supplied by a calibrated Lakeshore Cryogenics current source.

A type E thermocouple extends between the conductor and the coil form, near the thermodiode, measuring their temperature difference. The reference contacts are located on the coil form. They are separated from the metal by a strip of Mylar tape to keep them electrically isolated. The measurement contact is located $1\frac{1}{4}$ turns below the heated turn as shown in Figure 2-6. It is inserted beneath the conductor insulation and in direct contact with the conductor. Apiezon-N grease is applied to the contact region at all thermocouple ends.

Before determining the conductor operating temperature, the thermodiode and thermocouple output are allowed to reach steady state. We begin calculating the temperature by assuming that the thermocouple reference end and the thermodiode are at the same temperature. Using a calibration table to find the thermodiode temperature, an equivalent voltage is assigned from a thermocouple reference table. The thermocouple measurement end temperature is then determined by adding this voltage to the reference end voltage and converting with the reference table.

2.3.8 Instrumentation

Voltage measurements are sampled with Labview Software on a Macintosh digital computer. The computer receives inputs from a National Instruments A/D converter. Amplifiers and filters are built into the A/D converter. We used amplification in the range 1–1000, and 10 kHz filtering. Voltage tap outputs, thermodiode voltage, quench heater voltage, and transport current are sampled using a rate of 100 Hz for each trial. Voltages are monitored in real time using Keithley 175, 191, and 197 voltmeters.

2.4 Procedure

After the cryocooler is turned on and the test magnet reaches a steady state temperature, the nitrogen space is filled with liquid nitrogen. The second stage heater power supply is then set to the appropriate voltage for the desired operating temperature. The heater power must be adjusted periodically over a 6 hour period while allowing the temperature gradient between the conductor and the coil form to subside. Typically, there is a 6 K temperature difference between the conductor and the coil form at steady state.

The following steps illustrate how each trial is conducted:

1. The variable amplifier is set to trip the protection relay at V_{off}, calculated from Equation 2.1.
2. The heater supply is momentarily disconnected from the heater. The pulse is sampled to check its duration and magnitude.
3. The transport current is ramped slowly up to its desired value.
4. Output sampling is initiated. After 4 seconds, the heater is pulsed.
5. Current may be shut off manually or by the protection relay. The next trial does not begin for at least 120 minutes.

Operating parameters for each trial are listed in Table 2.3. Parameters are chosen to illustrate the radical difference in response caused by changing the operating temperature or

Table 2.3: Operating parameters for each trial

Trial	T_o [K]	I_t [A]
1	23.8	80
2	23.6	100
3	33.5	60
4	33.5	80
5	49.4	50
6	50.0	60

operating current. A heater pulse of approximately 18 W for 0.5 s is used for every trial.

Figures 2-7 and 2-8 are two examples of voltage traces for different transport current and operating temperatures: (a) 100 A at 23.6 K, and (b) 80 A at 23.8 K. The first example trace depicts a quench, while the second depicts a recovery. The entire set of voltage traces corresponding to the trials listed in Table 2.3 are shown in Chapter 4. In all trials, the inner coil voltage remains constant. Judging by the small voltage rise in the second layer, the quench never reaches the third layer. It is also observed that the quench never reaches the turns in the outermost layer that are adjacent to the heated turn.

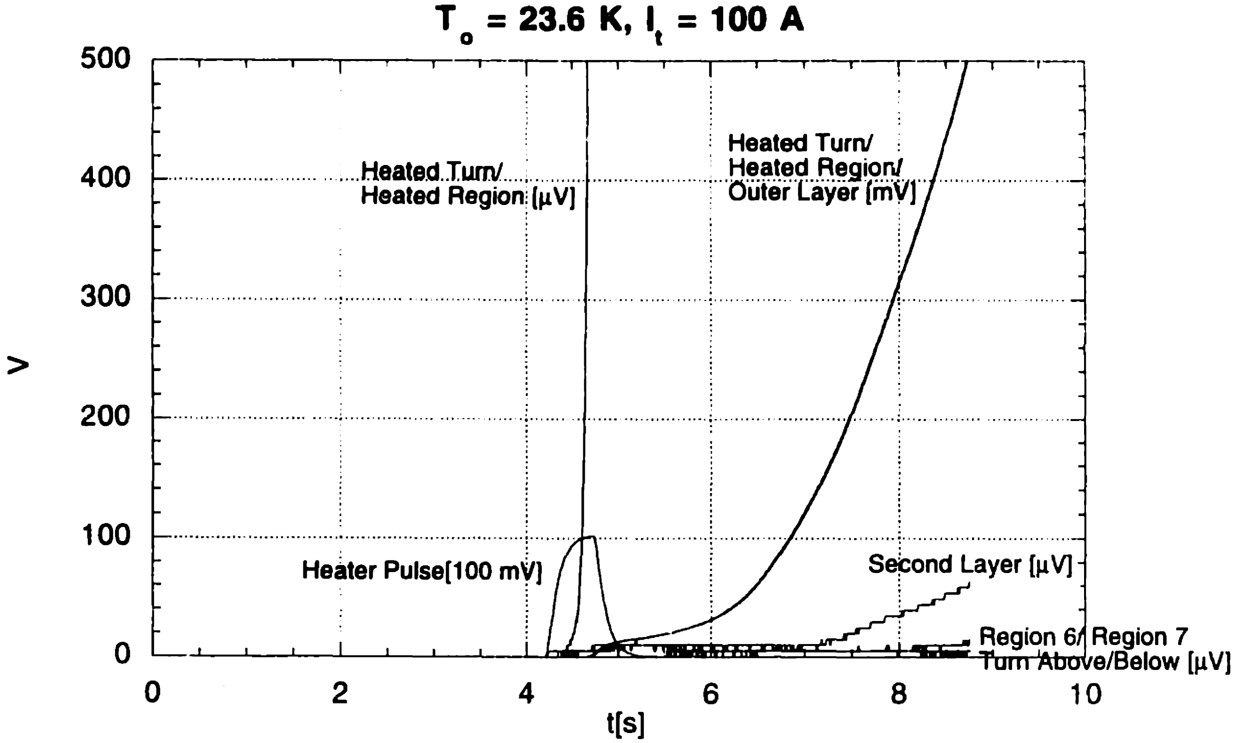

Figure 2-7: Voltage trace for $I_t = 100$ A and $T_o = 23.6$ K (trial 2). Regions 6 and 7 refer to the small conductor lengths just outside the heated region, depicted in Figure 2-5(pg.17).

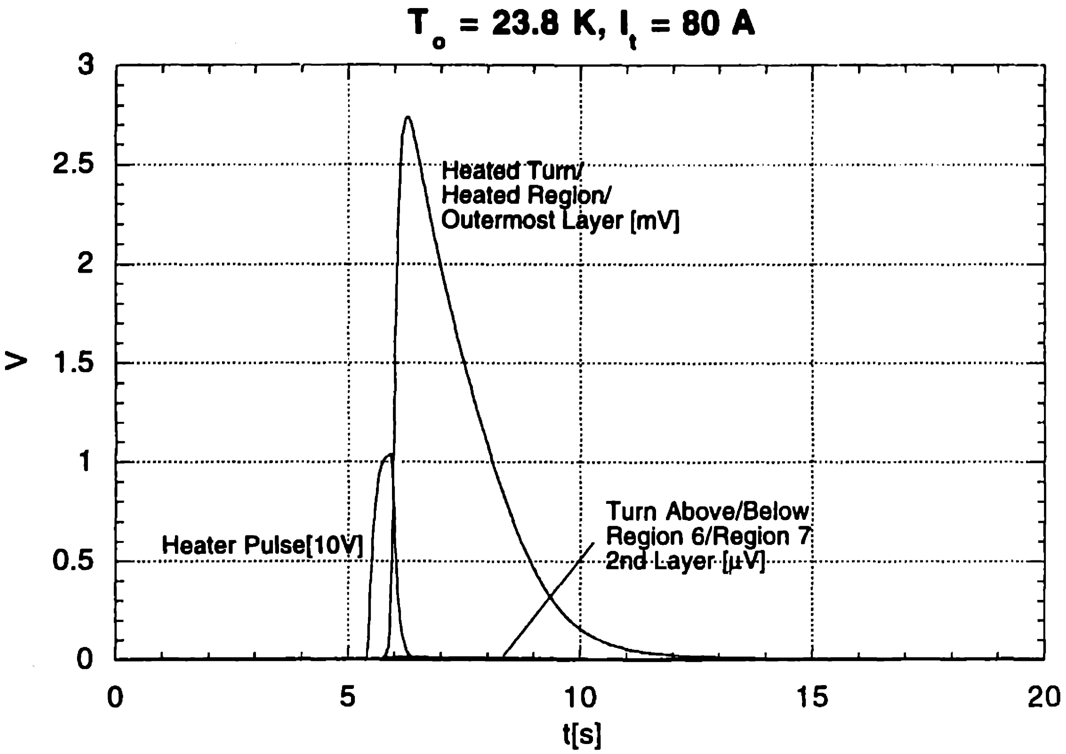

Figure 2-8: Voltage trace for $I_t = 80$ A and $T_o = 23.8$ K (trial 1).

Chapter 3

Numerical Model

3.1 Normal Zone Propagation

Typical conductor consists of superconducting filaments embedded in a conductive metal matrix. The matrix serves multiple purposes: it provides a conductive path when the superconductor is normal, helps maintain a uniform temperature across the conductor cross-section, and promotes thermal diffusion along its length. When a superconducting magnet operates below its critical current, I_c, the transport current flows entirely through the superconducting filaments, creating minimal heat dissipation. However, if an external energy source causes additional dissipation in a localized region, the temperature in that region will rise and the critical current decreases. Given a large enough heat input, the temperature will enter the current sharing region, at T_{cs}, when the critical current is less than the operating current. At this point, the operating current redistributes itself. The current in excess of the critical current flows through the metal matrix. Current flow through the resistive matrix causes Joule dissipation which may continue to increase the temperature, and decrease the critical current if the heat is not conducted away by the matrix fast enough. If the region recools, the quench "recovered". If the temperature of the heated region climbs indefinitely, a normal region propagates into the superconducting region of the coil. Whether the quench recovers or propagates depends on the size of the heated region, the initial heat input, thermal properties of the conductor and insulation, and the operating conditions-transport current, temperature, and field. If it propagates, the conductor's temperature can continue to rise unless the current is shut off. Therefore, we require an accurate model of the normal zone propagation(NZP) for designing the protection of superconducting systems. Specifically, a model will help answer the following questions:

1. Will the magnet quench by a specific heat dissipation, considering its magnitude and location(s)?
2. What type of protection system is required to ensure that the magnet will never be damaged?
3. What voltage magnitude across a specific length of conductor indicates a nonrecovering quench that will propagate and potentially damage the magnet?

Normal zone propagation is a thermal event that may be modeled using the transient heat conduction equation. Thorough work has been performed over the last three decades to model NZP in low-temperature superconducting magnets. For these magnets, the operating temperature, T_o, is typically only a few kelvins below the critical temperature, T_c. The small superconducting to normal transition permits us to represent the NZP by propagation speeds of a boundary between superconducting and normal regions, as shown in Figure 3-1. Two commonly specified are the longitudinal velocity(along the tape axis), U_l, and the azimuthal velocity(along the radius of the coil), U_t. There are two important consequences of the small superconducting to normal temperature difference that enables this simple modeling:

1. Thermal properties, which are strongly a function of temperature, do not vary significantly in the region of interest.
2. The current sharing region, where the conductor is still superconducting, but the operating current exceeds the critical current, exists in a very small region of space. Hence, the boundary between superconducting and normal regions is well defined.

High-Tc superconductors typically do not meet these conditions, as described below.

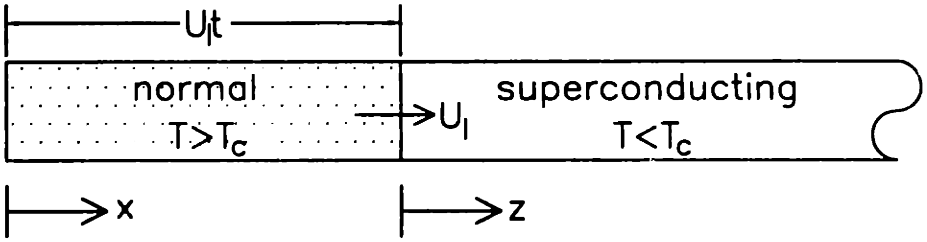

Figure 3-1: Model for low-Tc NZP.

3.1.1 Current Sharing Region

Critical current density, J_c, is shown as a function of temperature and magnetic field in Figure 1-1 for BSCCO-2223 and NbTi. During the beginning of a quench for the high-Tc case, heat dissipation is caused by current sharing. Current sharing begins at the temperature, T_{cs}, where the transport current, I_t, is equal to the critical current, I_c. As the temperature increases from T_o through T_{cs}, dissipation increases as I_c decreases and more current flows through the matrix. The difference between T_{cs} and T_c is typically on the order of tens of kelvins. Eventually, when T_c is surpassed, the rate of heat dissipation depends only on transport current density, matrix resistivity, and the matrix cross-sectional area.

As stated above, for low-Tc, the temperature difference between T_o and T_c is only a few kelvins. A relatively small amount of heat will drive the conductor completely normal, with negligible time spent in the current sharing region. This allows the simpler model of separating the conductor into two regions as depicted in Figure 3-1 for one-dimensional NZP in which the normal-to-superconducting boundary propagates along the conductor length. The boundary between the normal and superconducting regions moves into the superconducting region as the quench progresses. This basic model has been verified to be applicable even in a Nb-Ti solenoidal system in which normal zone propagation can be three-dimensional.[4]

3.1.2 Temperature Dependent Properties

The electrical and thermal properties of silver, the matrix metal of the conductor used in this experiment, are strongly temperature dependent. Between 20 K and 100 K electrical resistivity, thermal conductivity, and heat capacity all change by a factor of ten or greater(see Figures 3-6,3-8,3-9). In modeling a high-Tc quench, the change in properties are important because the conductor is not completely normal until it reaches approximately 100 K. Our modeling task is complicated by this as the coefficients of the heat equation and the heat dissipation term vary nonlinearly. Therefore, the ODE describing the thermal event cannot be solved analytically.

3.2 Quench Velocity Estimation

Despite the nonlinear temperature dependence of the conductor's thermal properties, we can still make an order of magnitude estimate of the longitudinal quench velocity. We use an equivalent method to the one used for low-Tc predictions. The method begins with the one-dimensional form of the heat equation:

$$c\frac{\partial T(x,t)}{\partial t} = \frac{\partial}{\partial x}\left[k\frac{\partial T(x,t)}{\partial x}\right] + g(T,x) \tag{3.1}$$

where T is temperature, c is specific heat capacity, k is thermal conductivity, and g is internal heat dissipation density. The left-side term is the rate of change in thermal energy density at a point a distance, x, along the conductor. The first term in the right-hand side represents the local thermal conduction density.

Internal heat generation is the result of the transport current flowing down a voltage gradient, $\partial V/\partial x$:

$$g(T,x) = I_t\frac{\partial V}{\partial x} \tag{3.2}$$

When the critical current is larger or equal to the operating current, there is theoretically no voltage gradient and $g(T,x)$ is zero. During current sharing, the voltage gradient is given by the product of the current flowing in the matrix and the matrix resistance per length:

$$\frac{\partial V}{\partial x} = I_m\frac{\rho_m}{x_m A_{cd}} \tag{3.3}$$

where A_{cd} is the total cross-sectional area of the conductor, $x_m A_{cd}$ is the cross-sectional area of the matrix material, ρ_m is the matrix resistivity, and I_m is the current flowing through the matrix. I_m is the difference between the transport current and the critical current, $I_t - I_c$. Therefore,

$$\frac{\partial V}{\partial x} = (I_t - I_c)\frac{\rho_m}{x_m A_{cd}} \tag{3.4}$$

Using Equation 3.2, we have:

$$g(T,x) = I_t(I_t - I_c)\frac{\rho_m}{x_m A_{cd}} \tag{3.5}$$

In the normal state, all of the current flows through the matrix, assuming the resistivity of the normal superconductor is much larger than the resistivity of the matrix. Replacing I_c with zero in Equation 3.5, we have:

$$g(T,x) = I_t^2 \frac{\rho_m}{x_m A_{cd}}. \tag{3.6}$$

For this simple approximation, we will ignore the current sharing region. The conductor is separated into two distinct regions in x, one superconducting and one normal as shown in Figure 3-1. We begin solving for velocity by introducing a change of variables, $z = x - U_l t$, where z is the position relative to the superconducting to normal boundary. Positive z extends into the superconducting region. Two ordinary differential equations are obtained by substituting the transform into the heat equation. The first applies to the superconducting region:

$$k_s \frac{d^2T}{dz^2} + \frac{dk_s}{dT}\left(\frac{dT}{dz}\right)^2 + c_s U_l \frac{dT}{dz} = 0 \tag{3.7}$$

For the normal region:

$$k_n \frac{d^2T}{dz^2} + \frac{dk_n}{dT}\left(\frac{dT}{dz}\right)^2 + c_n U_l \frac{dT}{dz} + g(T,z) = 0 \tag{3.8}$$

where s and n denote superconducting and normal regions, respectively. An approximate solution for U_l was obtained by Cherry and Gittleman[5] as:

$$U_l = J\sqrt{\frac{\rho k_s}{C_s C_n \Delta T}} \tag{3.9}$$

where ρ is the resistivity in the normal state, J is the current density, and ΔT is equal to the difference in critical and operating temperature, $T_c - T_o$.

Equation 3.9 assumes constant properties and no matrix. In this experiment, we used silver-sheathed BSCCO-2223 conductor that is approximately 70% silver by volume; 73% is used in the simulation. It has a critical temperature of approximately 110 K; however, the critical current is negligible around 90 K. Below, we estimate the propagation velocity for T_o equal to 20 K, and J equal to 12.4×10^3 A/cm^2. For a rough approximation, we may use average property values between T_o and T_c. The following is a list of the appropriate property values and their justifications for T_o equal to 20 K:

- ρ: The resistivity of BSCCO-2223 is larger than that of silver by 3 orders of magnitude. Since the superconductor and the matrix conduct in parallel, the average resistivity, $\tilde{\rho}$ is approximately the resistivity of silver divided by the volume fraction that is silver, x_{Ag}. Between T_o and T_c, $\tilde{\rho} = \tilde{\rho}_{Ag}/x_{Ag} = 9.32$ nΩcm.

- k_s: The thermal conductivity of silver is 2 orders of magnitude larger than for BSCCO-2223. They conduct in parallel, so k_s is very close to the average thermal conductivity of silver multiplied by x_{Ag}, $k_s = x_{Ag}\tilde{k}_{Ag} = 14.5$ W/cm K.

- C_n, C_s: The heat capacity of BSCCO-2223 is on the same order of magnitude as silver's. We will use the average heat capacity of silver because the conductor is mostly silver. There is no significant difference between the superconducting and normal states. $C_n = C_s = \tilde{C}_{Ag} = 0.2$ J/cm^{3}K.

- ΔT: The effective T_c is approximately 90 K. For $T_o = 20$ K, $\Delta T = 90\text{ K} - 20\text{ K} = 70$ K.

Inserting these values into Equation 3.9, we find that U_l is approximately 2.7 cm/s. This is 3 orders of magnitude smaller than a low-Tc propagation velocity, typically on the order of 10–100 m/s. The slower velocity indicates smaller temperature gradients and we cannot assume the current sharing region to be negligibly small in space. However, the simulation used to model the experimental results presented in Chapter 4 predicts U_l to be 1.7 cm/s, which is not too far off from the value calculated by Equation 3.9.

A similar analysis yields an approximate quench velocity in the transverse direction (normal to the conductor), U_t. Typically, there is electrical insulation between the layers, causing a much slower propagation velocity. The following expression may be used for U_t[6]:

$$U_t = \frac{J_m}{\tilde{C}_{cd}}\sqrt{\frac{\rho_m k_i \delta_{cd}}{2\delta_i \Delta T}} \tag{3.10}$$

where $\tilde{C}_{cd}$ is the mean heat capacity of the conductor between T_o and T_c, k_i is the thermal conductivity of the insulation, and δ_{cd} and δ_i are the thicknesses of the conductor and insulation, respectively. The insulation heat capacity does not appear because the heat capacity of conductive metals is much larger than that of organic materials. Likewise, the conductor thermal conductivity does not appear because the insulation provides a much larger conduction resistance than the conductive metals. Thermal property data for Kapton insulation is unavailable. However, the thermal conductivity of organic materials does not greatly vary and we may estimate k_i to be 0.003 W/cmK. δ_i and δ_{cd} are 75 μm and 230μm, respectively. Using these values, we estimate U_t to be 0.05 cm/s. This velocity is greatly overestimated because we have neglected the significant contact resistances associated with dry wound magnets, described in Section 4.2.

3.2.1 Minimum Quench Heat

Stekly has derived an expression for estimating the minimum quench heater power, q_h[7]:

$$q_h = \frac{8\pi}{3}(k_x k_y k_z)^{1/3} r_h \Delta T \tag{3.11}$$

where k_x, k_y, and k_z are the thermal conductivities along cartesian axes, and r_h is the radius of the heated region. Since we are dealing with a two-dimensional model for tape conductor, this equation may be modified to[3]:

$$q_h = \frac{4\pi}{3}(k_r k_\theta)^{1/2} w \Delta T \tag{3.12}$$

where, k_r and k_θ are the thermal conductivities in the transverse and azimuthal directions respectively, and w is the conductor width. Using $k_\theta = k_{Ag}$ and $k_r = k_i$ at 20 K, $w = 3.5$ mm, we estimate q_h to be, 5.3 W. This is a little over one third of the heater power used in this experiment. It is apparent that high-Tc conductors are far more thermally stable than low-Tc, where q_h values are on the order of microwatts.

3.3 Numerical Model

Even for low-Tc superconductors, numerical modeling of NZP shows significant improvement over analytical methods, as demonstrated by Kadambi and Dorri[8] and Eckert et al[9, 10]. For the high-Tc case, the wide temperature span of the current sharing region and the large variation of the thermal properties over this region make numerical methods essential. One-dimensional numerical analysis have been performed for high-Tc tapes using the finite difference method. In particular, Bellis and Iwasa[11] have developed a one-dimensional finite difference code for silver-sheathed BSCCO-2223 tapes. Lim[3] has developed a two-dimensional code for single-pancake coils, and obtained results that agree well with experimental results. Here we develop a two-dimensional code for a three-dimensional coil.

3.3.1 Finite Difference Method

Modeling the spatial variation of an implicit property across an object involves representing the object by a fine nodal mesh. Each node, corresponding to a small region(finite element) of the object, has relevant properties and at least one control variable associated with it. In our case, the control variable is temperature. The simulation proceeds through sufficiently small time steps. For each time step, the value of the control variable at each node is calculated for the next time step based upon property and control variable values of the surrounding nodes.

Various finite-difference algorithms are available. However, when used properly, each should yield identical results. The algorithms are classified into two categories. The implicit method (backward-difference) uses the control variable values at both the present and next time step to calculate the value for the next time step. The explicit method (forward-difference) requires only the present property and control variable values to calculate the value for the next time step. The implicit method requires much more computation per iteration, causing it to be time-consuming. Therefore, we will use the explicit method. However, we must pay special attention to the mesh sizes and the time step. The main disadvantage to the explicit method is its tendency to be unstable or yield faulty results when the mesh size or time step is too large.

3.3.2 Mesh Geometry

Although the coil construction is three-dimensional, there is a gap between successive turns, preventing heat conduction in the axial direction. Therefore, we will base the simulation on a two-dimensional form of the heat conduction equation. We model the heated region by individual linear strips sandwiched together as shown in Figure 3-2. The layers of conductor correspond to different layers of the coil. The wind construction, as shown in Figure 2-4, requires us to place 3 layers of insulation between layers of conductor, and 2 layers separating the heater from the outermost conductor layer.

There are three key conditions that allow us to represent the quench region using this geometry:

1. There are many turns between successive layers in the affected region. Simulation reveals that throughout the quench, there is negligible temperature change less than a turn away from the heated turn. Therefore, heat conduction along the tape and into successive layers can be neglected.

2. The thickness of the conductor and insulation is much smaller than the radius of the coil. Although the coil is solenoidal, local geometry is effectively linear.

3. Temperature gradients along the conductor in the second layer is much smaller than the

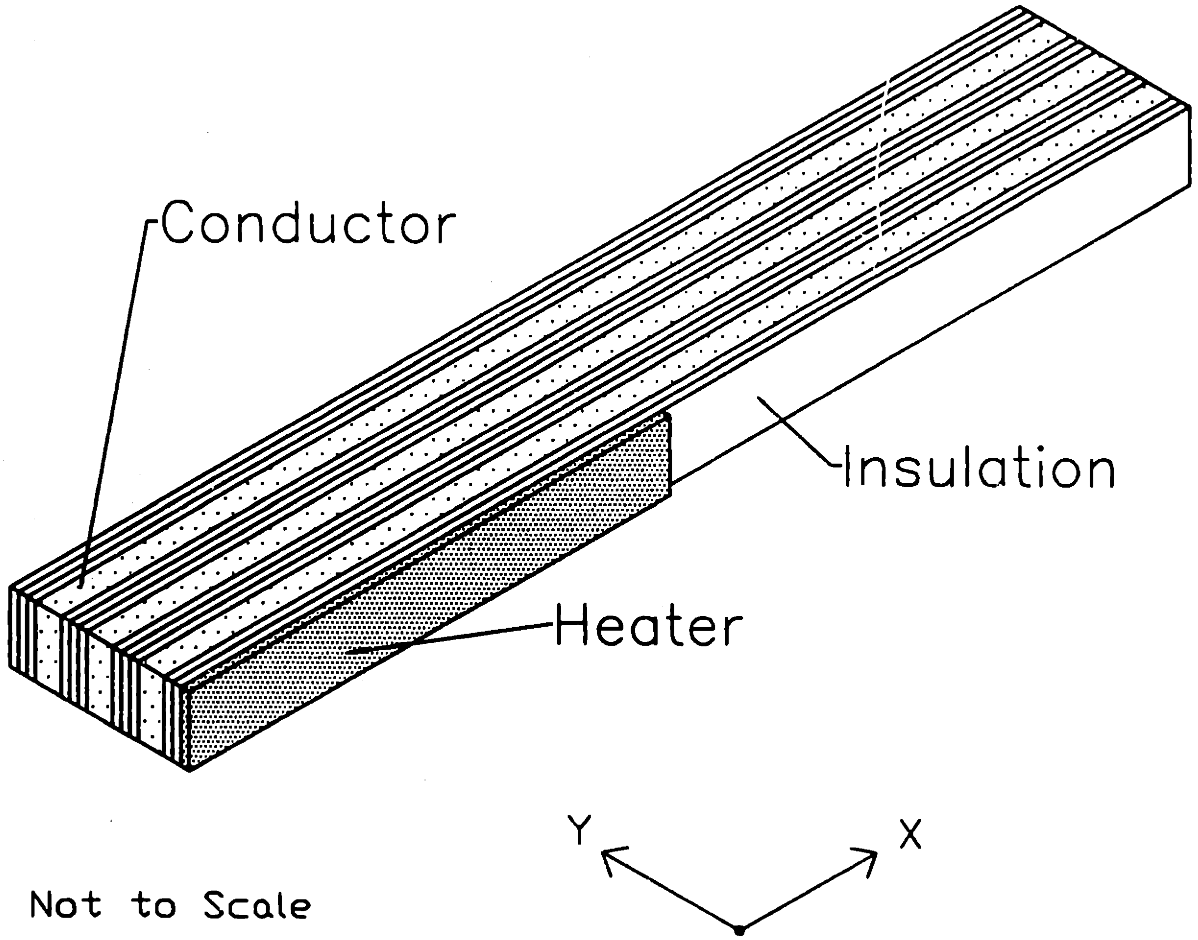

Figure 3-2: Model of heated region used in the simulation.

gradients between the outer two conductor layers. Although the successive layers are actually criss-crossing helixes, our model still calculates the heat conduction between the layers properly. However, the distribution of the flux requires some correction (see Section 3.3.3).

We actually model just half of the heated region because there is a line of symmetry at the midpoint of the heater. Figure 3-3 depicts a mesh for numerically modeling the arrangement shown in Figure 3-2. The resistance elements represent contact resistance between different layers. Each node is given a coordinate, (m, n), where m increases in the longitudinal (x) direction and n increases in the azimuthal (y) direction.

3.3.3 Layer-to-Layer Heat Conduction

Successive layers are not aligned on top of each other as the model implies (Figure 3-2), but are actually criss-crossing helixes. According to the simulation, thermal gradients are small in the inside layers. Therefore, heat flux from the outermost layer into the winding (y-direction) is calculated with reasonable accuracy. However, its distribution across the second layer may be in error.

If the outer two layers are cut along a vertical line and unwound on a flat surface, the turns will be arranged as in Figure 3-4. There is one turn in the second layer that shares half of its surface area with the heated turn. More importantly, the hottest portion of the heated turn lies in this shared area. The second layer turns that are adjacent to the turn that lies below the heated turn do not give a voltage contribution just as the first layer turns adjacent to the heated turn do not. Furthermore, heat conduction into these turns is at significant distance from the affected region. For the purpose of calculating voltage rise in the second layer, we need only be concerned with heat conduction from the heated turn to the second layer turn directly below it. The algorithm may be improved by accounting for the reduction in shared surface area between the two turns as m increases.

The area shared, A_{sh}, between two nodes of the same m value, one corresponding to the inside insulation of the heated turn (n=3) and the other the outside insulation of the second

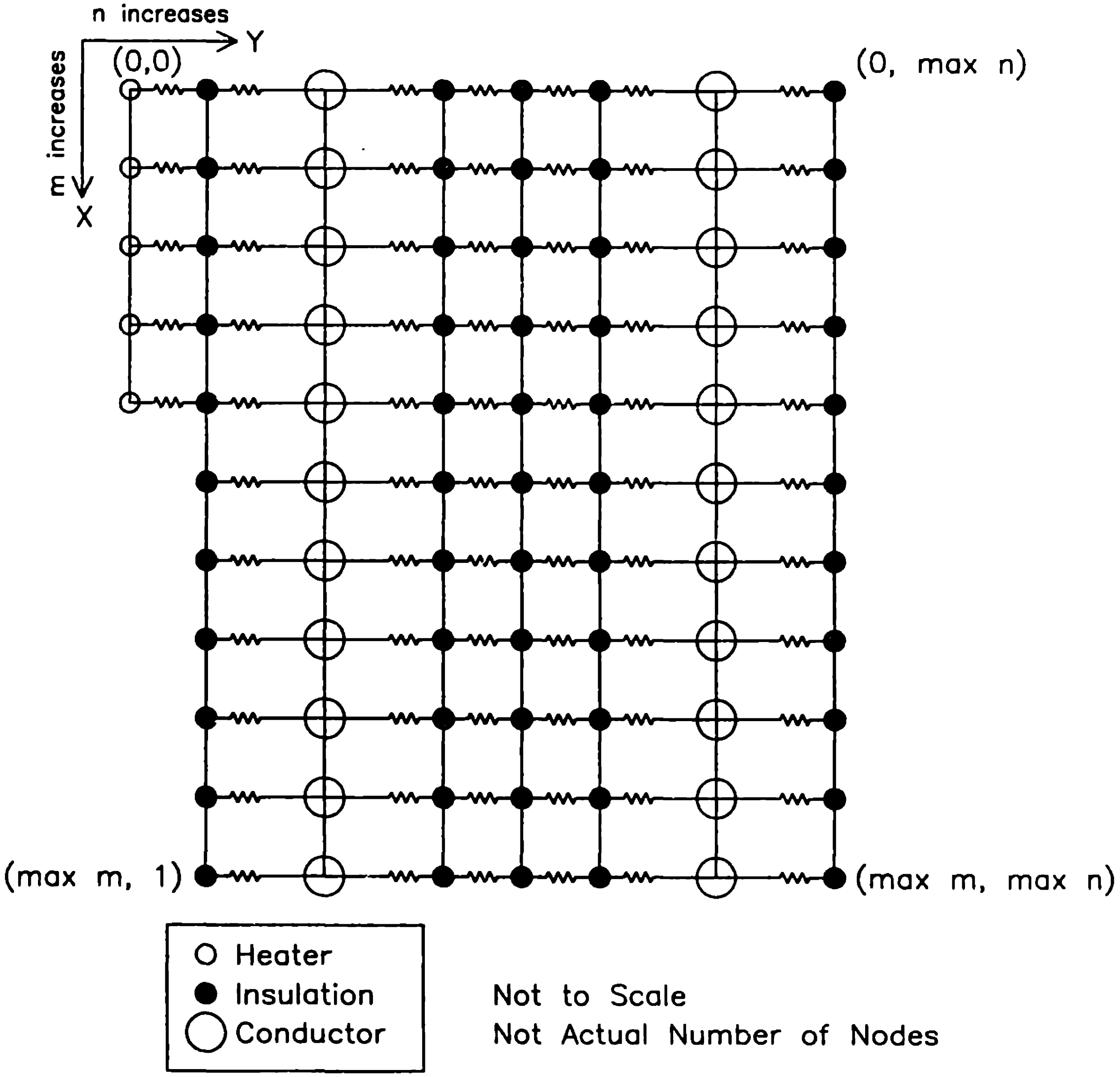

Figure 3-3: Mesh used in the simulation to represent the heated region.

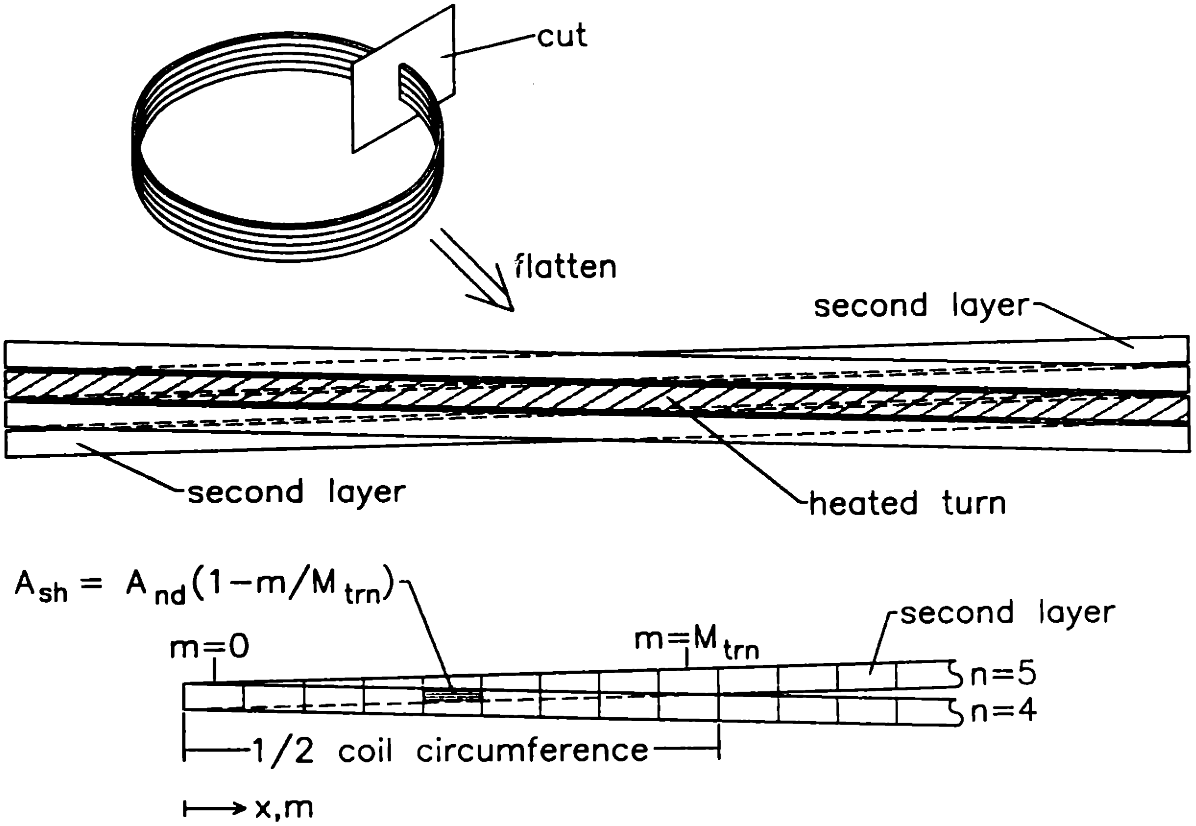

Figure 3-4: Contact area between successive layers, A_{sh}, for each node in terms of surface area of a node, A_{nd}, number of nodes per turn, M_{trn}, and the x-direction nodal coordinate, m.

layer (n=4), is given by:

$$A_{sh} = A_{nd}\left(1 - \frac{m}{M_{trn}}\right), m < M_{trn} \tag{3.13}$$

where A_{nd} is the radial surface area of a single node and M_{trn} is the total number of nodes per turn. Heat flux across the layer is corrected by multiplying by the area ratio, A_{sh}/A_{nd}.

3.3.4 Boundary Conditions

We expect heat input from outside the test magnet to be small because the magnet is housed in a high vacuum cryostat while liquid nitrogen is used to cool the sample space walls, reducing radiation. Radiation is estimated to be on the order of milliwatts. Therefore, the system has been modeled as adiabatic, where the outer surfaces of the outside nodes of the mesh do not transfer heat. It is likely that some of the heater energy is conducted away through the heater leads. Energy loss to the leads is estimated in Section 4.4 to be approximately 5 mJ, assuming the leads remain at T_o throughout the trial. The total dissipation in the heater is on the order of 9.5 J, which is much larger than conduction through the heater ends. Therefore, the entire test magnet assembly is modeled as adiabatic.

We choose enough layers and nodes to permit the last layer and the end nodes farthest from the heater to experience insignificant temperature change (less than 0.2 K) throughout the trial. The outside surface of these nodes are adiabatic, as would be the case if the temperature difference across them is negligible.

3.3.5 Numerical Form of the 2-D Heat Equation

The Cartesian form of the 2-D heat density equation applies to our model:

$$c\frac{\partial T}{\partial t} = k\left(\frac{\partial^2 T}{\partial x^2} + \frac{\partial^2 T}{\partial y^2}\right) + g(x, y, t) \tag{3.14}$$

where c is the volumetric heat capacity, k is the thermal conductivity, g is the heat dissipation term, and t is time. We can convert this partial differential equation into a numerically usable form by substituting Taylor expansions for the partial differentials. The following

Taylor expansions pertain:

$$\frac{\partial T}{\partial t} \cong \frac{T^{i+1}_{m,n} - T^{i}_{m,n}}{\Delta t} \tag{3.15}$$

$$\frac{\partial^2 T}{\partial x^2} \cong \frac{T^{i}_{m+1,n} - 2T^{i}_{m,n} + T^{i}_{m-1,n}}{(\Delta x)^2} \tag{3.16}$$

$$\frac{\partial^2 T}{\partial y^2} \cong \frac{T^{i}_{m,n+1} - 2T^{i}_{m,n} + T^{i}_{m,n-1}}{(\Delta y)^2} \tag{3.17}$$

where Δt is the time step, Δx and Δy are the mesh sizes in the longitudinal and azimuthal directions respectively, i denotes which time step, and (m, n) is the nodal coordinate (see Figure 3-3). Substituting Equations 3.15 – 3.17 into Equation 3.14, we obtain:

$$c^{i}_{m,n}\frac{T^{i+1}_{m,n} - T^{i}_{m,n}}{\Delta t} = k^{i}\left[\frac{T^{i}_{m+1,n} - 2T^{i}_{m,n} + T^{i}_{m-1,n}}{(\Delta x)^2} + \frac{T^{i}_{m,n+1} - 2T^{i}_{m,n} + T^{i}_{m,n-1}}{(\Delta y)^2}\right] + g^{i}_{m,n} \tag{3.18}$$

We can convert this equation into a form for calculating the temperature of a node at the next time step, $i + 1$, in terms of its present temperature, the present temperature of the surrounding nodes, and the properties of those nodes. One way of making this conversion simpler while obtaining a form that is easy to visualize is to combine the thermal conductivities and spatial distances into thermal resistive elements. The resistances are given by:

$$R_{m\pm 1} = \frac{\Delta x}{k_x w \Delta y} \tag{3.19}$$

$$R_{n\pm 1} = \frac{\Delta y}{k_y w \Delta x} \tag{3.20}$$

where w is the conductor width, $m \pm 1$ and $n \pm 1$ denote the resistance to longitudinally and azimuthally adjacent nodes respectively, k_x and k_y are the thermal conductivities in the longitudinal and azimuthal directions, respectively. Substituting Equations 3.19 and 3.20 into Equation 3.18 we obtain a simple power balance equation:

$$c^{i}_{m,n}\frac{T^{i+1}_{m,n} - T^{i}_{m,n}}{\Delta t} = \sum_{j} \frac{T^{i}_{j} - T^{i}_{m,n}}{R^{i}_{j}} \tag{3.21}$$

where j represents the nodal coordinate of the adjacent nodes, $(m \pm 1, n)$ and $(m, n \pm 1)$.

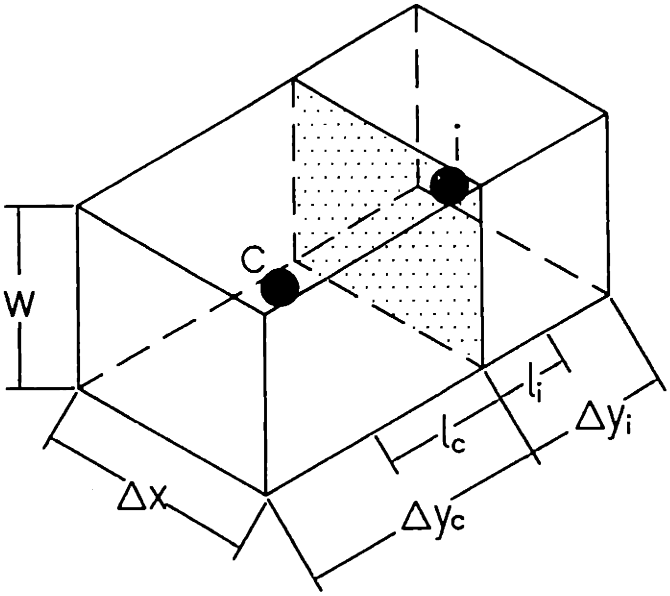

Figure 3-5: Junction of two nodes representing different materials

Solving for $T_{m,n}^{i+1}$ yields the desired form that can easily be incorporated into a numerical code:

$$T_{m,n}^{i+1} = \frac{\Delta t}{c_{m,n}^{i}}\left(g_{m,n}^{i} + \sum_{j} \frac{T_j^i - T_{m,n}^i}{R_j}\right) + T_{m,n}^{i} \tag{3.22}$$

3.3.6 Thermal Resistance Between Nodes

When two adjacent nodes represent different materials, or have significantly different temperatures, their thermal conductivities will be different. Additionally, nodes of different material will typically have different mesh size. Calculation of the thermal resistance between the two nodes, R_j, is performed simply by summing the resistance contribution of the individual nodes. Figure 3-5 depicts a junction between a conductor node and an insulation node. Calculation of the resistance between a node and the interface requires the thermal conductivity, length, and cross-sectional area. The resistance between the conductor node and the interface is given by:

$$R_c = \frac{l_c}{k_c A} = \frac{\Delta y_c}{2k_c w \Delta x} \tag{3.23}$$

while the contribution from the insulation node is given by:

$$R_i = \frac{l_i}{k_i A} = \frac{\Delta y_i}{2k_i w \Delta x} \tag{3.24}$$

where A is the cross-sectional area of the node, and the subscripts c and i denote conductor and insulation, respectively. The factor of 2 enters because l is one half the mesh size. Contact resistances are usually significant and must be added into the total thermal resistance. Summing Equations 3.23 and 3.24 while including a contact resistance, R_{ct}, yields:

$$R_j = \frac{1}{2w\Delta x}\left(\frac{\Delta y_c}{k_c} + \frac{\Delta y_i}{k_i}\right) + R_{ct} \tag{3.25}$$

3.3.7 Mesh Generation

The mesh depicted in Figure 3-3 is used in the simulation. Each layer of insulation and each layer of conductor are thin enough to require only one node across their thickness. Since this is a 2-D model, all nodes have the same depth.

The nodes have the following conditions associated with them, determined in the simulation as described:

- material: either BSCCO-2223, Kapton, or stainless steel, determined from the n coordinate.
- cross-sectional areas, longitudinal and azimuthal: depends on mesh size of the material and depth.
- position: determined from the nodal coordinate (m,n) as described in Figure 3-3.
- neighboring nodes: also determined from the nodal coordinate.
- temperature: only present value is necessary. When a node is passed, temperature is changed to the future value.
- thermal conductivity: function of temperature, material, and magnetic field for the conductor nodes.
- heat capacity: function of temperature and material.
- resistivity of conductor nodes: function of temperature and magnetic field.
- critical current of conductor nodes: function of temperature and magnetic field.

- voltage rise for conductor nodes: calculated from resistivity, critical current, operating current, and longitudinal mesh size using Equation 3.4.
- contact resistance between next layer $(n+1)$: determined from the n coordinate.

Additionally, magnetic field, B, transport current, I_t, and width, w are included in the simulation. I_t and w do not need to be assigned to each node because they do not vary. Magnetic field varies only slightly because we are interested in two conductor layers out of 18. Magnetic field has a small impact on material properties because we are operating in a small, self field.

We must choose sufficiently small time steps, Δt, and mesh sizes, Δx and Δy, for the simulation to converge. In determining their proper sizes, we begin with large mesh size and reduce Δt by factors of 2 until the result no longer varies with Δt. We repeat this process for smaller mesh sizes until the results are independent of both mesh size and time step. Finally, we increase Δx for nodes outside the heated region while proportionally decreasing there number. Mesh sizes used in the final simulation are 0.23 mm for Δy_c, 0.025 mm for Δy_i, and 0.0127 mm for the heater node thickness, Δy_h. Δx is set to 4.0 mm for all nodes. A total of 300 nodes per layer is required to maintain a negligible temperature rise at the far end from the heater.

The time step, Δt, is 500 μs. The time step requirement for convergence is related to mesh size by the following relationship:

$$\Delta t \leq min\left(\frac{C^i_{m,n}}{\sum_j 1/R^i_{m,n}}\right) \tag{3.26}$$

where $R^i_{m,n}$ is a function of thermal conductivity and mesh size. In some cases, Δt, can be increased or decreased during the simulation, as the value of Equation 3.26 changes, to improve the efficiency of the code. However, for this simulation, we want the nodes farthest from the heater to remain at T_o throughout the simulation. Therefore, Δt can not change throughout the simulation because the Δt calculated from Equation 3.26 is smallest at T_o.

3.3.8 Finite Difference Algorithm

Each node starts with the same initial temperature, T_o. For each time step, analysis begins at the (0,0) node (see Figure 3-3). Heat generation, g, is calculated with Equation 3.5 or 3.6. Heat flux to adjacent nodes is calculated using the right side of Equations 3.21. A new temperature is then assigned to the node using Equation 3.22. m is incremented to calculate the temperature of the next node in the same layer (next m, same n). When the end of the layer is reached, the next layer is begun at the top (m is set to 0, n is incremented). After the last node of the entire mesh, the process repeats for the next time step, starting at (0,0).

Fluxes into and properties of adjacent nodes whose temperatures have not been updated are stored in memory. This prevents repeated conductivity and flux calculations, and rids the requirement of having to remember both present and future temperatures. Before the simulation begins, properties are calculated for every multiple of 0.1 K between 20 K and 700 K and stored in memory. During the simulation, properties are determined from the stored values by interpolation. The program terminates when a maximum voltage, 0.5 V, for the outer conductor layer is reached, or when a maximum number of time steps has been executed.

The simulation is carried out using the C programming language. We found that 7200 nodes are required for convergence (24 layers, each 300 nodes in length). A simulation corresponding to 8 s real time required approximately 4 min. of running time on a Sun SPARCstation 5 workstation. The simulation code is listed in Appendix A.

3.4 Material Properties

Once we have a working simulation code, the accuracy of its results depends largely on the accuracy of the material properties as a function of temperature. It is not possible to know these functions exactly, as they are strongly dependent upon their processing. Additionally, previous attempts to tabulate thermophysical properties show limited accuracy, and reports vary. We present below mathematical correlations of the properties relevant to this experiment that have been successfully used in other attempts to model high-Tc normal

Table 3.1: Correlation coefficients for resistivity of silver in 0 field [3].

Temperature Range [K]	m_0 [$\mu\Omega$cm]	m_1 [$\mu\Omega$cm/K]	m_2 [$\mu\Omega$cm/K^2]	m_3 [$\mu\Omega$cm/K^3]
4–70	0.069136	-0.006714	0.00019844	-9.728×10^{-7}
70–300	-0.34145	0.0094905	-1.9905×10^{-5}	3.2803×10^{-8}
300–1000	1.6	0.005	0	0

zone propagation[3]. They include the thermal conductivities of stainless steel, Kapton insulation, and silver, as well as the electrical resistivity of silver. All are strong functions of temperature. For silver, magnetic field also effects resistivity and thermal conductivity.

3.4.1 Electrical Resistivity of Silver

Figure 3-6 shows the resistivity of silver as a function of temperature in zero background field, $\rho_{Ag,0}$[12]. The data has been correlated into a piecewise 3rd degree polynomial:

$$\rho_{Ag,0} = m_0 + m_1 T + m_2 T^2 + m_3 T^3 \tag{3.27}$$

where the coefficients, m_0, m_1, m_2, and m_3 are given in Table 3.1. It is important to note that $\rho_{Ag,0}$ increases by almost 2 orders of magnitude between 20 K and 100 K, as this is also the current sharing region for BSCCO-2223. Our ability to create a successful model will strongly depend on the accuracy of our $\rho_{Ag,0}$ correlation in this region.

3.4.2 Magnetoresistive Effect

The resistivity of silver has a strong dependence on magnetic field, known as the magnetoresistive effect. According to Kohler's rule:

$$\frac{\rho_{Ag}(B,T) - \rho_{Ag,0}(T)}{\rho_{Ag,0}(T)} = f\left[\frac{B}{\rho_{Ag,0}(T)}\right] \tag{3.28}$$

where $\rho_{Ag}(B,T)$ is the resistivity of silver in a magnetic field B, and at temperature T. Figure 3-7 is a Kohler plot for pure silver(RRR = 700)[12], showing the relationship between

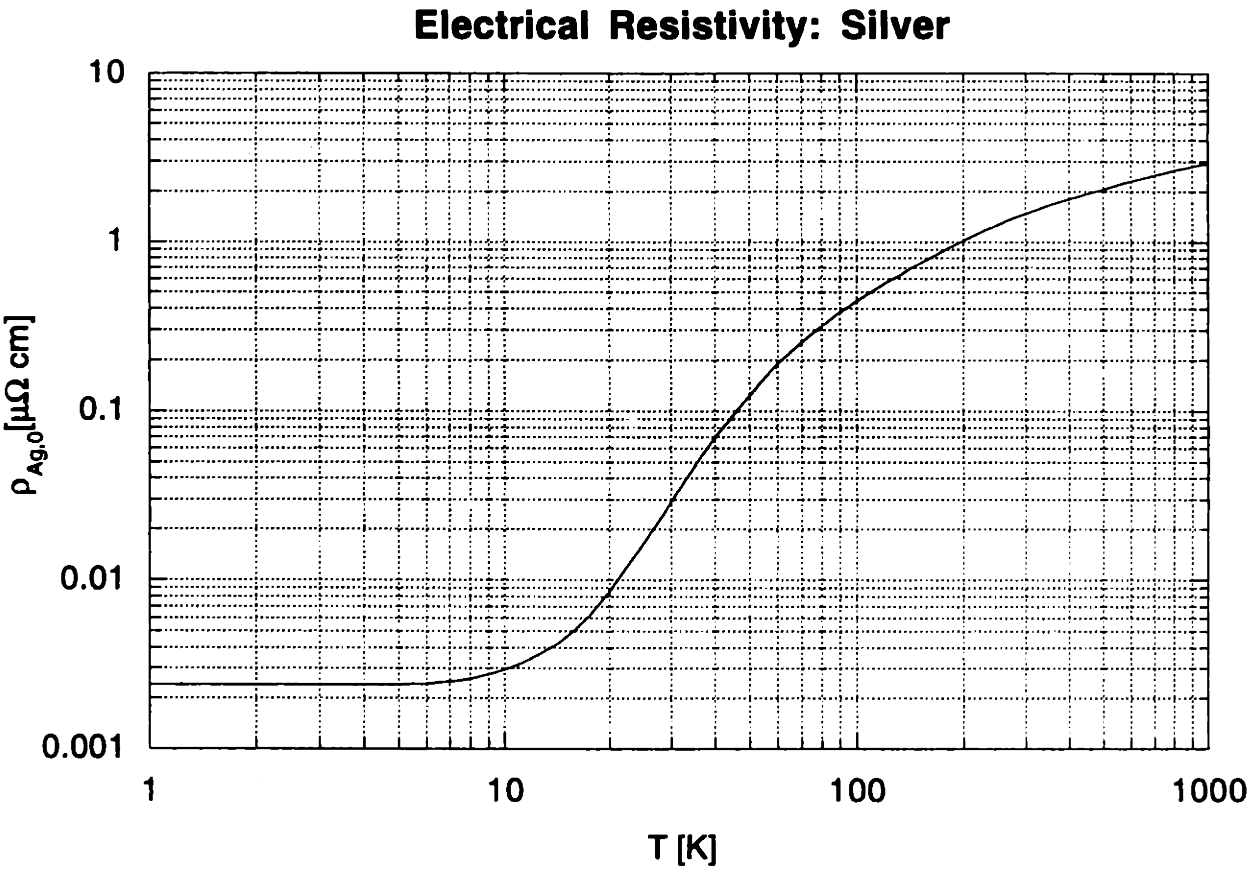

Figure 3-6: Electrical resistivity of silver in zero background field [3], [12].

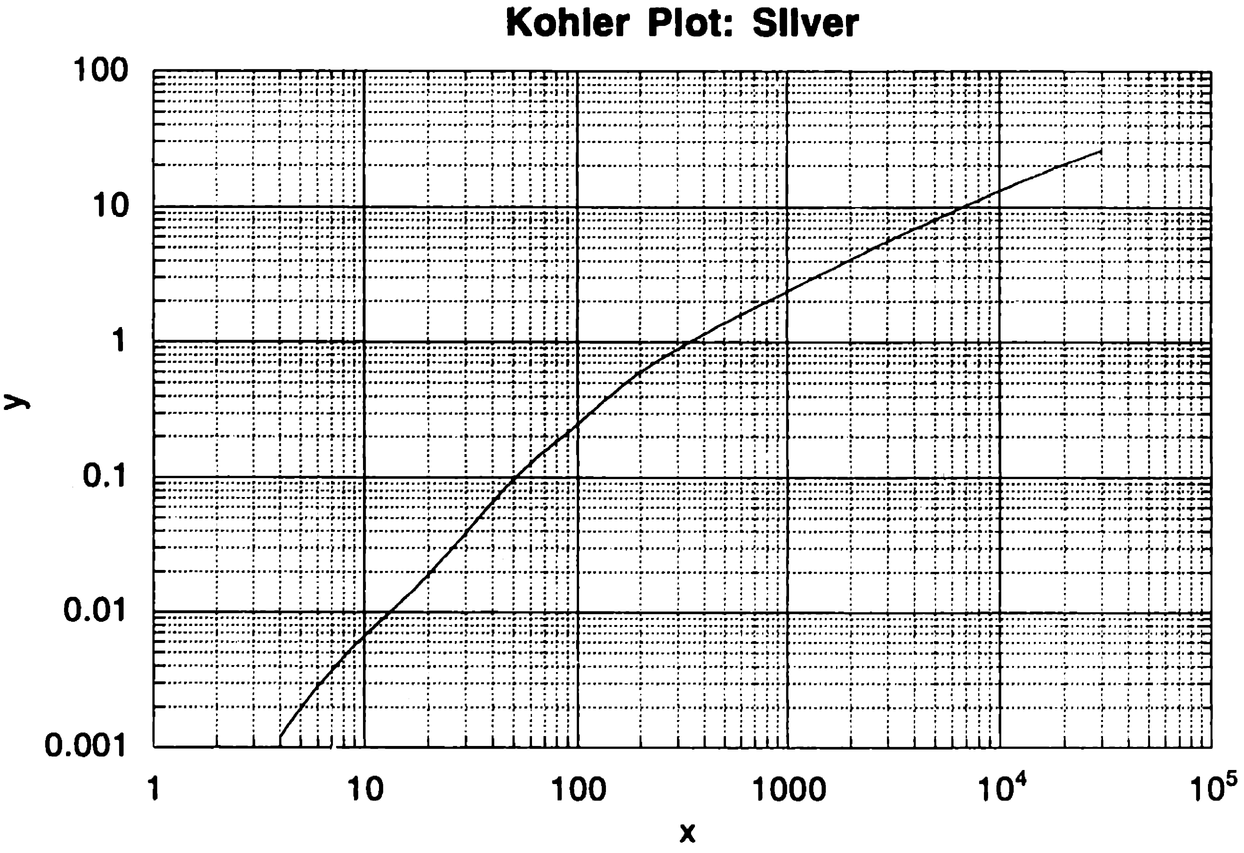

Figure 3-7: Kohler plot for silver(RRR = 700)[3], [12].

Table 3.2: Correlation coefficients of the Kohler function for silver[3].

x Range [T]	m_0	m_1
4–200	0.00014736	1.5838

a normalized change in resistivity due to magnetic field(the left-hand side of Equation 3.28), y, against the product of field and normalized zero field resistivity, x, given by:

$$x = B \times \frac{\rho_{Ag,0}(273\mathrm{K})}{\rho_{Ag,0}(T)} \tag{3.29}$$

The curve is piece-wise approximated by the following equation:

$$y = m_0 x^{m_1} \tag{3.30}$$

where the coefficients, m_0 and m_1, are listed in Table 3.2 for x less than 200. We do not expect x to be greater than 200 because the test magnet operates with zero background field.

3.4.3 Thermal Conductivity of Silver

Figure 3-8 shows the thermal conductivity of silver versus temperature in zero magnetic field, $k_{Ag,0}$. The data are taken from Bellis and Iwasa[12]. As is the case with resistivity, the thermal conductivity of silver varies by more than an order of magnitude in the temperature range 10-100 K. An exponential correlation that closely approximates the data is given by:

$$k_{Ag,0}(T) = 4.0 + 3.2T^2 e^{(4.0 - \frac{T}{4.5})} \tag{3.31}$$

for the temperature range 10 K to 300 K. In Equation 3.31, $k_{Ag,0}(T)$ is in the unit of W/cm K and T is in kelvin. Above 300 K, $k_{Ag,0}$ is roughly constant at 4.0 W/cm K as shown in Figure 3-8. The thermal conductivity of silver also varies strongly with magnetic field. The thermal conductivity in nonzero field, k_{Ag}, may be estimated using the Wiedmann-Franz

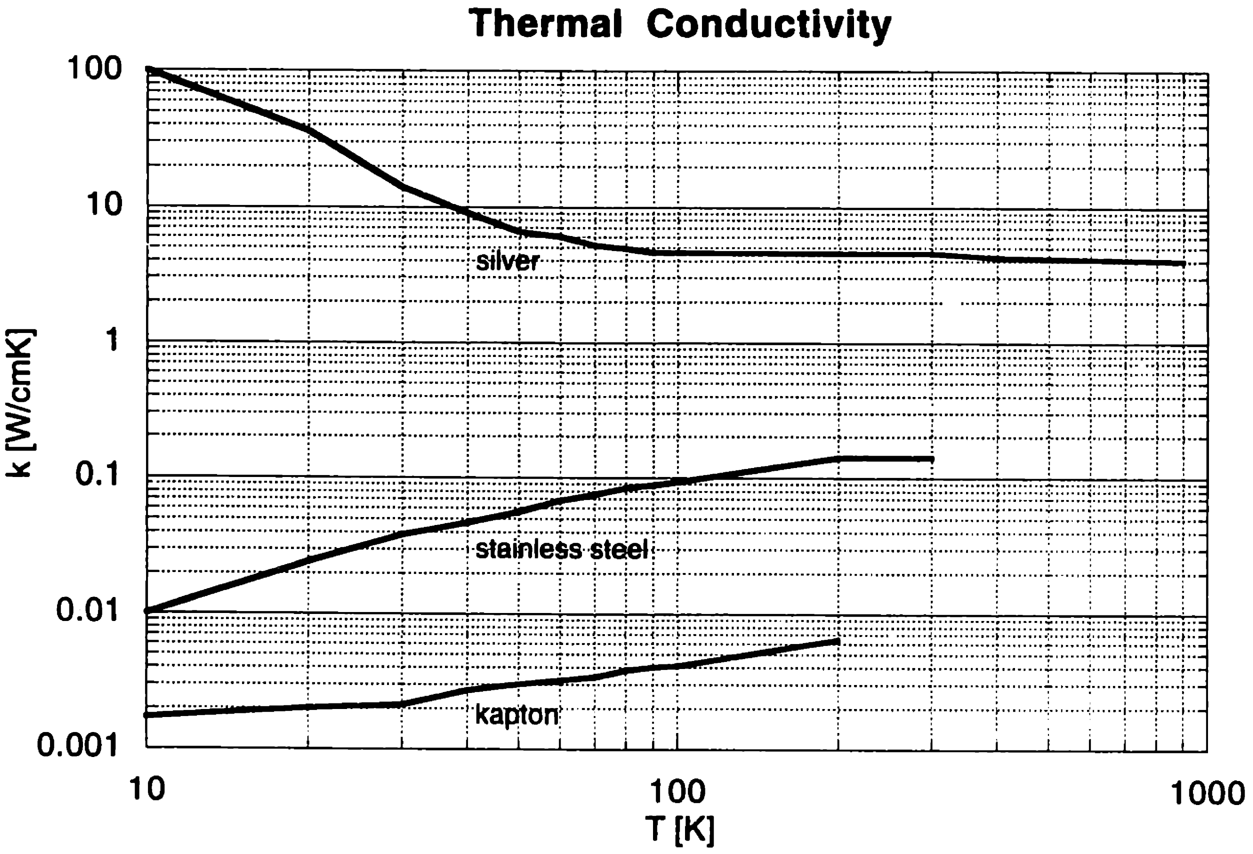

Figure 3-8: Thermal conductivity of silver, kapton, and stainless steel in zero background field.[3], [12], [13]

law, which applies to normal metals:

$$k_{Ag}(B,T)\rho_{Ag}(B,T) = \Lambda T \tag{3.32}$$

where Λ is the Lorentz number($2.45 \times 10^{-8} W/\Omega K^2$). Replacing ΛT with resistivity and thermal conductivity in zero field yields:

$$k_{Ag}(B,T)\rho_{Ag}(B,T) = k_{Ag,0}(T)\rho_{Ag,0}(T) \tag{3.33}$$

and

$$k_{Ag}(B,T) = k_{Ag,0}(T)\frac{\rho_{Ag,0}(T)}{\rho_{Ag}(B,T)} \tag{3.34}$$

However, the Lorentz number increases with magnetic field at a rate of approximately 0.05 per tesla. Therefore,

$$k_{Ag}(B,T) = (1 + 0.05B)k_{Ag,0}(T)\frac{\rho_{Ag,0}(T)}{\rho_{Ag}(B,T)} \tag{3.35}$$

This relation applies reasonably to most conductive metals.

3.4.4 Specific Heat of Silver

The specific heat of pure metals may be expressed with reasonable accuracy as the sum of an electronic(Sommerfield) contribution, c_{v1}, and a phonon (Debye) contribution, c_{v2}. The electronic contribution is a function of temperature given by:

$$c_{v1} = 1944\left(\frac{T}{\Theta}\right)^3 \tag{3.36}$$

where c_{v1} is given in J/mol K and Θ is the Debye temperature, equal to 220 K for silver[14]. The phonon contribution is a constant equal to the Dulong-Petit limit. This limit is approached above the Debye temperature and is given by:

$$c_{v2} = 3R = 24.95 \tag{3.37}$$

where c_{v2} is given in J/molK and R is the universal gas constant. According to Dresner[14], the two may be combined into a single equation, yielding a close approximation:

$$c_v = (c_{v1}^{-n} + c_{v2}^{-n})^{-1/n} \tag{3.38}$$

where n = 0.85, $c_{v1} = 17.75\times10^{-6}T^3$ J/cm^{3}K, and $c_{v2} = 2.426$ J/cm^{3}K for silver. Magnetic field has minimal effect on the specific heat of silver, c_{Ag}. Therefore, we use the following function to calculate c_{Ag} in the simulation:

$$c_{Ag} = \left[(17.75\times10^{-6}T^3)^{-0.85} + (2.426)^{-0.85}\right]^{-1/0.85} \tag{3.39}$$

3.4.5 Properties of BSCCO-2223

Thermal Conductivity There are few references that list the thermophysical properties of BSCCO-2223. The thermal conductivities of undoped and silver doped BSCCO-2212, reported by Matsokawa et. al.[15], are on the order of 0.001 W/cmK. By comparison to Figure 3-8, we see that the thermal conductivity of silver is at least 2 orders of magnitude larger than the thermal conductivity of BSCCO-2212. Therefore, we estimate the thermal conductivity of the conductor, k_{cd}, as the volumetric fraction of silver, x_{Ag}, multiplied by the thermal conductivity of silver. This is a legitimate approximation because the two components conduct heat in parallel.

Specific Heat Specific heat data for BSCCO-2223 is just as sparse as the thermal conductivity data. Thermal properties given by Iwasa[6] for BSCCO-2223 and silver at 120 K show that the volumetric specific heat of BSCCO-2223 is about half c_{Ag}. For a silver fraction $x_{Ag} = 0.70$, we estimate the volumetric specific heat of the conductor, c_{cd}, as $0.85c_{Ag}$.

Critical Current The conductor critical current, I_c, is not correlated as a function of temperature prior to winding the coil. Ideally, we would measure I_c at various sections in the region we intend to model. The best way is to produce voltage versus transport current traces for each of these sections. Unfortunately, the heat dissipation in the long length of conductor exceeds the refrigeration capacity before the critical current is reached and the temperature rises quickly. Therefore, I_c is calculated by a linear approximation based on manufacturer specifications.

The electric field, E, in a superconducting composite is related to transport current by the following function:

$$E = E_c\left(\frac{I_t}{I_c}\right)^n \tag{3.40}$$

where E_c is the electric field that defines the critical current(typically 1 μV/cm), and n is the index number. Sumitomo measured currents that produce electric fields of 0.1 and 1.0 μV/cm at 77 K to be 19.9 A and 23.7 A, respectively. I_c vs. T data found in [6] indicates the relation is approximately linear with a slope of -1.82 A/K, and (T-intercept) of 90 K. Using the data supplied by Sumitomo, I_c is determined as a function of T for $E_c = 1$ μV/cm.:

$$I_c = -1.82T + 163.8 \tag{3.41}$$

By setting I_c equal to zero, we estimate a T_c to be 89.3 K.

The dissipation due to an electric field of 1 μV/cm is insignificant for the short trial durations. The simulation uses a relationship based on $E_c = 22$ μV/cm, $n = 8$, and a T_c of 89.5 K:

$$I_c = -3.12T + 279.2 \tag{3.42}$$

3.4.6 Thermophysical Properties of Stainless Steel and Kapton

The volumetric specific heats and thermal conductivities of Kapton and stainless steel 310 are shown with silver in Figures 3-8[12],[13] and 3-9[6],[13],[16]. These plots are accurate to within 1%. Property data are not actually available for Kapton, but the thermal properties of organic materials do not vary significantly. Here, we use data for epoxy. Variations in the thermophysical properties due to magnetic field are negligible for stainless steel and organic materials.

The data are correlated by a piece-wise third-degree polynomial as is done for the zero field resistivity of silver (see Equation 3.27). The correlation coefficients are given in Table 3.4

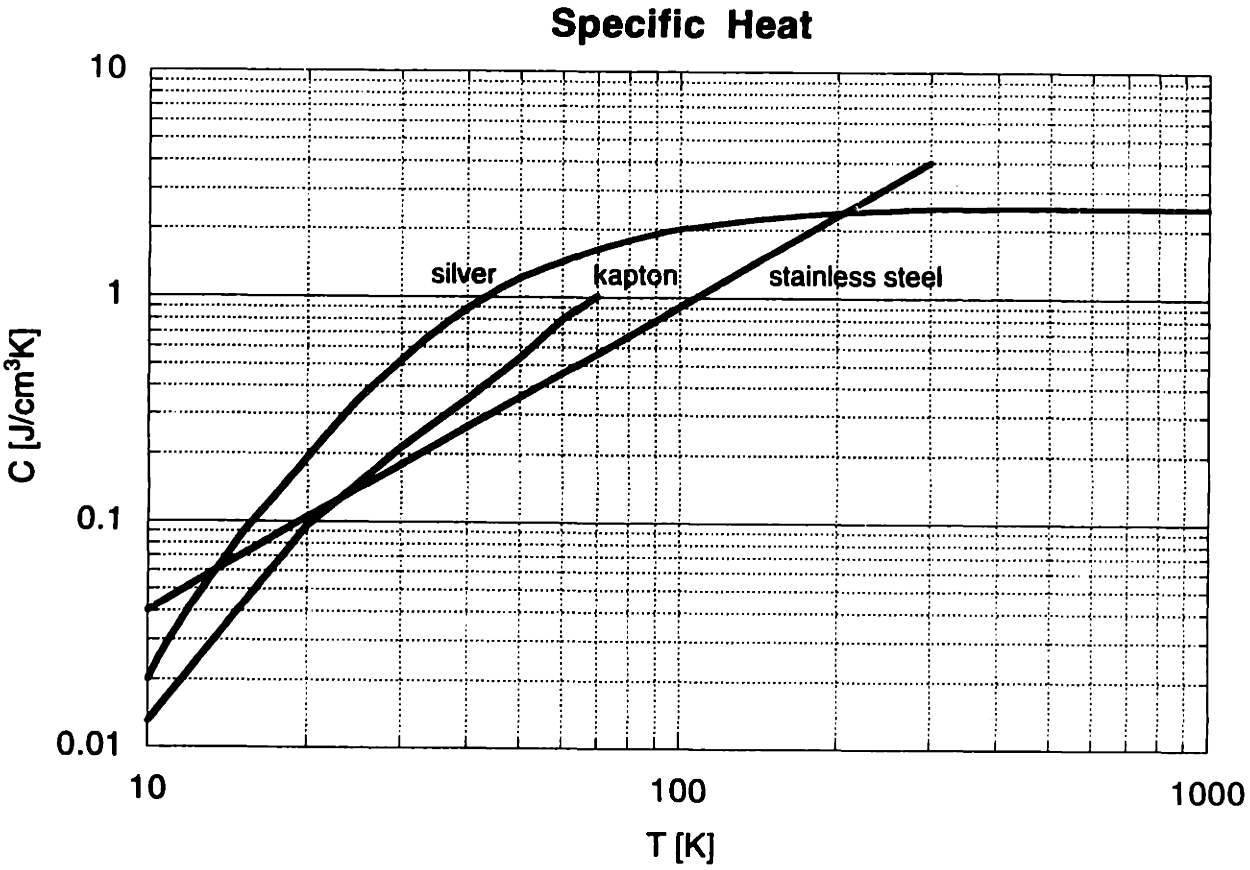

Figure 3-9: Specific heats of silver, kapton, and stainless steel.[3],[6],[13],[16]

Table 3.3: Correlation coefficients for the thermophysical properties of stainless steel and kapton[3].

Property	Temperature Range [K]	m_0 [$\mu\Omega$cm]	m_1 [$\mu\Omega$cm/K]	m_2 [$\mu\Omega$cm/K^2]	m_3 [$\mu\Omega$cm/K^3]
k_{ss}	20–300	-0.001877	0.001260	-3.3219×10^{-6}	2.7041×10^{-9}
k_k	20–300	0.0015335	0.0000227	0	0
c_{ss}	20–300	-0.014096	0.005665	2.4600×10^{-5}	0
c_k	20–300	-0.016000	0.002074	1.7738×10^{-4}	0

for the range of 20 K to 300 K. Above 300 K, the properties are assumed constant. The subscripts, k and ss, are used to denote kapton and stainless steel, respectively.

3.5 Power Dissipation Functions

3.5.1 Heat Dissipation in the Conductor

Equations 3.5 and 3.6 determine the power dissipation density, g, in the conductor as a function of temperature. Substituting the appropriate variables yields the following piecewise function:

$$g(T) = \begin{cases} I_t(I_t - I_c)\dfrac{\rho_{Ag}}{x_{Ag}A_{cd}} & \text{if } T < T_c \\ I_t^2\dfrac{\rho_{Ag}}{x_{Ag}A_{cd}} & \text{if } T \geq T_c \end{cases} \tag{3.43}$$

Dissipation in the current sharing region, $T < T_c$, is calculated by substitution of Equation 3.42 for I_c.

3.5.2 Heat Dissipation in the Heater

The heater pulse deviated slightly between trials. The heater pulse trace obtained during the experiment is applied to the heater dissipation, q_{ht}, for the corresponding simulation. The voltage trace is easily converted to power dissipation using Ohm's Law and the heater resistance, R_{ht}:

$$q_{ht}^i = \frac{(V^i)^2}{R_{ht}} \tag{3.44}$$

where i denotes the time step. R_{ht} is measured to be 5.6 Ω at 20K. From the simulation, we see the maximum heater temperature is approximately 130K. If we assume the average temperature of the heater to be approximately 77 K, data found in Iwasa[6] allows us to convert the resistance at 20 K to a value corresponding to 77 K of 5.9 Ω.

Chapter 4

Discussion of Results

4.1 Qualitative Aspects of the Experimental Results

Figure 4-1 is a voltage trace obtained for a propagating quench (trial 4). The heater pulse is initiated at t = 0 s. The conductor temperature within the heated length surpasses the current sharing temperature when a measurable voltage rise is observed, at approximately 0.5 s. The voltage rises somewhat sharply at first, then levels off as the heater and heated region approach thermal equilibrium. At this point, Joule dissipation in the heated region, caused by the transport current flowing through the resistive matrix, is larger than heat conduction away from the heated region. Therefore, the voltage (and temperature) continue to rise. The rate of rise increases as the critical current of the conductor decreases and more current flows through the matrix. The increasing matrix resistivity also contributes to the increasing voltage rise rate. Once the critical current is surpassed, change in voltage becomes completely dependent on the changing resistivity. Conduction along the tape causes the normal region to grow. The normal region passes the voltage taps at the ends of the heater at approximately 7.5 s; when a sharp rise is observed in region 7(see Figure 2-5), just outside the heated region. Difference in the time the normal region passes the upper and lower ends of the heater is probably due to a subtle nonuniformity in the power balance along the conductor.

Figure 4-2 is a voltage trace obtained for a quench recovery(trial 1) with the same trans-

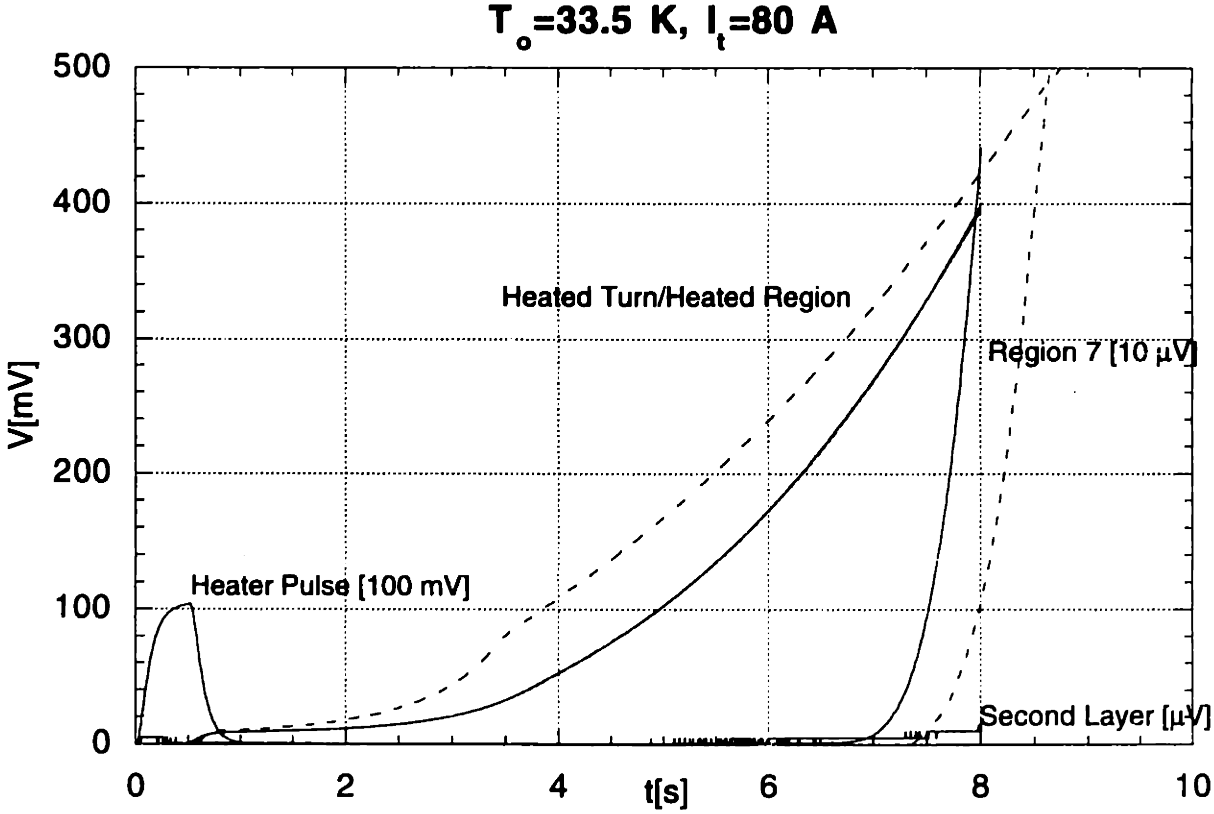

Figure 4-1: Experimental(solid) and simulated(dashed) voltage traces (trial 4). Region 7 refers to the small conductor length just outside the heated region, depicted in Figure 2-5(pg.17).

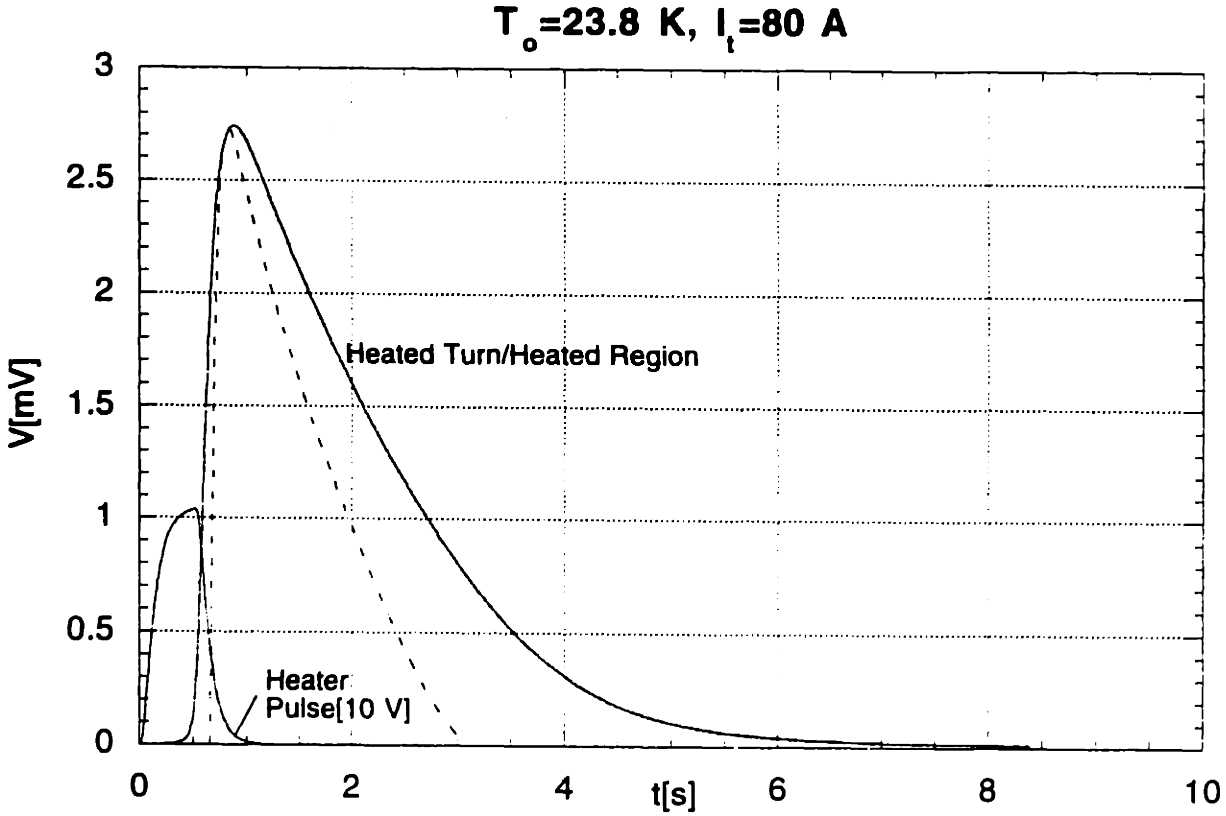

Figure 4-2: Experimental(solid) and simulated(dashed) voltage traces (trial 1).

port current as the trial just discussed. Voltage rise in the heated region is first observed at approximately 0.5 s, very similar to the propagation example. We expect these times to be close because, although the magnet is operated 10 K lower for this trial, the enthalpy difference between 23 K and 33 K is small compared with the enthalpy difference between 33 K and the current sharing temperature, estimated to be around 65 K, as can be inferred from Figure 3-9. If only a small portion of the heater energy is used to quickly bring the conductor temperature to 33 K, then the thermal interaction between the heater and the conductor should be very similar in both trials as long as the conditions at the interface of the heater and the conductor are consistent. However, the small enthalpy difference between 23 K and 33 K becomes very significant after the heater and the conductor reach thermal equilibrium at some temperature, T_{eq}. In the previous example, T_{eq} was just large enough for the Joule dissipation to exceed cooling of the heated region by conduction. In this recovery example, T_{eq} is not quite high enough for Joule dissipation to exceed conduction cooling, and the temperature and voltage drops after the equilibrium is reached.

For the 80-A trials shown in Figure 4-1 and Figure 4-2, 9.5 J is dissipated in the quench heater in approximately 0.5 s for both cases. It is apparent that stability improves with decreasing operating temperature as the same heat input that leads to a voltage recovery at 23.8 K causes a propagating quench at 33.5 K. Figure 4-3 makes the same comparison for a transport current of 60 A, showing the same difference in response with $T_o = 33.5$ K (trial 3) and $T_o = 50.0$ K (trial 6). Reduction in stability due to increasing I_t with similar T_o is illustrated in Figure 4-4 for $T_o \approx 50$ K with a recovery at 50 A (trial 5) and a propagating quench at 60 A (trial 6), and in Figure 4-5 for $T_o \approx 24$ K with a recovery at 80 A (trial 1) and a propagating quench at 100 A (trial 2).

4.2 Numerical Results

The trials are simulated using identical parameters except for operating current and temperature. Also, the heater pulse trace sampled during the experiment is applied to the corresponding simulation. Contact resistances and the critical current dependence on temperature are chosen to make the best match between the simulation and the entire set of

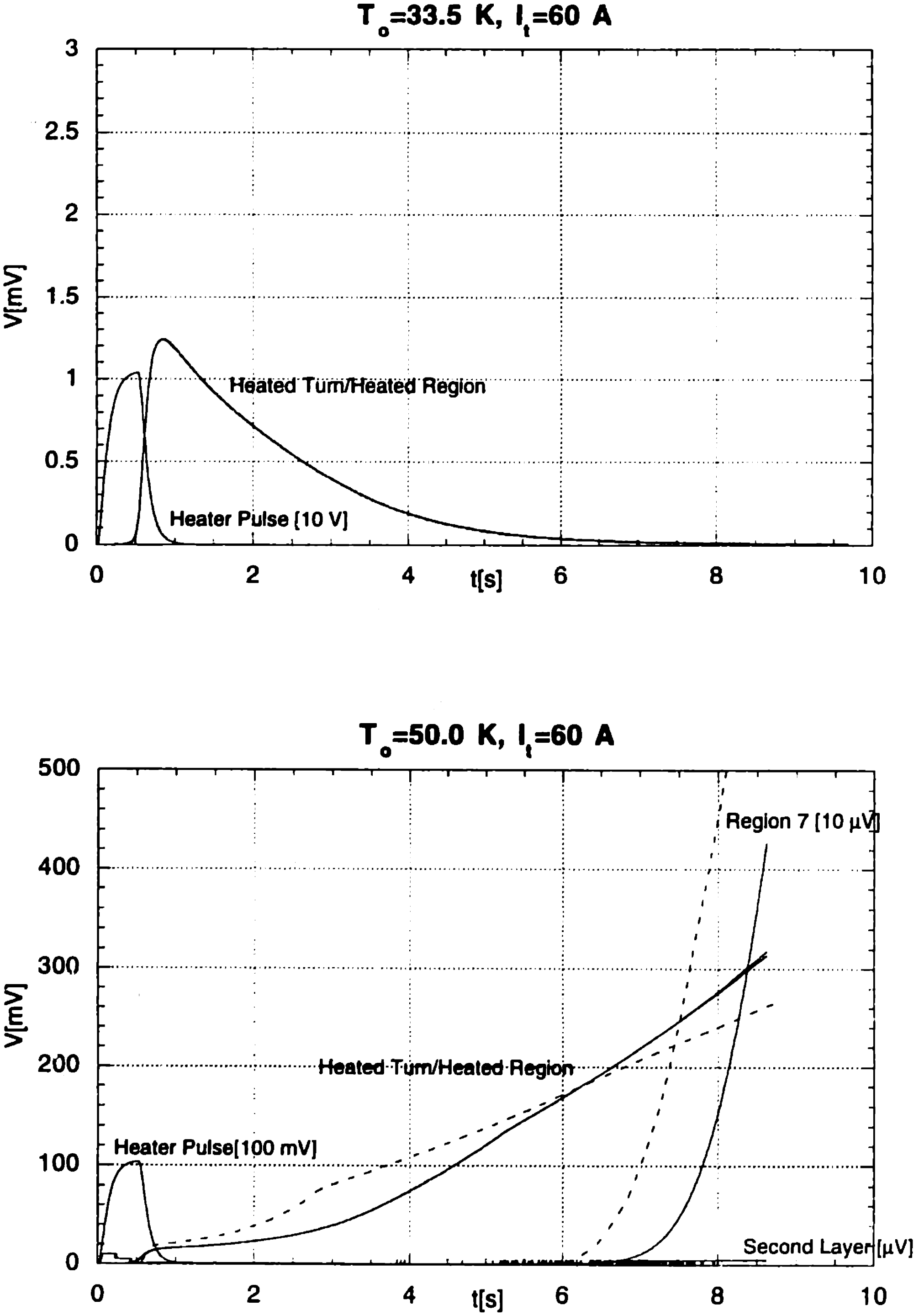

Figure 4-3: Experimental voltage traces for I_t = 60 A showing a recovery at 33.5 K (trial 3) and a quench at 50.0 K (trial 6). The dashed curves shown for the 50.0 K trial are the simulated traces.

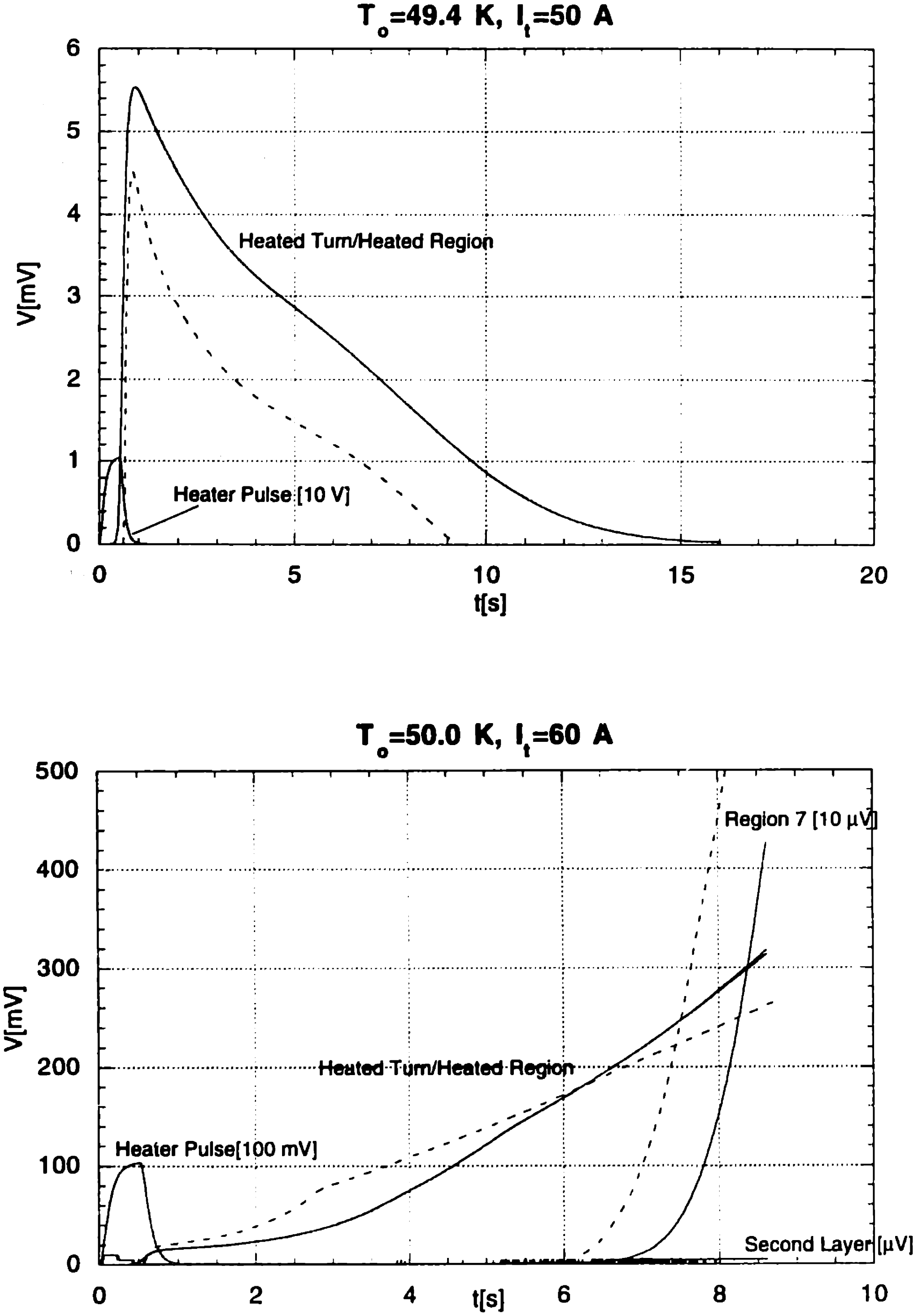

Figure 4-4: Experimental(solid) and simulated(dashed) voltage traces for $T_o \approx 50$ K showing a recovery at 50 A (trial 5) and a quench at 60 A (trial 6).

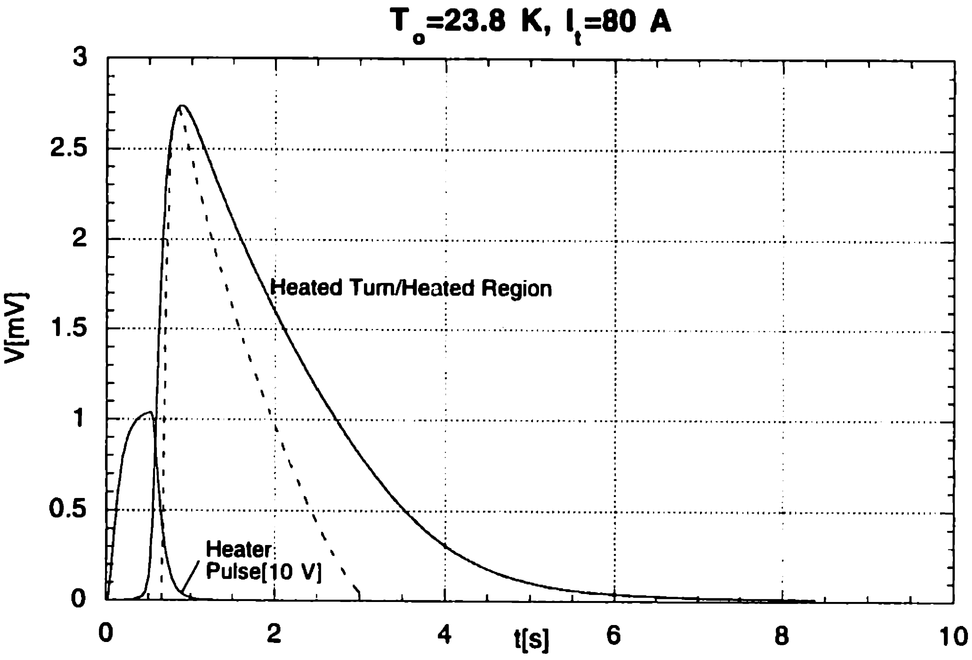

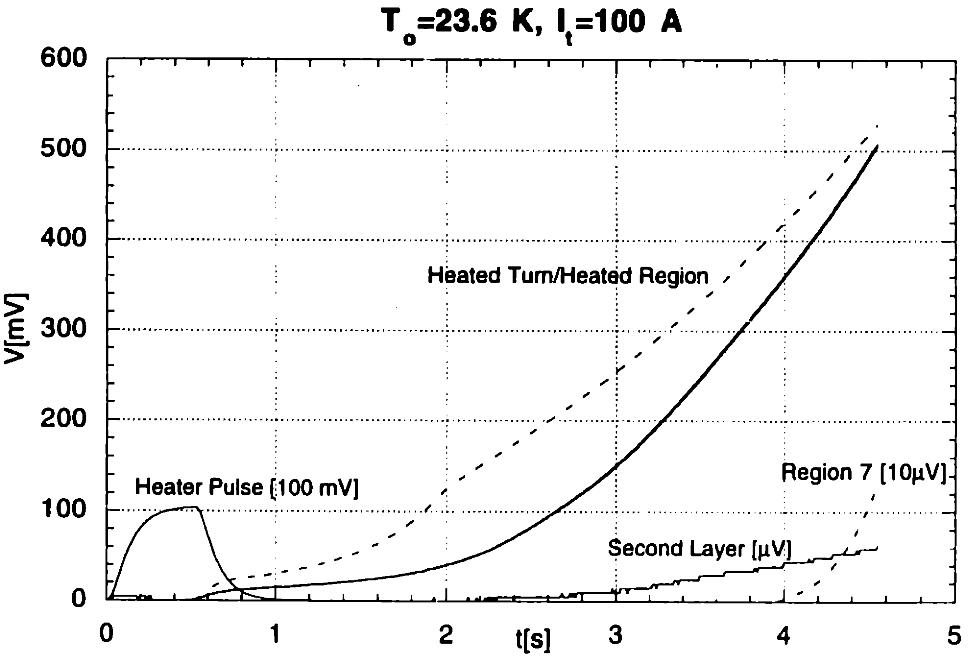

Figure 4-5: Experimental(solid) and simulated(dashed) voltage traces for $T_o \approx 24$ K showing a recovery at 80 A (trial 1) and a quench at 100 A (trial 2).

experimental traces. Between the heater and the conductor, a thermal resistance of 10 cm^2K/W is assigned to each surface of the Kapton insulation. At all other radially normal surfaces, a thermal resistance of 320 $cm^2\,K/W$ is assigned. The thermal grease applied to the surfaces between the heater and the conductor, depicted in Figure 2-4, accounts for the smaller thermal resistance.

The critical current function is a line connecting 216.8 A at 20.0 K, and 0 A at 89.5 K. Critical currents calculated using this function are larger than those based on an electric field criterion of 1 μV/cm. Heat dissipation caused by a voltage rise of 1μV/cm is very small, at least in terms of the time duration of the trials made. At 77 K, the critical current calculated with the simulation function corresponds to an electric field of 22 μV/cm, according to the data given in Section 3.4.5, and Equation 3.40 with an index number, n, of 8.

Figure 4-1 includes the simulated voltage traces for trial 4. The model closely predicts the times at which a positive voltage is initially observed inside and outside of the heated region. Additionally, the voltage rise in the heated region while the heater is in thermal equilibrium with the conductor, between 0.6 s and 1.5 s, is also closely matched. However, after 1.5 s, the simulated voltage trace deviates significantly from the actual because critical current is approximated as a linear function of temperature, being zero at 89.5 K. In reality, the critical temperature of BSCCO-2223 extends to 110 K. The critical current drops less sharply at higher temperatures and reaches zero gradually, as may be inferred from Figure 1-1. Thus, in the simulation, as the conductor temperature goes above 85 K the voltage rise is overestimated. Also, the simulated critical current is a piecewise function of temperature, with a discontinuity in the slope at the critical temperature. In the simulated results there is an abrupt change of slope as the temperature of the heated region crosses the critical temperature, at approximately 3.3 s and 80 mV. Above this voltage, the rate of rise for the simulated and experimental traces agree reasonably well.

Figure 4-2 includes the simulated voltage traces for trial 2, a recovery. Again, both the time at which a positive voltage is initially observed and the voltage when the heater and conductor are in thermal equilibrium are closely matched. However, the simulated voltage trace drops off much more quickly than the experimental. Voltage is calculated using Equation 3.4, where it is proportional to the difference in transport current and critical current. If the transport current is less than or equal to critical current, the voltage is assumed zero:

$$\frac{\partial V}{\partial x} = \begin{cases} 0 & \text{if } I_t \leq I_c \\ (I_t - I_c)\dfrac{\rho_{Ag}}{x_{Ag}A_{cd}} & \text{if } I_t > I_c \end{cases} \tag{4.1}$$

When the conductor temperature drops just below the temperature that matches critical and transport current, the voltage rise is calculated as zero. Realistically, rhe electric field in the conductor is a smooth, not piecewise, function of transport current. When the conductor is close to this temperature, a significant rise should still be observed, accounting for the slower voltage drop-off rate in the experimental voltage traces. This also explains the discrepancy in the voltage rise of the second layer for trial 1 (Figure 4-5). Experimental traces show a rise of approximately 60 μV. The rise indicates that the current sharing temperature is approached, but the temperature rise is too small to be accurately predicted by the piecewise function. Additionally, in trial 3 (Figure 4-3), the simulation predicts no voltage rise while the experimental traces show a small rise of approximately 1.3 mV.

4.3 Simulation Limitations

The model assumes the conductor layers to be aligned, but they are actually arranged as criss-crossing helixes. Throughout most of the coil, the conductor bridges two adjacent turns in the next layer. As described in Section 3.3.3, a coefficient is used to adjust the conduction between adjacent layers so that conduction into the warmer turn of the next layer is more realistic, while heat conduction into the cooler turn, is simply unaccounted for. Towards the end of the heated region, the portion of layer-to-layer conduction that is thrown out is largest. Simulation reveals that past the middle of the heated region(which corresponds to one quarter of the actual heated region), temperature rise is small in the second layer, less than 3.3 K, prior to the heated turn reaching the critical temperature. Thus, discrepancy in calculating heat conduction out of the heated region is small. However, in certain situations temperature rise in the second layer may be significant. For example, a particular quench event may last a relatively long time, on the order of minutes, or the thermal resistances between layers may be very small. In such cases, the method described in Section 3.3.3

would not be valid. The three-dimensional helix geometry would have to be fully accounted for, leading to a more complicated model with significantly longer simulation times.

The linear approximation used for the critical current temperature dependency may not suffice in modeling situations where voltage rise or local heat dissipation is of critical importance. Unfortunately, a very accurate relationship between electric field, current, and temperature are presently unavailable.

4.4 Model Variations

When calculating the simulated layer-to-layer heat conduction as described in Section 3.3.3, it is assumed that the middle of the quench heater is aligned symmetrically with the crossing of the turns of the outer two layers. An alternate relationship was tried that shifted the middle of the heater one quarter turn relative to the wind:

$$A_{sh} = A_{nd}\left(1 - \left|\frac{1}{2} - \frac{m}{M_{trn}}\right|\right) \tag{4.2}$$

This function has a value of 1/2 at the middle of the heater, indicating that the heat conduction from the middle of the turn is shared by two turns. At one quarter of a turn from the heater middle the turns coincide and Equation 4.2 has a value of one. At the end of the turn, it is equal to one half. The adjustment causes visible differences, but are insignificant compared to the overall discrepancy between experimental and simulated results. The adjustment may become necessary in situations where the contact resistances at the insulation surfaces are smaller.

The ends of the heater are assumed as adiabatic. Simulations were executed with the heater ends modeled as isothermal where they remain at T_o throughout the trial, producing a very slight difference. The heater conducts heat slowly, even under large temperature gradients because it is very thin and the thermal conductivity of the heater material, stainless steel, is low. We can estimate a maximum possible heat conduction through the ends by analyzing the node at the heater end. Conduction out of the node through the end, q_{end}, is given by:

$$q_{end} = \frac{\tilde{k}A_{ht}}{\Delta x}(T_{end} - T_{out})t_{pls} \tag{4.3}$$

where T_{end} is the temperature of the end node, T_{out} is the temperature just outside the heater end, t_{pls} is the heater pulse duration, Δx is the longitudinal mesh size, A_{ht} is the cross-sectional area of the heater, and $\tilde{k}$ is the average thermal conductivity of the heater material between T_{end} and T_{out}. The maximum possible q_{end} for any given trial is estimated by assuming T_{out} is equal to the operating temperature, and T_{end} is set equal to the maximum temperature observed in the heater during the simulation. T_{end} is approximately 113 K, while T_{out} is set to the lowest operating temperature used, about 20 K. Using actual values for the other variables yields a value of 5 mJ, negligible compared with the total heater pulse energy of approximately 9.5 J.

4.5 Estimation of Quench Propagation Temperature

As discussed in Section 4.1, propagation of a normal zone results when the conductor reaches a high enough temperature for Joule dissipation to exceed conductive cooling, T_{qp}. An equation for estimating T_{qp} is derived here.

Figure 4-6 shows simulated temperature profiles along one half of the heated conductor for trial 4 at various times after the initiation of the heater pulse. Before Joule dissipation begins to dramatically increase the temperature and voltage rise, the temperature profiles well inside the heated region are almost flat. Therefore, at the center of the heated region where the conductor temperature is the highest, we expect heat conduction along the tape to be small compared with layer-to-layer conduction. To justify this claim, we calculate heat conduction along the conductor from the node corresponding to the middle of the heated region, q_l, at 1.0 s using the simulated temperature profiles. The following equation applies:

$$q_l = \frac{kA}{l}\frac{\partial T}{\partial x} \approx \frac{kA_{cd}}{\Delta x}(T_0 - T_1) \tag{4.4}$$

where k is the thermal conductivity of the conductor, Δx is the mesh size in the longitudinal direction(along the conductor), A_{cd} is the conductor cross-sectional area, and T_0 and T_1 are

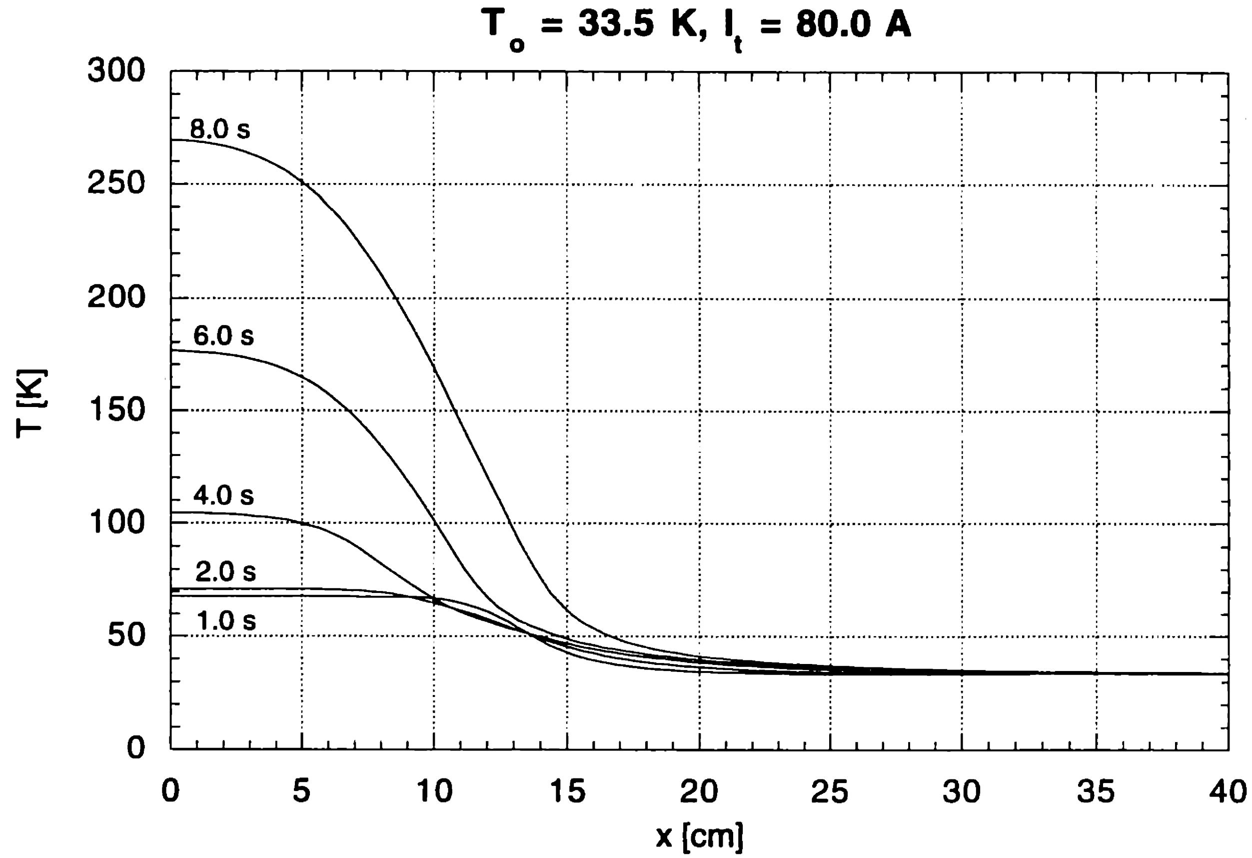

Figure 4-6: Simulated temperature profiles for trial 4 (see Figure 4-1).

the temperatures of the first and second nodes from the midpoint of the heated region in the longitudinal direction. Using a value for k corresponding to the simulated conductor temperature yields a value for q_l of 8.3 μW.

Layer-to-layer heat conduction per unit length, q_r', is given by:

$$q_r' = \frac{W}{\sum R_{th}}(T_2 - T_{hr}) \tag{4.5}$$

where T_2 and T_{hr} are the temperatures of the second layer and the heated region, respectively, and $\sum R_{th}$ are the thermal resistances given by:

$$\sum R_{th} = 4R_{ct} + 3\frac{\delta_{ins}}{k_{ins}} \tag{4.6}$$

R_{ct} is the contact resistance, δ_{ins} is the insulation thickness, and k_{ins} is the thermal conductivity of the insulation. The factors of 4 and 3 appear because there are 4 interfaces and 3 layers of insulation between each conductor layer. We may estimate layer-to-layer conduction by first assuming that the second layer temperature has not yet increased significantly from its initial temperature, T_o. At 1.0 s, the simulation calculates a temperature rise in the second layer of less than 1.5 K. For k_{ins}, we use an average value of $\tilde{k}_{ins} = 2.0$ mW/cmK as the thermal conductivity of organic materials does not change very much with temperature. The value for R_{ct} used in the simulation is 320 $\mathrm{cm^2K/W}$. Setting T_2 equal to T_o and assigning T_{hr} its simulated value yields a value for q'_r. Multiplication by Δx indicates a heat conduction from the node at the middle of the heated region equal to 3.8 mW, which is over 2 orders of magnitude larger than conduction along the conductor.

Having verified that layer-to-layer conduction is substantially larger than conduction along the conductor, we can derive an equation to estimate the minimum conductor temperature that will lead to a quench propagation by equating Joule dissipation with layer-to-layer conduction. Joule dissipation per unit length is given by Equation 3.5:

$$g(T,x) = I_t(I_t - I_c)\frac{\rho_m}{x_m A_{cd}} \tag{4.7}$$

Setting the right-hand-sides of Equations 4.5 and 4.7 equal and rearranging, we have:

$$T_{qp} = \frac{\rho_m I_t(I_t - I_c)}{x_m A_{cd} W}\left(4R_{ct} + 3\frac{\delta_{ins}}{k - ins}\right) \tag{4.8}$$

When solving for T_{qp}, we may have to iterate using different values for ρ and I_t because their values change dramatically in the temperature range 20–100 K. Once we have estimated a value for T_{qp}, energy dissipation per unit length necessary to propagate a quench may be estimated from the enthalpy change in the conductor between T_o and T_{qp}. It is interesting to note that reducing the contact resistances increases the energy dissipation density required to cause a quench. However, this equation fails to apply when the contact resistance is so low that the second layer temperature rises closely behind the temperature of the heated region.

Chapter 5

Application: Maximum Temperature During a Quench Event in an HTS Magnet

During a quench in an HTS magnet, the energy that raises the conductor temperature through Joule dissipation originates from the magnetic energy that is stored prior to the quench. Therefore, by conservation of energy we expect the conductor will reach some maximum temperature that depends strongly on the initial stored energy(a function of operating current and inductance) as well as conductor attributes, wind geometry, operating temperature, and how the quench is initiated. If the maximum temperature is low enough not to damage the conductor, the magnet may not require any protection. Using a simulation that is tailored according to the design parameters, we can predict the maximum temperature attained during a quench as a function of operating current and inductance, and to a lesser degree operating temperature.

Because there are many possible operating conditions, magnet designs, and initial size of the normal zone, we cannot determine a relationship between maximum temperature and initial stored energy that applies to all situations. However, results from a simulation that is set up for a very specific design may still reveal trends that will be important to understand when considering designs for future magnets. In the following section, we modify the numerical code to simulate a reasonably applicable design in producing a maximum temperature versus stored energy relationship at various operating currents and operating temperatures.

5.1 Simulation for Modeling Magnets of Various Inductances

5.1.1 Calculation of Transport Current

In Chapter 3, we developed a simulation code that models constant transport current operation. For the magnet under consideration, persistent or driven with a voltage-mode power supply, the transport current will decrease at a rate determined by the magnet inductance and the voltage rise. Figure 5-1 is a simple circuit schematic representing the magnet circuit after the quench has been initiated. The inductance, L, has a value equal to the magnet inductance, which is constant. The resistance component, $R(t)$, varies over time and is dependent upon the temperature profile within the winding as well as the winding parameters. Using Kirchoff's Law, we obtain the following relationship for the transport current, $I_t(t)$:

$$I_t(t)R(t) + L\frac{dI_t(t)}{dt} = 0. \tag{5.1}$$

$R(t)$ may be obtained indirectly from the voltage across the normal region in the coil, $V(t)$, which is calculated by the simulation using the method described in Chapter 3. $R(t)$ relates to $V(t)$ and $I_t(t)$ simply as:

$$R(t) = \frac{V(t)}{I_t(t)} \tag{5.2}$$

Substitution of Equation 5.2 into Equation 5.1 with some rearrangement of the variables yields:

$$\frac{dI_t(t)}{dt} = -\frac{V(t)}{L} \tag{5.3}$$

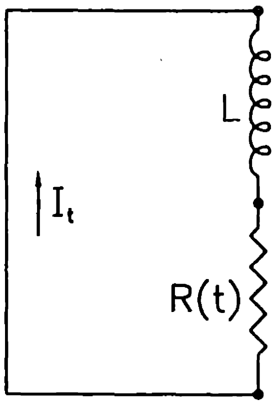

Figure 5-1: Circuit schematic modeling a quench event in a magnet, persistent or driven by a voltage-mode supply.

Equation 5.3 is easily converted into a numerically usable form by substituting in the appropriate Taylor expansion, Equation 3.15 with $T_{m,n}$ replaced by I_t, which gives us:

$$\frac{I_t^{i+1} - I_t^i}{\Delta t} = -\frac{V^i}{L} \tag{5.4}$$

where i denotes the time step number. The transport current for the next time step, I_t^{i+1}, is solved for explicitly by rearranging Equation 5.4:

$$I_t^{i+1} = I_t^i - \frac{V^i}{L}\Delta t \tag{5.5}$$

In the simulation, transport current is calculated for the next time step after V_i has been calculated and just before t is incremented. I_t^0 is set equal to the operating current.

5.1.2 Magnet Parameter Assumptions

In order to compare maximum temperatures resulting from various inductances, we must make several assumptions concerning the quench initiation and the magnet characteristics that are related to inductance. The following list states important assumptions and compares this simulation to that used in reproducing the experimental voltage traces described in Chapter 3. Significant changes are justified.

- The conductor parameters and wind technique do not change. The number of insulation layers between turns and the contact resistances remain the same and are equal to those used in simulating the test magnet.
- The heated region is assumed to be instantaneously brought to the critical temperature(driven normal). The simulation begins with the heated region at the critical temperature, while all other nodes are at the operating temperature.
- The heated region is the length of one full turn. A smaller normal region will result in a higher maximum temperature because the magnetic energy is dissipated in a smaller volume. However, unlike LTS magnets where epoxy cracking can cause enough dissipation to initiate a quench, localized sources of heat have not been encountered with HTS magnets because of their large minimum quench power density, calculated in Section 3.2.1.
- The heated region is in the outermost layer. This will result in a higher final temperature than an internal quench because heat is conducted away from the normal region through only one radially normal surface.
- For simplicity the self-field is assumed to have negligible effect on critical current and matrix resistivity, as is the case with the test magnet.
- The outer diameter of the wind varies with inductance according to a relationship derived below.

For a solenoidal magnet, its inductance, L, is approximated by the following relationship:

$$L = a_1 \Theta(\alpha, \beta) N^2 \tag{5.6}$$

where a_1 is the inner wind radius, and N is the total number of turns. Θ is a function dependent on geometric parameters, α and β given by:

$$\alpha = \frac{2a_2}{2a_1} \tag{5.7}$$

$$\beta = \frac{2b}{2a_1} \tag{5.8}$$

where a_2 is the wind outer radius and $2b$ is the wind height. It is reasonable to model geometrically similar magnets where the geometric parameters, α and β, remain constant while the size and inductance vary. This makes solving for the wind diameter simpler because Θ will also remain constant.

N is the quotient of half the area intersected by an axial-section through the wind, A_{wnd}, and the overall cross-sectional area of a single turn(includes insulation and void space), A_{trn}. A_{wnd} is given by:

$$A_{wnd} = (a_2 - a_1)2b \tag{5.9}$$

and for N:

$$N = \frac{A_{wnd}}{A_{trn}} = \frac{(a_2 - a_1)2b}{A_{trn}}. \tag{5.10}$$

Substituting Equation 5.10 into Equation 5.6:

$$L = a_1\Theta(\alpha,\beta)\left[\frac{(a_2 - a_1)2b}{A_{trn}}\right]^2 \tag{5.11}$$

Using Equations 5.7 and 5.8 we can solve L in terms of Θ, A_{trn}, a_1, and the dimensionless geometric parameters, α and β:

$$L = a_1^5 \times \frac{\Theta(\alpha,\beta)(\alpha - 1)^2 4\beta^2}{A_{trn}^2} \tag{5.12}$$

The outer radius, a_2, is required in terms of inductance, L, because the quench is initiated in the outermost turn. We obtain a solution for a_2 by substituting a_2/α for a_1 and rearranging:

$$a_2 = L^{1/5} \times \frac{\alpha A_{trn}^{2/5}}{4^{1/5}\Theta(\alpha,\beta)^{1/5}(\alpha - 1)^{2/5}\beta^{2/5}} \tag{5.13}$$

Geometric parameters equal to those of the outer coil of the test magnet are used in this simulation: $\alpha = 1.055$, $\beta = 0.718$, $\Theta(\alpha,\beta) = 1.676\times 10^{-8}$ H/cm, and $A_{trn} = 0.0110$ cm^2. Substituting these values into Equation 5.13 yields a simple relation for a_2 [given in cm] in terms of L [in henry]:

$$a_2 = 17.22 \times L^{1/5} \tag{5.14}$$

This value for a_2 is used to determine the length of a single turn, $2\pi a_2$, which is used for the length of the heated region and effects layer-to-layer conduction, as described in Section 3.3.3. The same contact resistance used in simulating the test magnet, 320 cm^{2}K/W, is applied radially between nodes.

5.2 Simulation Analysis

We are interested in the maximum temperature, T_{max}, reached in the wind over the entire quench event for determining if the coil will be damaged by a quench caused under the specified conditions. The highest temperature at any given time corresponds to the middle of the heated region, where the most dissipation and least conductive cooling occurs throughout the quench event.

Figure 5-2 shows the simulated response of total resistive voltage, temperature at the middle of the heated region, and current decay in a 100-mH magnet(approximately the inductance of the test magnet) operating at 100 A and 20 K. The simulation begins with the heated region at the critical temperature, T_c, and the rest of the coil at the operating temperature, T_o. Current flow through the matrix of the heated region results in an initial resistive voltage. The current immediately begins to drop at a rate proportional to the voltage. After the voltage reaches a maximum, both current and voltage asymptotically approach zero along with Joule dissipation, which is given by their product. When Joule dissipation in the heated region becomes smaller than conductive cooling by the surrounding cool region, the highest temperature in the coil begins to decrease.

5.2.1 Simulation Results

Maximum temperature, T_{max}, versus coil inductance, L is plotted in Figure 5-3 for operating currents between 15 A and 120 A, and operating temperatures of 20 K(solid lines) and 60 K(dashed lines). For a combination of 15 A and 20 K, no temperature rise is observed

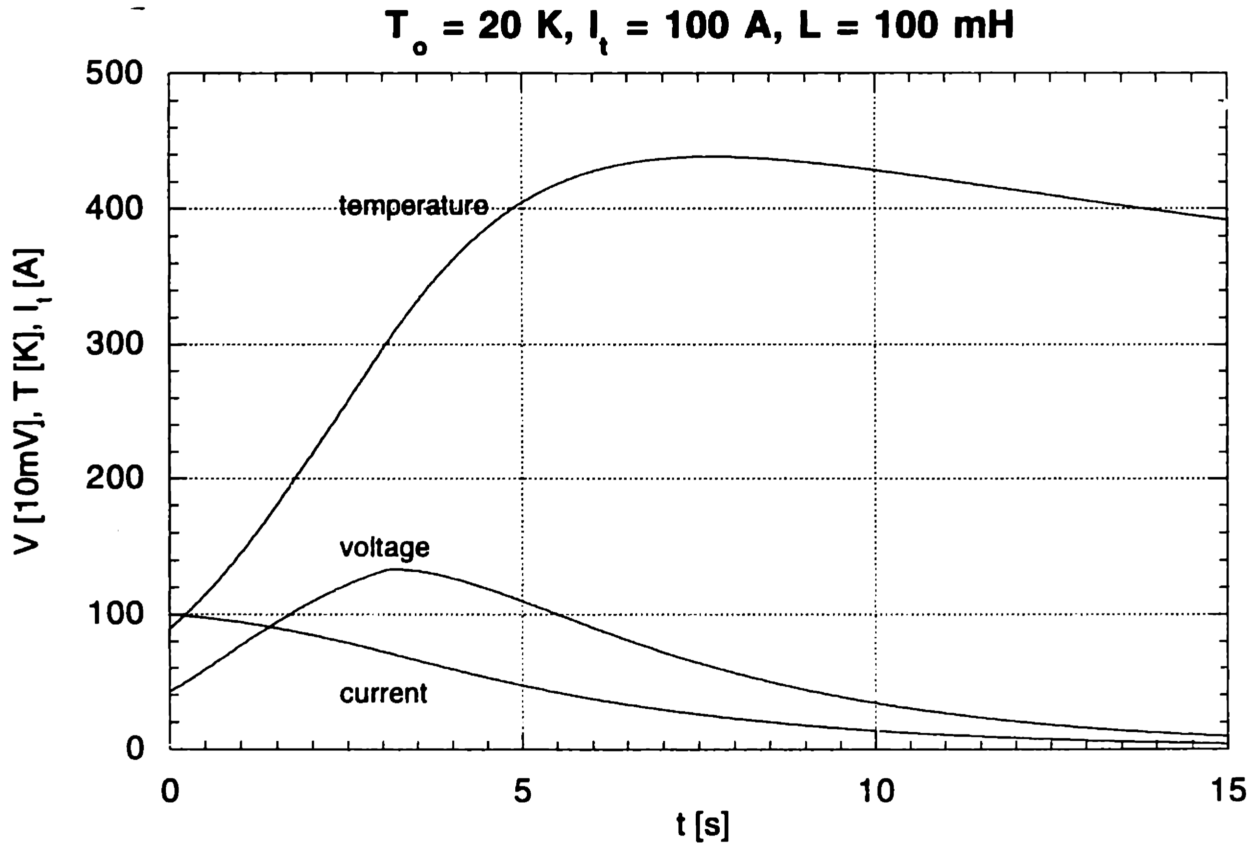

Figure 5-2: Simulated voltage, temperature at the middle of the heated region, and transport current response for a 100-mH magnet operating at 100 A and 20 K.

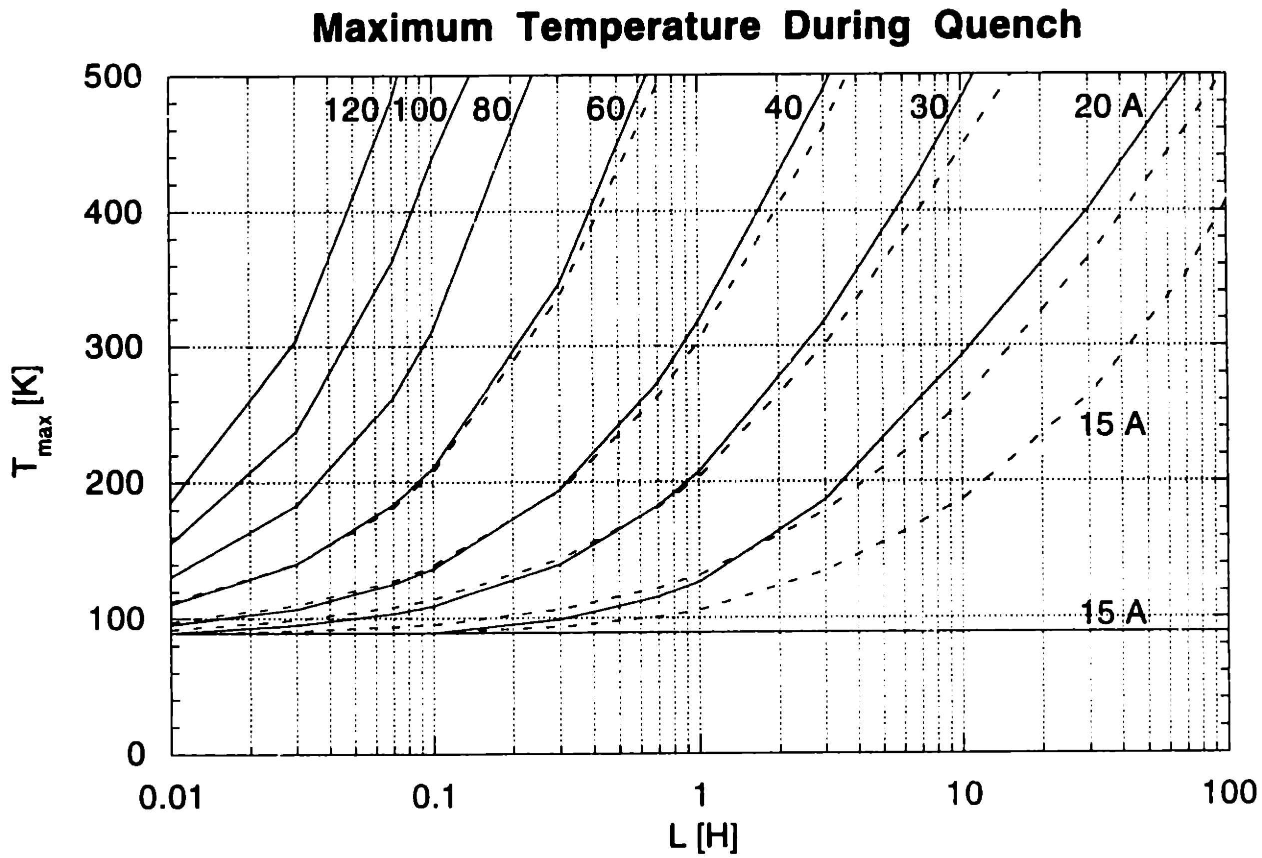

Figure 5-3: Maximum temperature, T_{max}, versus coil inductance, L, for various operating currents and temperatures. Solid lines are for an operating temperature of 20 K, and dashed lines are for an operating temperature of 60 K.

because conduction cooling exceeds dissipation at low currents. However, for the same current at 60 K, the heated region temperature does increase, though even slower, because there is less conduction out of the heated region.

T_{max} increases with inductance faster for higher operating currents because the stored magnetic energy, E_L, is proportional to the square of the current: $E_L = 1/2\,LI^2$. We can estimate T_{max} simply by assuming all of the magnetic energy is dissipated in the heated region with only a negligible amount of heat conducted away. Dividing E_L by the volume of the heated region yields a volumetric enthalpy difference, ΔH. If the heated region begins at the critical temperature, T_c, we have:

$$\Delta H = H(T_{max}) - H(T_c) = \frac{E_L}{w\delta l_{trn}} = \frac{LI^2}{2w\delta l_{trn}} \tag{5.15}$$

where $H(T_{max})$ and $H(T_c)$ are the conductor volumetric enthalpies at the maximum and critical temperatures respectively, w is the conductor width, δ is the conductor thickness, and l_{trn} is the length of a single turn, equal to the length of the heated region. To solve for T_{max}, we rearrange Equation 5.15:

$$H(T_{max}) = H(T_c) + \frac{LI^2}{2w\delta l_{trn}} \tag{5.16}$$

T_{max} is interpolated from $H(T_{max})$ using values for the enthalpy of silver that are tabulated against temperature in [17]. The tabulated values are adjusted by a factor of 0.85 to account for the fraction of BSSCO-2223 in the conductor. A similar modification is made to the specific heat of silver as described in Section 3.4.5.

Equation 5.16 gives a reasonable approximation only when T_{max} is reached in a very short time; otherwise, net conduction away from the normal turn during long durations becomes significant compared with E_L. Trial durations are generally shorter for larger currents and smaller inductance. Table 5.1 compares values for T_{max} that are simulated and estimated using Equation 5.16 for various values of inductance and operating currents of 100 A and 20 A.

Table 5.1: Comparison of Maximum Temperatures

$I_t(0)$ [A]	L [H]	Simulation	Equation 5.16
20	0.010	90	93
	0.100	90	111
	1.000	127	212
	10.00	293	773
100	0.010	156	169
	0.030	238	269
	0.070	363	429
	0.100	438	533

5.2.2 Effect of Changing Thermal Resistance

A smaller thermal resistance will also reduce the maximum temperature reached when operating above I_{tr}, not only because heat is removed from the heated region faster as its temperature climbs, but because more adjacent layers may become resistive, causing the magnetic energy to be dissipated over a larger volume. Figure 5-4 compares simulated traces of the temperature at the middle of the heated region for two 100-mH magnets with different R_{ct}, but are otherwise identical. In this case, decreasing the contact resistance by a factor of 10 reduces the temperature rise by almost 50%.

5.2.3 Effect of Changing Operating Temperature and Critical Current

Figure 5-3 reveals that increasing T_o actually reduces the maximum temperature observed during a quench event, more noticeably at higher values of T_{max}. For higher T_o, less heat is required to drive a section of conductor normal. Therefore, conduction out of the heated region drives adjacent conductor normal sooner, causing the magnetic energy to be dissipated over a larger volume, and resulting in a lower T_{max}. However, increasing T_o does decrease the current required to cause a temperature rise because there is less conduction away from the heated region.

Similar arguments apply to conductor with lower critical current. The lower current

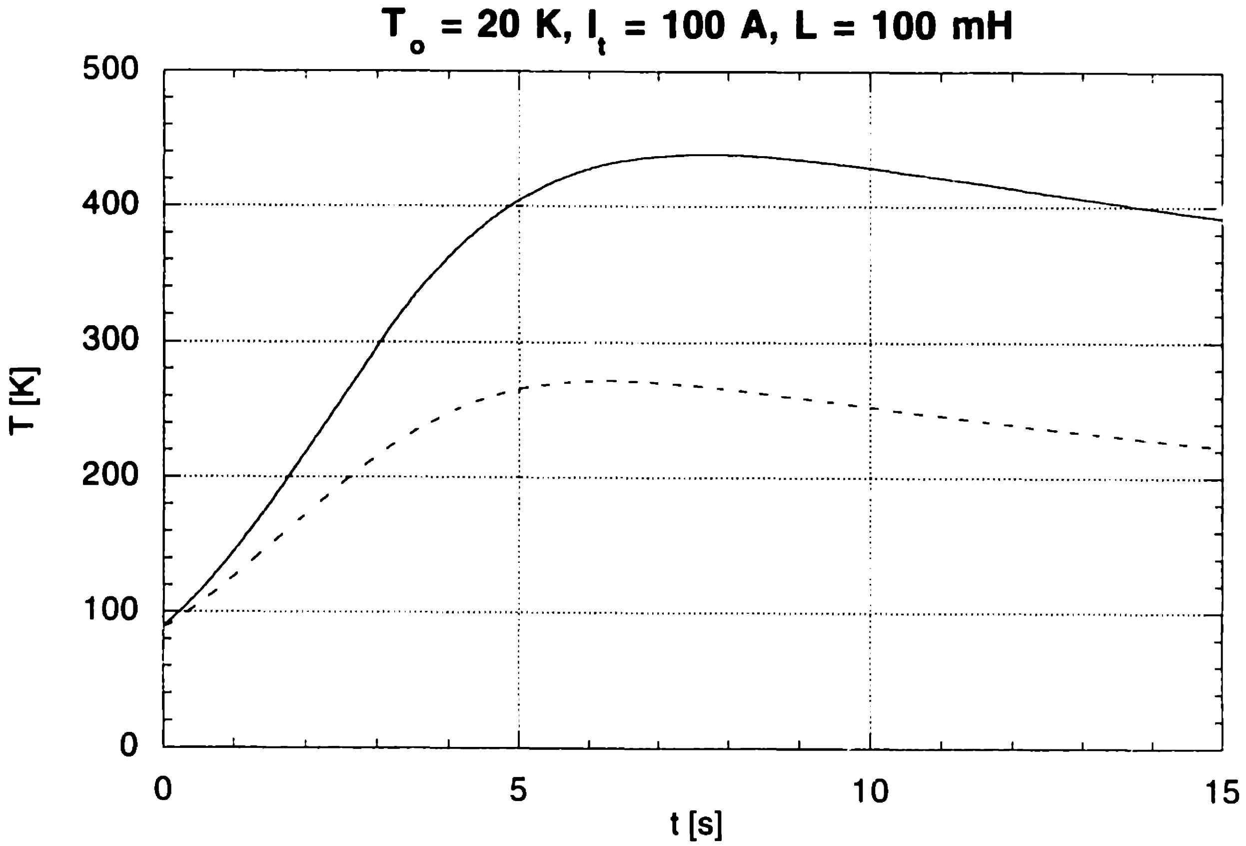

Figure 5-4: Simulated voltage and temperature response for two 100-mH magnets with contact resistances, 320 Kcm^2/W(solid) and 32 Kcm^2/W(dashed).

sharing temperature leads to a smaller enthalpy change required to cause resistive dissipation. But, the difference in maximum temperature associated with varying the critical current tends to be very small.

5.2.4 Effect of Changing Heated Region Parameters

Decreasing the initial temperature of the heated region should not produce any surprisingly different results as long as the temperature is high enough for Joule dissipation to drive the conductor normal. Some of the magnetic energy will be used in bringing the conductor to the normal state, resulting in a situation similar to the conditions simulated for creating Figure 5-3, but with the stored magnetic energy effectively lower.

Changing the heated length can cause severe difference in maximum temperature. When the heated region is larger, the same stored magnetic energy is dissipated in a larger volume, leading to a lower maximum temperature. Figure 5-5 shows simulated voltage and temperature response for identical 100-mH magnets and operating conditions, but different heated lengths. For this particular situation, doubling the heated length reduces the temperature rise by 45%. Therefore, in order to apply this model, we must have a good estimate of the size of the heated region that would likely cause a quench.

5.2.5 Minimum Transport Current to Cause Temperature Rise

Below a particular transport current, I_{tr}, Joule dissipation may be balanced by conduction immediately after the quench is initiated. T_{max} is then independent of both magnet inductance, as is seen in Figure 5-3 for an operating current of 15 A, as well as the length of the heated region. We may estimate the minimum current required for Joule dissipation to cause temperature to increase, by comparing heat conduction out of a small section in the middle of the heated region to Joule dissipation within that section. Simulation reveals that layer-to-layer conduction is more significant than longitudinal conduction at the middle of the heated region. If we assume the second layer temperature is T_o, we can solve for the minimum current by equating Joule dissipation to radial conduction. Below this current, the temperature in the heated region will decrease immediately after it is driven normal.

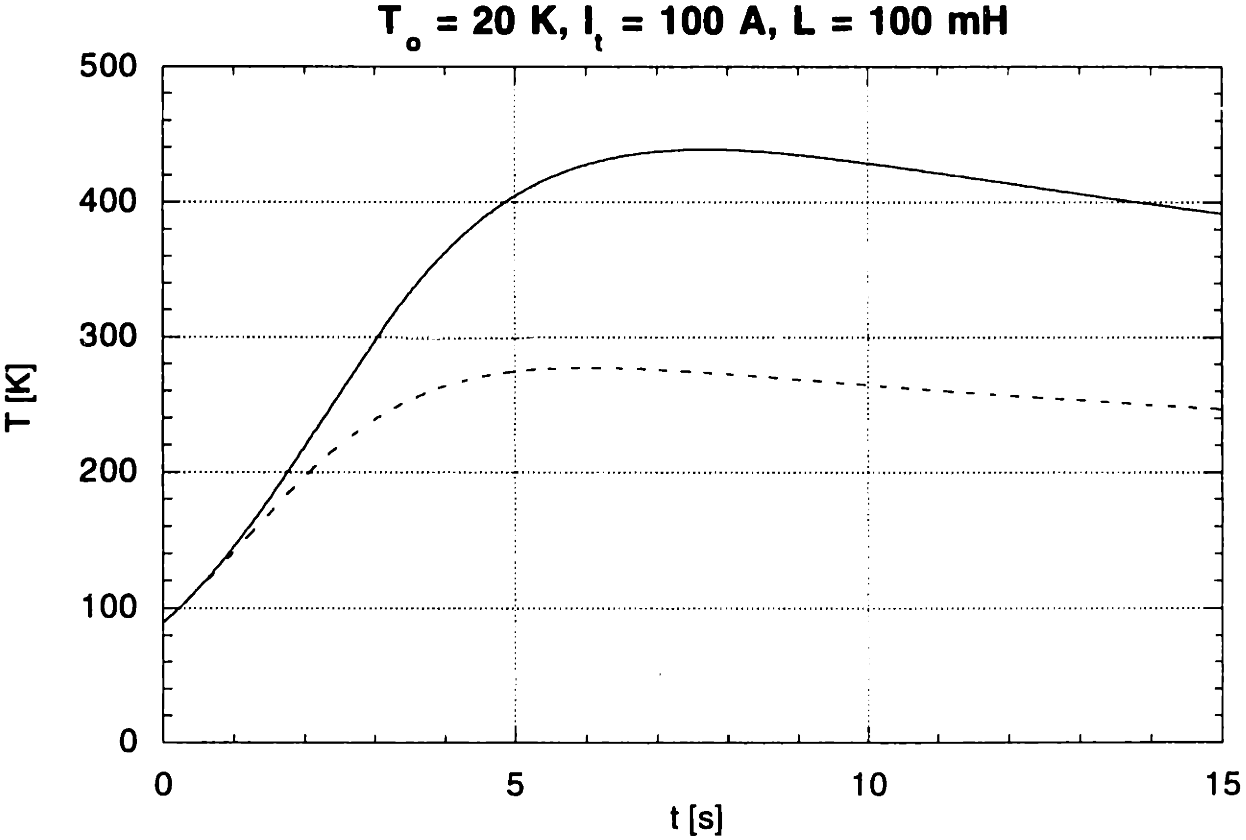

Figure 5-5: Simulated voltage and temperature response for two 100-mH magnets with different heated lengths, 43.0 cm(solid) and 86.0 cm(dashed).

For conductor at the critical temperature, Joule dissipation per unit length, $g(T)$, is given by Equation 3.6:

$$g(T) = I_t^2 \frac{\rho_m}{x_m A_{cd}} \tag{5.17}$$

Conduction in the radial direction per unit length conductor, q_r, is given by:

$$q_r = \frac{W}{\sum R_{th}}(T_2 - T_{hr}) \tag{5.18}$$

where T_2 and T_{hr} are the temperatures of the second layer and heated region, respectively, and $\sum R_{th}$ are the thermal resistances given by:

$$\sum R_{th} = 4R_{ct} + 3\frac{\delta_{ins}}{k_{ins}} \tag{5.19}$$

R_{ct} is the contact resistance, δ_{ins} is the insulation thickness, and k_{ins} is the thermal conductivity of the insulation. The factors of 4 and 3 appear because there are 4 interfaces and 3 layers of insulation between each conductor layer.

Equating Equation 5.17 with Equation 5.18 and substituting in Equation 5.19 gives us a solution for I_{tr}:

$$I_{tr} = \sqrt{\frac{x_m A_{cd} W}{\rho_m} \frac{(T_c - T_o)}{4R_{ct} + 3\delta_{ins}/k_{ins}}} \tag{5.20}$$

where we have set T_{hr} equal to T_c and T_2 equal to T_o. The thermal conductivity of organic materials does not vary much with temperature, so for k_{ins} we use an average value of $\tilde{k}_{ins}$ = 2.0 mW/cmK. Assigning appropriate values to the right hand side variables yields an estimate for I_{tr} = 16 A. According to Equation 5.20, I_{tr} can be increased by reducing the thermal resistance between layers. Decreasing the thermal resistance allows heat to flow from the heated region faster, permitting a larger Joule dissipation to be balanced.

5.3 Addition of Shunt

Two or more shunts placed across approximately equal portions of the magnet will further reduce T_{max} in the conductor during a quench event. Voltage rise across the heated region

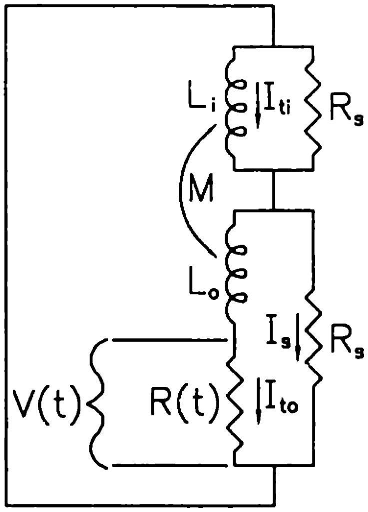

Figure 5-6: Circuit schematic modeling a quench event in a two-coil magnet with each coil shunted.

diverts some of the current to flow through the shunt it is in parallel with, reducing the rate of dissipation and permitting a lower temperature at which conduction will match dissipation. Also, slower dissipation allows the normal region to spread further and increase the volume the energy is dissipated in. Here, we simulate the thermal response of shunted magnets of various inductance when one turn in the outermost layer is driven normal.

5.3.1 Circuit Equations

Figure 5-6 is a circuit schematic representing a magnet consisting of two concentric coils like the magnet tested, with each coil shunted by resistors of equal value, R_s. $R(t)$ denotes the time-dependent electrical resistance across the heated region and may be derived from the voltage rise calulcated by the simulation, $V(t)$, by dividing by the current in the outer coil, I_{to}(t). L_i and L_o are the self-inductances of the inner and outer coils, respectively, and M is their mutual inductance. Using Kirchoff's laws, the time differentials of the transport current in the outer coil, $dI_{to}(t)/dt$, and the current through the shunt resistors, $dI_s(t)/dt$, may be solved in terms of $V(t)$, L_i, L_o, M, R_s, and $I_s(t)$. The current through the shunt resistors are equal and opposite because the voltages across each coil-shunt pair must sum to zero. Using a sign convention with positive current in the direction of the arrows shown in Figure 5-6 results in the following equations for $dI_{to}(t)/dt$ and $dI_s(t)/dt$:

$$\frac{dI_{to}(t)}{dt} = \frac{1}{L_iL_o - M^2}[(L_i + M)R_sI_s(t) - L_iV(t)] \tag{5.21}$$

$$\frac{dI_s(t)}{dt} = -\frac{1}{2(L_iL_o - M^2)}[(L_i + 2M + L_o)R_sI_s(t) - (L_i + M)V(t)] \tag{5.22}$$

Equations 5.21 and 5.22 are easily converted into a numerically usable form by substituting in the appropriate Taylor expansions:

$$I_{to}^{i+1} = I_{to}^i + \frac{\Delta t}{L_iL_o - M^2}[(L_i + M)R_sI_s^i - L_iV^i] \tag{5.23}$$

$$I_s^{i+1} = I_s^i - \frac{\Delta t}{2(L_iL_o - M^2)}[(L_i + 2M + L_o)R_sI_s^i - (L_i + M)V^i] \tag{5.24}$$

where the superscript i denotes which time step. In the simulation, I_{to} is calculated for the next time step after V^i has been calculated and just before t is incremented. The coil and shunt currents have the initial conditions $I_{to}^0 = I_t$, and $I_s^0 = 0$.

The current through the inside coil, $I_{ti}(t)$, is determined by equating with the other three currents leaving the node that corresponds to the magnet's intermediate current port:

$$I_{ti}(t) = I_{to}(t) + I_s(t) + I_s(t) = I_{to}(t) + 2I_s(t) \tag{5.25}$$

or in numerical form:

$$I_{ti}^i = I_{to}^i + 2I_s^i \tag{5.26}$$

5.3.2 Magnet Parameter Assumptions

The simulation determines T_{max} based on the total magnet inductance, L_{i+o}. The other necessary parameters- L_i, L_o, M, and the outer diameter $2a_3$, may be derived from L_{i+o} as follows. The simulated magnet is assumed geometrically similar to itself, having geometric parameters close to that of the test magnet. Scaling the magnet varies its inductances. The coils of the simulated magnet are indistinguishable, except by the position of intermediate current port. In other words, the two coils combined are equivalent to one larger coil. The

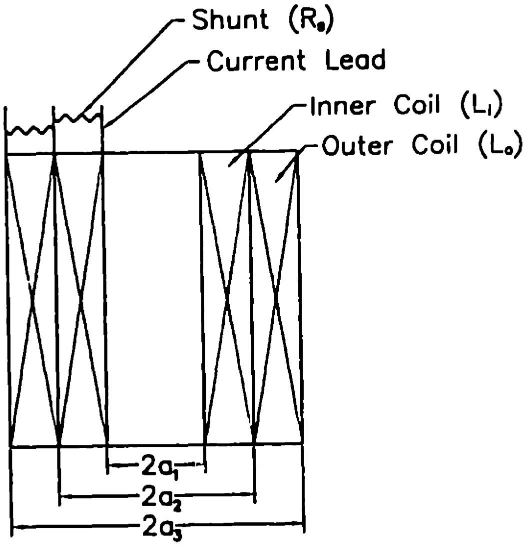

Figure 5-7: Coil configuration used for simulating a quench event in a two-coil magnet with each coil shunted.

arrangement is depicted in Figure 5-7, where $2a_3$ is the outer diameter of the outer coil, $2a_2$ is the inner diameter of the outer coil and the outer diameter of the inner coil, $2a_1$ is the inner diameter of the inner coil, and $2b$ is the height, identical for both coils. The dimensionless geometric parameters, α and β, of both coils and the coil resulting from combining the individual coils do not vary with inductance since we are assuming geometric similarity. Viewing the system as a single coil, the outer diameter is given by modifying Equation 5.13:

$$a_3 = L_{i+o}^{1/5} \times \frac{\alpha_{i+o} A_{trn}^{2/5}}{4^{1/5}\Theta(\alpha_{i+o}, \beta_{i+o})^{1/5}(\alpha_{i+o} - 1)^{2/5}\beta_{i+o}^{2/5}} \tag{5.27}$$

where the subscript, $i + o$, denotes the entire magnet(both coils combined). The self-inductance of the inner and outer coils are given by Equation 5.12:

$$L_o = \left(\frac{a_3}{\alpha_o}\right)^5 \times \frac{\Theta(\alpha_o, \beta_o)(\alpha_o - 1)^2 4\beta_o^2}{A_{trn}^2} \tag{5.28}$$

$$L_i = \left(\frac{a_3}{\alpha_o \alpha_i}\right)^5 \times \frac{\Theta(\alpha_i, \beta_i)(\alpha_i - 1)^2 4\beta_i^2}{A_{trn}^2} \tag{5.29}$$

where the subscripts, i and o, denote the inner and outer coils respectively. Table 5.2 lists the parameters used to obtain the following solutions for a_3 [in cm], L_o, and L_i in terms of

Table 5.2: Geometric Parameters of the Simulated Coil.

Coil	α	β	Θ [H/cm]	A_{trn} [cm^2]
inner	1.046	0.760	1.648×10^{-8}	0.0110
outer	1.055	0.727	1.698×10^{-8}	0.0110
combined	1.104	0.760	1.676×10^{-8}	0.0110

L_{i+o} [in henry]:

$$a_3 = 13.65 \times L_{i+o}^{1/5} \tag{5.30}$$

$$L_o = 0.3254 \times L_{i+o} \tag{5.31}$$

$$L_i = 0.1924 \times L_{i+o} \tag{5.32}$$

The mutual-inductance of the coils is derived from the total magnet self-inductance and the self-inductances of the component coils:

$$M = \frac{1}{2}\Big(L_{i+o} - L_o - L_i\Big) \tag{5.33}$$

5.3.3 Simulation Results

Figure 5-8 shows simulated maximum temperature traces for a 300-mH magnet operating at 20 K and 80 A. Each trace is for a different shunt resistance, R_s: 1.0 mΩ (solid), 10 mΩ (dashed), and infinity(dash-dot). An infinite shunt resistance is equivalent to the case where no shunts are used. It is clear that shunted subdivision lowers the maximum temperature. Voltage and temperature response differs from the shuntless case with respect to an initial sharp change in voltage and current as the outer coil current is diverted into its shunt because of the sudden voltage rise across the heated turn. Thereafter, the response is much like a shuntless magnet. The voltage and currents gradually decay as the temperature reaches a maximum. It is important to note that $I_{ti}(t)$ first jumps above its initial value, equal to the operating current. If $I_{ti}(t)$ exceeds the conductor critical current at any point, the entire

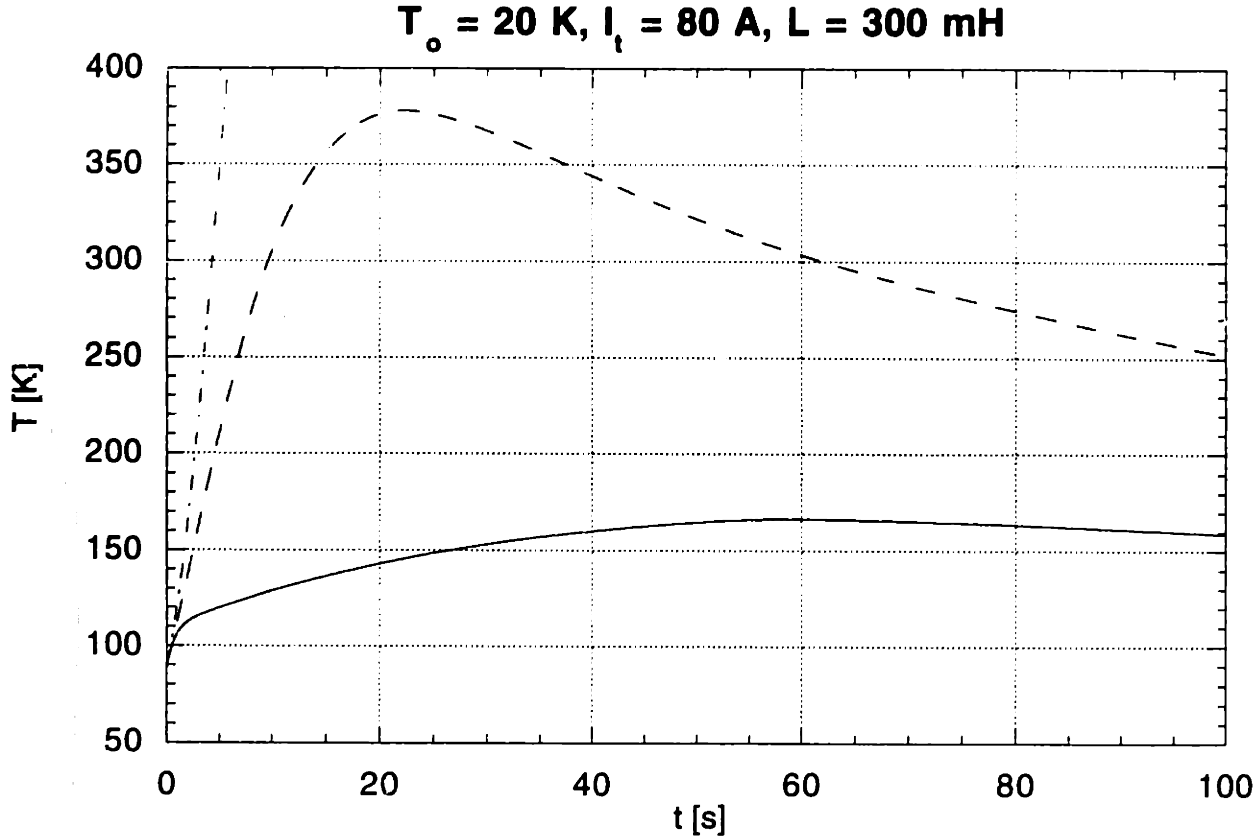

Figure 5-8: Simulated temperature traces for a 300-mH magnet operating at 20 K and 80 A. Each trace is for a different shunt resistance, R_s: 1.0 mΩ (solid), 10 mΩ (dashed), and infinity(dash-dot). An infinite shunt resistance is equivalent to the case where no shunts are used.

inner coil will quench. Such a response may be advantageous as the magnetic energy is dissipated over a relatively enormous volume, substantially reducing T_{max}.

Figure 5-9 shows T_{max} for an operating temperature of 20 K, total inductances larger than 10 mH, operating currents of 20 A and 100 A, and shunt resistances of 1 mΩ (solid), 10 mΩ (dashed), and infinity (dash-dot). Decreasing the shunt resistance always reduces T_{max}, more noticeably for higher inductance.

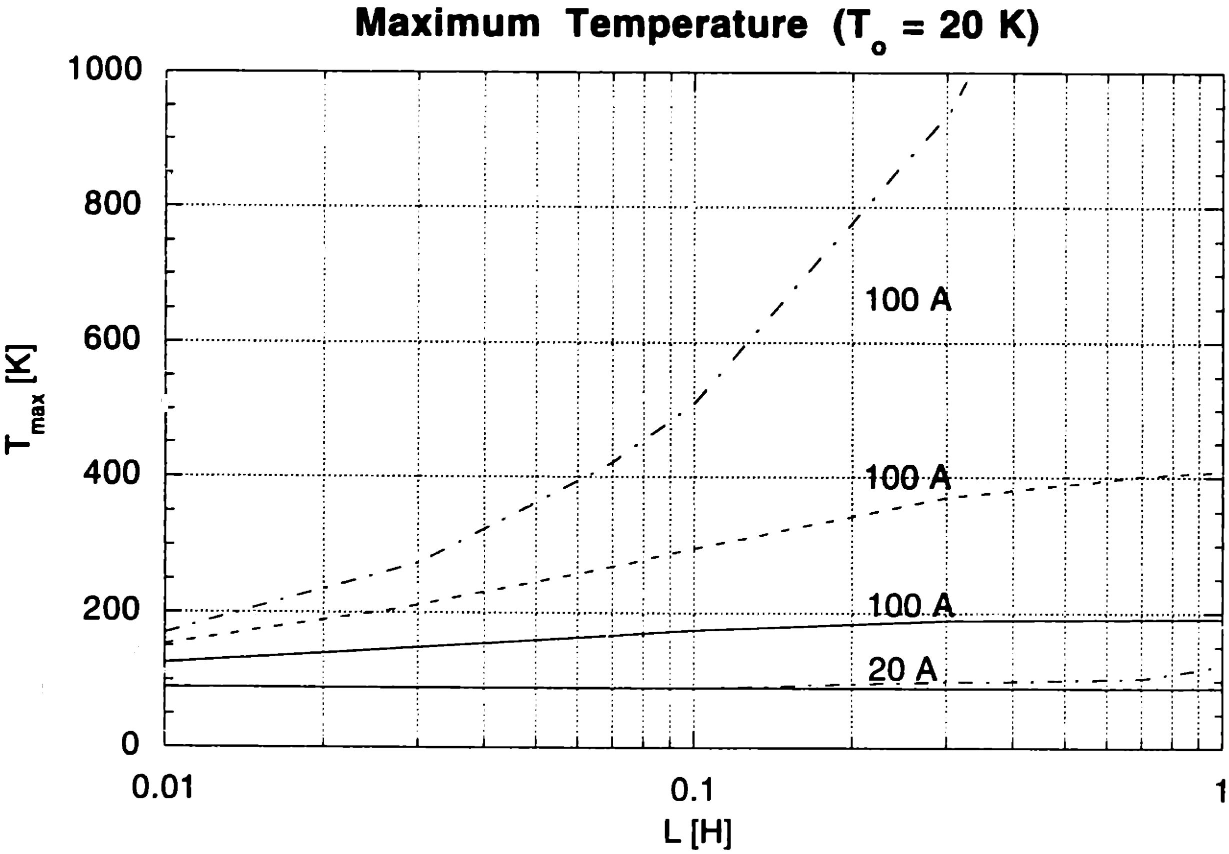

Figure 5-9: Maximum temperature, T_{max}, versus coil inductance, L, for operating currents of 20 A and 100 A with shunt resistance of 1 mΩ(solid), 10 mΩ(dashed), and infinity(dash-dot). An infinite shunt resistance is equivalent to the case where no shunts are used.

Chapter 6

Conclusions

Heater-induced normal zone propagation in a three-dimensional, dry, quasi-adiabatic, high temperature superconducting coil was studied, experimentally and through numerical simulation. Results from the simulation were compared against voltage traces obtained experimentally with a magnet wound with silver-sheathed BSCCO-2223 tape. Although the numerical results show similar change in response for different operating parameters, a better knowledge of the critical current temperature dependency and the contact resistances would produce a much improved simulation. Nonetheless, we have demonstrated that our model closely predicts whether a quench will propagate or recover for various operating conditions. Additionally, we have verified the usefulness of this model by demonstrating that below a certain operating current, a quench in a magnet similar in winding characteristics to the one studied here will cause the current to fully decay before the conductor is thermally damaged.

Bibliography

[1] H. Mukai T. Hikata M. Ueyama T. Kato K. Sato, N. Shibuta and J. Fujikami. Bismuth superconducting wires and their applications. *Cryogenics*, 33, 1993.

[2] Y. K. Kang. Ac-loss induced quenching in adiabatic coils wound with composite superconductors having different twist pitches, 1996.

[3] H. Lim. *Normal Zone Propagation in High-Temperature Superconducting Tape-Wound Coils.* Phd thesis, MIT, Department of Mechanical Engineering, 1996.

[4] C. H. Joshi and Y. Iwasa. Prediction of current decay and terminal voltages in adiabatic superconducting magnets. *Cryogenics*, 29, 1989.

[5] W. H. Cherry and J. I. Gittleman. Thermal and electrodynamic aspects of the superconductive transition process. *Solid State Electronics*, 1, 1960.

[6] Y. Iwasa. *Case Studies in Superconducting Magnets.* Plenum Press, New York, 1994.

[7] Z. J. J. Stekly. Behavior of superconducting coil subjected to steady local heating within the windings. *J. Appl. Phy.*, 37, 1996.

[8] V. Kadambi and B. Dorri. Current decay and temperatures during superconducting magnet coil quench. *Cryogenics*, 26, 1986.

[9] A. Mobius D. Eckert, A. Gladun and P. Verges. Numerical treatment of the quenching process in superconducting magnet system. *Cryogenics*, 21, 1981.

[10] A. Gladun D. Eckert and A. Mobius. A computer program simulating the quench of superconducting magnet system. *IEEE Trans. on Mag.*, 17, 1981.

[11] R. H. Bellis and Y. Iwasa. Quench propagation in high-tc superconductors. *Cryogenics*, 34, 1994.

[12] R.H. Bellis K. Sato Y. Iwasa, E.J. McNiff. Magnetoresistivity of silver over temperature range 4.21̃59 k. *Cryogenics*, 33, 1993.

[13] R. B. Scott. Cryogenic engineering. Technical report, Met-Chem Research Inc., 1988.

[14] L. Dresner. Stability and protection of ag/bssco magnets operated in the 204̃0 k range. *Cryogenics*, 33, 1993.

[15] K. Noto H. Fujishiro K. Michishita M. Matsukawa, F. Tatezaki and Y. Kubo. Thermal conductivity of ag-doped bi-2212 superconducting materials prepared by the floating zone method. *Cryogenics*, 34, 1994.

[16] Y. Touloukian et al. *Thermophysical Properties of Matter.* Volumes 1-12. IFI/Plenum, New York, 1970.

[17] Robert J. Corruccini and John J. Gniewek. Specific Heats and Enthalpies of Technical Solids at Low Temperatures. *NBS Monograph*, 21, 1960.

Appendix A

Simulation Code Listing

```
#include <stdio.h>
#include <stdlib.h>
#include <math.h>

#define DX    0.4          /* longitudinal mesh size */
#define W     .35          /* conductor width */
#define THC   .023         /* conductor azimuthal mesh size */
#define THI   (.0025)      /* insulation azimuthal mesh size */
#define THH   .00127       /* heater azimuthal mesh size */
#define MTOT  300          /* total number of nodes/layer */
#define NTOT  24           /* total number of layers */
#define IT    100.00       /* transport current */
#define TO    23.50        /* operating termperature */
#define DT    0.0003       /* time step */
#define STOP  30000        /* time limit */
#define RMC   0.73         /* volumetric fraction silver */
#define HTP   2520         /* size of heater data */
#define HTL   35           /* nodal heater length */
#define VSTP  1.50         /* voltage simulation terminates */
#define RHT   10           /* thermal resistance beneath heater */
#define RCT   320          /* thermal resistances for other layers */
#define B     0.3          /* magnetic field */
#define TTOT  8000         /* # points for property interpolation */
```

```
#define IC   216.8            /* critical current at 20 K */
#define TC   89.5             /* critical temperature */
#define TRI  3                /* which heater pulse data */

#define ICM  (IC / (20.0 - TC))  /* critical current slope */
#define ICB  ((-ICM) * TC)       /* critical current slope I-intercept */
#define TSKIP (TO + 0.001)       /* temperature rise to add new layer */
#define VMAX  (VSTP/2)           /* half termination voltage */
#define AC   (W * THC)          /* x-section area of conductor */
#define AI   (W * THI)         /* x-section area of insulation */
#define CXF  (2 * W)           /* various constants used in heat */
#define CR   (W * DX)           /*   conduction, dissipation, */
#define CQ   (IT * DX /(RMC * AC)) /*   temperature change, and */
#define CV   (DX / (RMC * AC))    /*   voltage calculations */
#define CT   (DT / (W * DX))
#define LAL  (17.5/DX)          /* nodes per single half-turn */


main()
{
  char mtrl[NTOT], mend[NTOT][MTOT];
  char heat, inside, newl;
  int m, n, time, stop2, outp;
  char mat, mat2;
  int t;

  double T[NTOT][MTOT];
  float ktab[TTOT][3], ctab[TTOT][3];
  float th[NTOT], hpls[(int) (HTP/10)], hpdat[(int) (HTP/10)][6];
  float kx1, kx2, fx1, fx2, q, rho, Ic, c;
  float kr1, kr2[MTOT], fr1, fr2[MTOT], rth[NTOT];
  float thi, thi2, ff;
  float opv1[NTOT], opv2, opvold;

                                      /* functions for calculating props */
```

```
float kcalc(float T, char mtrl);
float rhocalc(float T);
float ccalc(float T, char mtrl);

FILE *ofp, *ifp;

                                        /* initialize output file */
ofp = fopen("vout12e.dat", "w");
fprintf(ofp, "");
fclose(ofp);

                                        /* assign material to layers */
mtrl[0] = 2;
mtrl[2] = mtrl[6] = mtrl[10] = 0;
mtrl[14] = mtrl[18] = 0;
mtrl[22] = 0;
mtrl[1] = mtrl[3] = mtrl[4] = mtrl[5] = mtrl[7] = 1;
mtrl[8] = mtrl[9] = mtrl[11] = 1;
mtrl[12] = mtrl[13] = 1;
mtrl[15] = 1;
mtrl[16] = 1;
mtrl[17] = mtrl[19] = 1;
mtrl[20] = mtrl[21] = mtrl[23] = 1;

                                        /* assign thermal contact resistances */
for(n = 0; n < NTOT; ++n){
 if(n <= 1)
  rth[n] = RHT;
 else if(n < (NTOT - 1))
  rth[n] = RCT;
 else rth[n] = 0;
}

                                        /* read heater pulse voltage data */
ifp = fopen("htpls.dat", "r");
```

```
    for(time = 1; time <= ((int) (HTP/20)); ++time)
      for(n = 0; n < 7; ++n)
        fscanf(ifp, "%f  ", &(hpdat[time][n]));
    fclose(ifp);


                                                /* assign heater dissipation to time steps */
   for(time = 1; time <= ((int) (HTP/20)); ++time)
     hpls[time] = (hpdat[time][(TRI-1)] * hpdat[time][(TRI-1)])/(5.9 * 2 * HTL);

   stop2 = STOP;


                                                /*  initialize temperature and layer end indicator(mend) */
  for(m = 0; m < MTOT; ++m)
    for(n = 0; n < NTOT; ++n){
      T[n][m] = TO;
      mend[n][m] = 0;
      if((n == 0) && (m == (HTL - 1)))
           mend[n][m] = 2;
      if(m == (MTOT - 1))
           mend[n][m] = 1;
  }


                                               /* create interpolation tables for properties */
 for(n = 0; n < 3; ++n){
   for(t = 0; t < 200; ++t)
     ktab[t][n] = ctab[t][n] = 0.0;
   for(t = 200; t < (TTOT); ++t){
     ktab[t][n] = kcalc(((float)t/10), n);
     ctab[t][n] = ccalc(((float)t/10), n);
   }
 }


                                              /* assign thermal conductivity to first layer, */
                                              /* set azimuthal conduction to zero (adiabatic surface) */
for(m = 0; m < MTOT; ++m){
```

```
  kr2[m] = ktab[(int)(10*T[0][m])][mtrl[0]];
  fr2[m] = 0;
}

                                    /* assign thicknesses to layers */
for(n = 0; n < NTOT; ++n){
  switch(mtrl[n]){
  case 0:
    th[n] = THC;
    break;
  case 1:
    th[n] = THI;
    break;
  case 2:
    th[n] = THH;
  }
}

printf("\n\n\n*****");

                                    /* assign thermal conductivity to first layer, */
                                    /* set azimuthal conduction to zero (adiabatic surface) */
for(m = 0; m < MTOT; ++m){
  kr2[m] = ktab[(int)(10*T[0][m])][mtrl[0]];
  fr2[m] = 0;
}

for(time = 1; time < STOP; ++time){          /* time step loop */

                                    /* whent outp > 0, outputs data to file this time step */
  if((time%100) == 0){
    outp = (time/100);
    opv1[2] = opv1[6] = opv1[10] = 0;       /* initialize voltage */
    opv2 = 0;                          /* voltage outer turn/outside heater */
 }
```

```
else outp = 0;

for(n = 0; n < NTOT; ++n){                        /* azimuthal loop */

 if(n < (NTOT -1)){
      inside = 1;                             /* indicates conduction with next layer */
      mat2 = mtrl[n+1];                         /* next layer material quick lookup*/
      thi2 = th[n+1];                          /* next layer thickness quick lookup */
 }
 else inside = 0;                            /* indicates reached inside adiabatic surface */
 thi = th[n];                               /* this layer material quick lookup */
 mat = mtrl[n];                              /* this layer thickness quick lookup */

 if((time < HTP) && (!n))                       /* heater dissipation apply to */
      heat = 1;                             /* this layer at this time? */
 else heat = 0;

 kx2 = ktab[(int)(10*T[n][0])][mat];            /* themal conductivity of */
                                           /* first node in this layer */
 fx2 = 0;                                   /* no longitudinal conduction into first node(symmetry) */

 if((n > 1) && (((n - 1) % 4) == 0))
      newl = 1;                             /* indicates new Conductor layer */
 else newl = 0;

 for(m = 0; m < MTOT; ++m){                       /* longitudinal loop */

      kx1 = kx2;                             /* thermal conductivity of this node and conduction*/
      fx1 = -fx2;                            /* from last node both calculated at last node */
      kr1 = kr2[m];

      if(newl){                             /* if new conductor layer, adjust */
       if(m < LAL)                           /* layer-layer conduction from last layer */
        fr1 = -fr2[m] * (1.0 - (((float) m) / LAL));
       else fr1 = 0;
```

```
}
else fr1 = -fr2[m];

if(mend[n][m])  /* if end of layer or heater, no long. conduction */
  fx2 = kx2 = 0;
else {                              /* otherwise calculate conduction into next */
  kx2 = kr2[m+1];                     /* longitudinal node */
  fx2 = (T[n][m+1] - T[n][m]) * (CXF * thi) / ((DX / kx1) + (DX / kx2));
}

if(inside){                         /* if not last layer, calculate layer-to-next layer */
  kr2[m] = ktab[(int)(10*T[n+1][m])][mat2];  /* conduction */
  fr2[m] = (T[n+1][m] - T[n][m]) * CR/(rth[n] + (thi/(2*kr1)) + (thi2/(2*kr2[m])));
}
else{                               /* if last layer, assign thermal conductivity to */
  fr2[m] = 0;                        /* heater nodes */
  if(m < HTL)
    kr2[m] = ktab[(int)(10*T[0][m])][2];
  else kr2[m] = ktab[(int)(10*T[1][m])][1];
}

c = ctab[(int)(10*T[n][m])][mat];          /* specific heat of this node */

if(!mat){                           /* if conductor node */
  rho = rhocalc(T[n][m]);              /* resistivity of silver for this node */

  if(T[n][m] < TC)                    /* Ic of this node */
    Ic = (ICM * T[n][m]) + ICB;
  else Ic = 0;                       /* zero if above critical temperature */

  if(IT > Ic){
    q = CQ * (IT - Ic) * rho;            /* q of this node */
    if(outp){
      if((n == 2) && (m > HTL))            /* if outside heater in outermost lyr*/
          opv2 += (IT - Ic) * rho * CV;
```

```
            else opv1[n] += (IT - Ic) * rho * CV;   /* voltage contribution from this node */

          }
        }
        else q = 0;
      }
      else q = rho = Ic = 0;

      if(heat)                                    /* dissipation in heater during heating time */
        fx1 = hpls[(int) (time/20)];

                                                  /* new temperature of this node */
      T[n][m] += (CT * (q + fx1 + fx2 + fr1 + fr2[m]))/(c * thi);

      if((T[n][m] > 500.0)){                      /* stop if temperature exceeds 500 K */
        printf("\n %d  %d  %d  %f  %f  %f", time, m, n, T[n][m], q, c);
        m = MTOT;
        n = NTOT;
        time = STOP;
      }

                                                  /* if rest of grid at TO, go to next layer */
      if((((T[2][m - 1]) <= (TSKIP)) && (n) && (m > 2)) || (mend[n][m] == 2))
        m = MTOT;
    }
  }

  if(outp){                                       /* voltage/max temperature output */
    printf("\n%f  %f  %f  %f  %f", time*DT, 2*opv1[2], opv2, T[0][0], T[2][0]);
    ofp = fopen("vout12e.dat", "a");
    fprintf(ofp, "\n%f  %f  %f  %f", (time*DT), 2 * opv1[2], opv2, 2*opv1[5]);
    fclose(ofp);


                                                  /* terminates if maximum voltage exceeded */
```

```
      if((opvl[2] > VMAX) || ((opvl[2] == 0.0) && (opvold > 0.0))){
          printf("\n**********");
          stop2 = time+1;
          time = STOP;
      }
      opvold = opvl[2];

      if(time%1000 == 0){                          /* periodically save temperature profile */
          ofp = fopen("Tout12e.dat", "w");
          for(m = 0; m < MTOT; ++m){
            fprintf(ofp, "\n");
            for(n = 0; n < NTOT; ++n)
              fprintf(ofp, "%f   ", T[n][m]);
          }
      }
      fclose(ofp);
    }
  }

  printf("\n\nMARK\n");

  ofp = fopen("Tout12e.dat", "w");
  for(m = 0; m < MTOT; ++m){
    fprintf(ofp, "\n");
    for(n = 0; n < NTOT; ++n)
      fprintf(ofp, "%f   ", T[n][m]);
  }
  fclose(ofp);
}

float rho0calc(float T)  /* zero field resistivity calculation for silver */
{

  float m0, m1, m2, m3, rho0;
```

```
  if(T<70.0){
    m0 = .069136;
    m1 = -.006714;
    m2 = .00019844;
    m3 = -9.728e-7;
  }

  if(T>=70.0 && T<300.0){
    m0 = -.34145;
    m1 = .0094905;
    m2 = -1.9905e-5;
    m3 = 3.2803e-8;
  }

  if(T<300.0)
    rho0 = (m0 + (m1 * T) + (m2 * T * T) + (m3 * T * T * T)) * 1e-6;
  else rho0 = ((2.6775 * log10(T/300.0)) + 1.6) * 1e-6;

  return rho0;
}


float rhocalc(float T)   /* nonzero field resistivity calculation for silver*/
{

  float m4, m5, rho0, rho;
  float rho0calc(float T);

  rho0 = rho0calc(T);

  if((B * (1.43338e-6)/rho0) < 200.0){
    m4 = .00014736;
    m5 = 1.5838;
  }
  else{
```

```
    m4 = .117;
    m5 = .76403;
  }

  rho = (rho0 * m4 * pow((B * (1.43338e-6)/rho0), m5)) + rho0;
  return rho;
}


float kcalc(float T, char mtrl)  /* thermal conductivity for all materials */
{
  float k, k0, rho, rho0;
  float rhocalc(float T);
  float rho0calc(float T);

  if(mtrl == 0){
    rho = rhocalc(T);
    rho0 = rho0calc(T);

    if(T<300)
      k0 = 4.0 + (3.2 * T * T * pow(2.71828, (4.0 - T)/4.5));
    else k0 = 4.0;

    k = RMC * (1 + (0.05 * B)) * (rho0 / rho) * k0;
  }

  if(mtrl == 1)
    k = (0.0015335 + (.0000227 * T));

  if(mtrl == 2)
    k = (-.001877 + (.001260 * T) + (-3.3219e-6 * T * T) + (2.7041e-9 * T * T * T));

  return k;
}
```

```
float ccalc(float T, char mtrl)  /* heat capacity for all materials */
{
  float c;

  if(mtrl == 0)
    c = ((1.0 + RMC)/2)*pow((pow((17.75e−6 * T * T * T), −0.85) + 0.47081), −1.1765);

  if(mtrl == 1)
    c = (−.016 + (.002074 * T) + (1.7738e−4 * T * T));

  if(mtrl == 2)
    c = (−.014096 + (.005665 * T) + (2.46e−5 * T * T));

  return c;
}
```